UNIVERSITA' DEGLI STUDI DI PARMA

Dottorato di ricerca in Scienze Chimiche

Ciclo XXV (2010-2012)

Energy transfer and charge transfer processes in luminescent materials

COORDINATOR

Prof. Giovanni Predieri

TUTOR

Dr. Enrico Cavalli

PhD CANDIDATE

Angiuli Fabio

2013

INDEX

INTRODUCTION

Luminescent inorganic solid-state materials find application in a broad range of largely used devices like TV and computer panels, fluorescent lamps and LEDs, lasers, detectors and others. The continuous technological evolution implies an ever growing demand of materials with better and better characteristics in terms of performance, reduced production costs, energy saving, new application possibilities, and so on. The challenge is of capital importance: large amounts of energy are in fact consumed for lighting and during operation of displays, then the development of economical light sources like white light-emitting diodes and display panels with enhanced efficiency constitute crucial targets. There are other aspects deserving consideration: for instance, the efficiency of the solar cells could be in principle improved using phosphors which allow the conversion of thermal radiation into electrical energy. Moreover some medical imaging diagnostic methods require efficient and sensitive detectors, and devices based on inorganic phosphors appear as very promising solutions in this connection. Enormous interests are involved, and for this reason the research activities in this field are frenetic and often oriented more in the assessment of the application potentialities of the material than in the investigation of the intrinsic luminescence mechanisms. Many fundamental questions are still open and strongly motivate speculative investigations. The work described in this thesis has been carried out in the belief that the deep knowledge of the properties of a material is a fundamental requisite for its successful development. It is organized as follows. In Section 1 some theoretical concepts are presented, which will be useful in the analysis of the experimental data. General information about the experimental procedures is provided in Section 2, concerning the synthesis of the investigated materials, their morphological, structural and spectroscopic characterization. Section 3 reports a study concerning the effect of the host composition and of the synthesis conditions on the luminescence properties of Dy^{3+}-doped yttrium phospho-vanadate white-emitting phosphors. In Section 4 the spectral properties of $CaMoO_4:Pr^{3+}$ in form of both single crystals and powder have been explored in order to assess the role of the sample morphology and of the charge transfer states in the emission dynamics of this material. The investigations on the effects of the charge transfer states on the luminescence behavior have been extended to the interesting case of Bi^{3+} in $Y(P,V)O_4$ (Section 5), that has been successfully dealt with in the light of a recently proposed model. Starting from these results, the positive effect of bismuth co-doping on the emission properties of YPO_4 activated with several rare earth ions has been carefully characterized in Section 6, and an new point of view has been proposed in order to account for the observed results. At last, Section 7 is dedicated to a research activity concerning the photoswitching of bis-spiropyran using near-infrared light, performed in the ambit of an internship at the Department of Chemistry and Biochemistry of the Concordia University (Montreal, Canada) under the supervision of Prof. John Capobianco.

Chapter 1

Theoretical aspects

1.1 Luminescent materials

A luminescent material, often called phosphor, is a solid which converts certain types of energy into electromagnetic radiation in the visible range as well as in other spectral regions, such as ultraviolet or near-infrared [1]. The classification of a luminescence process depends on the excitation mechanism. For example, the bioluminescence is the emission by a living organism, the chemiluminescence is the result of a chemical reaction, in the cathodoluminescence the material is excited by an electron beam, and so on. In the photoluminescence the emission is the result of absorption of photons of suitable energy.

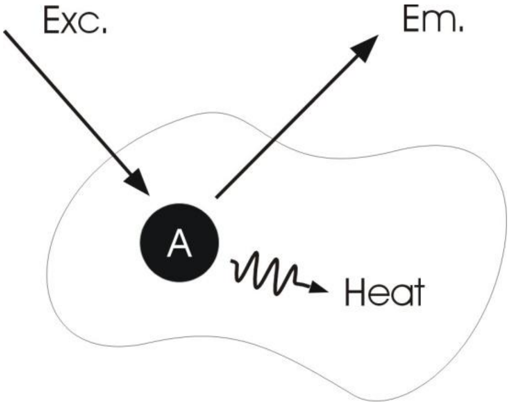

Fig. 1.1. Luminescent material constituted of an activator (*A*) in the host lattice. Exc.: excitation; Em.: emission; Heat: nonradiative return to the ground state.

As schematically drawn in Fig. 1.1, a photoluminescent material consists of a host lattice and a luminescent center called activator (*A*). In the simplest case, the excitation radiation is absorbed by the activator which is raised to an excited state. The return to the ground state can take place radiatively through emission of radiation or nonradiatively through the vibrational states of the host lattice (Fig. 1.2) or other mechanisms. The radiative and the nonradiative process are in competition, then it is necessary to minimize the efficiency of the latter in order to increase the efficiency of the emission channel.

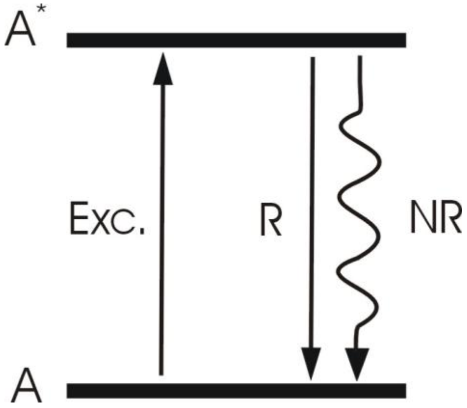

Fig. 1.2. Energy level diagram of the activator *A* in Fig. 1.1, where *A** indicates the excited state, *R* the radiative and NR the nonradiative return to the ground state.

In many cases the absorbing and the emitting center do not coincide. The incident radiation is absorbed by an ion, denoted as sensitizer (*S*), that subsequently transfers the energy to the activator (*A*), as shown in Fig. 1.3. The sensitizer can be present as a co-doping ion or as constituent of the host lattice.

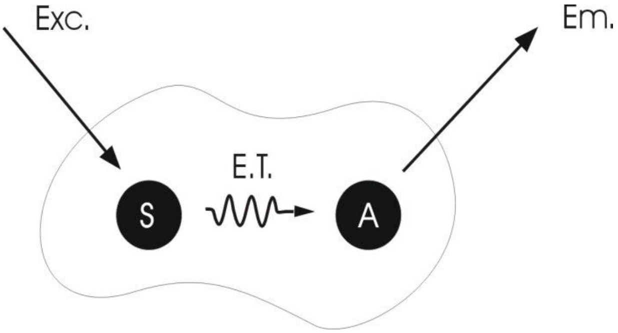

Fig. 1.3. Energy transfer (E.T.) from a sensitizer *S* to an activator *A*.

1.2 Shape and intensity of the optical absorption bands

The shape of an optical absorption band can be explained using the single configurational coordinate diagram [2]. The diagram shows the potential energy curves of the absorbing center as a function of a configurational coordinate which describe one of the vibrational modes of the center involved. We consider exclusively the symmetrical stretching mode in which the ligands are moving in phase with respect to the central metal ion (Fig. 1.4). As shown in Fig. 1.5, the configurational coordinate diagram for this mode consists of a plot of the energy E versus the metal-ligand distance R. The curve for the ground state is parabolic with a minimum at R_0. The parabolic shape follows from the fact that the vibrational motion is assumed to be harmonic. The restoring force F is therefore proportional to the displacement: $F= - k(R-R_0)$ and corresponds to a potential energy whose dependence on R is parabolic: $E= ½ k (R-R_0)$. The minimum of the parabola R_0 corresponds to the equilibrium distance in the ground state.

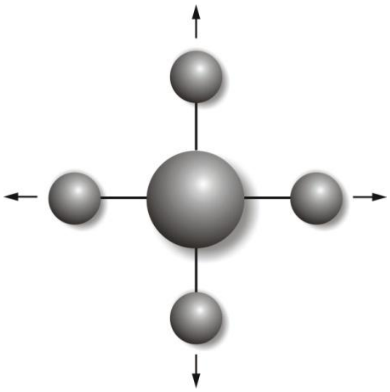

Fig. 1.4. Symmetrical stretching vibration of a square-planner complex.

The quantum mechanical solution of this problem is the harmonic oscillator and yields $E_{\nu}= (\nu+1/2)h\nu$, where $\nu= 0, 1, 2, \ldots$. The energies of these vibrational levels are shown in Fig. 1.5. Also the excited state has a parabolic shape in the configurational coordinate diagram, but with different values of the equilibrium distance (R_0') and of the force constant (k'). These differences arise from the fact that in the ground and in the excited state the chemical bond is different, and the value of $\Delta R= R_0'-R_0$ is a qualitative measure of the difference in the electron-phonon interaction in the two states. An absorption transition implies the excitation of the active center from its ground state to a higher lying state. In the Franck-Condon approximation the electronic transition can be represented by a vertical transition in the configurational coordinate diagram (Fig. 1.6). The most probable absorption transition starts from the lowest vibrational level ($\nu= 0$) in correspondence of R_0, where the vibrational wave function has its maximum value, and terminates in correspondence of the edge of the excited stated parabola, where the vibrational levels have their highest amplitude (Fig. 1.7).

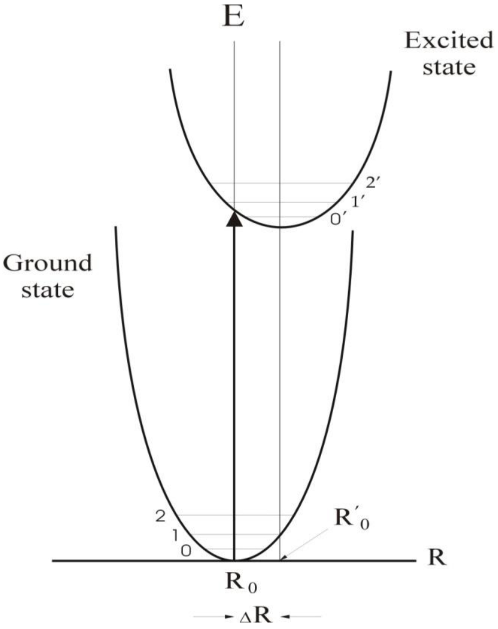

Fig. 1.5. Configurational coordinate diagram illustrating an absorption transition. The ground state has equilibrium distance at R_0 and vibrational levels $\nu = 0, 1, 2$. The excited state has equilibrium distance at R_0' and vibrational levels $\nu' = 0, 1, 2$. The parabola offset is $\Delta R = R_0' - R_0$.

This transition corresponds to the maximum of the absorption band. Less probable transitions, starting at R value larger or smaller than R_0, are also possible. The probability for an optical transition between the $\nu = 0$ vibrational level of the ground state and the $\nu = \nu'$ vibrational level of the excited state is proportional to:

$$< e / r / g > < \chi_\nu / \chi_0 > \qquad (1.1)$$

where e and g are the electronic wave function of the excited state and the ground state respectively, r is the electric dipole operator of the transition and χ are the vibrational wave functions.

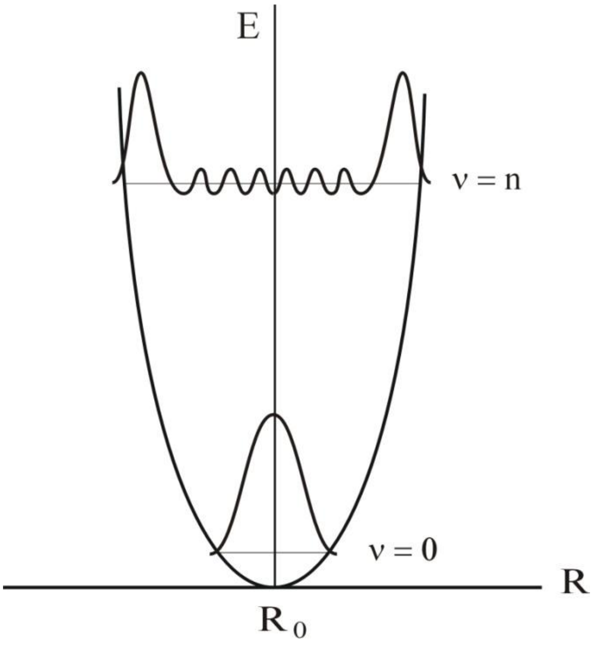

Fig. 1.6. The wave functions for the lowest vibrational level ($\nu = 0$) and a high vibrational level ($\nu = n$).

The first part of the equation is the electronic matrix element, which is independent of the vibration and determines the intensity of the transition. The second part represents the vibrational overlap and determines the shape of the absorption band. When $\Delta R = 0$, the overlap of the vibrational wavefunctions will be maximum for $\nu = \nu' = 0$, since the involved vibrational wave functions have their maxima coincident at R_0. The absorption transition consists of one line, and is referred to as the zero-vibrational or no-phonon transition, since no vibrations are involved.

If $\Delta R \neq 0$, the $\nu = 0$ level will have vibration overlap with several levels with $\nu' > 0$, and a broad absorption band is observed (Fig. 1.7). The broader the absorption band, the larger the value of ΔR.

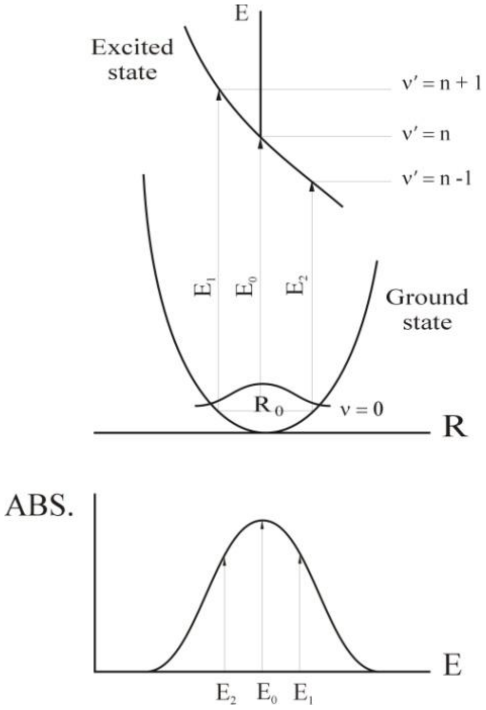

Fig. 1.7. The optical absorption transition between two parabolas which have an offset relative to each other in the configurational coordinate diagram consists of a broad absorption band.

The intensity of the optical absorption transition is determined by the first part of the Eq. 1.1 and it is substantially governed by the selection rules. The spin selection rule states that transitions between levels with different spin states ($\Delta S \neq 0$) are forbidden, whereas the parity selection rule states that transitions between levels with the same parity (*d-d*, *f-f* transitions, etc.) are forbidden. Interactions like the spin-orbit coupling and electron-vibration coupling induce a partial relaxation of the selection rules and make the forbidden transitions in part possible.

1.3 The effect of the host lattice

The optical properties of a luminescent center are significantly influenced by their surroundings. In this connection, the main host lattice-optically active ion interactions influencing the absorption/emission properties are ascribable to:

- Covalency
- Crystal field
- Inhomogeneous broadening

With increasing covalency the interaction between electrons is reduced since they spread out over wider orbitals. Therefore, the electronic transitions between levels whose energy difference is determined by electron interaction shift to lower energy for increasing covalence. This is known as nephelauxetic effect: the electron repulsion in the coordination complex is lower than that of the free ion due to the increased distance between the electrons.

The crystal field is the electric field at the site of the ion under consideration due to the surroundings. The transition metal ions are the best known examples of how the spectral position of certain optical transitions and consequently the color of the compound is determined by the strength and the geometry of the crystal field. In addition it is responsible for the symmetry splitting of the optical transitions. In the case of the rare earth ions the effect of the crystal field on the structure and position of the *f*-*f* transitions is rather weak, as we shall discuss later.

In powders the external surface is large and the ions near the surface are in a bonding situation different than in the bulk. These ions have their optical transitions at slightly different energies from those in the bulk and the features in the spectra broaden (Fig. 1.8). In crystals the inhomogeneous broadening can result from the presence of lattice defects, of non-equivalent lattice sites available for the optical centers, of perturbations arising, for instance, from charge compensation mechanisms, structural disorder, etc..

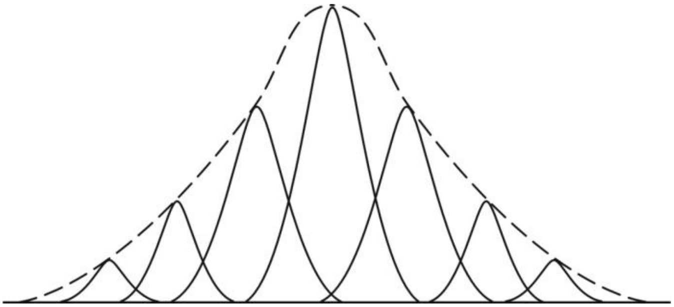

Fig. 1.8. Inhomogeneous broadening. The individual absorption transitions vary slightly from site to site in the host lattice. The broken line indicates the experimentally observed absorption spectrum.

1.4 The absorption transitions: selected cases

In this section we briefly discuss the nature of the absorption bands of some classes of compounds that have been considered in the ambit of this thesis.

Ions with d^0 electronic configuration.

Compounds like YVO_4, $YNbO_4$ and $CaWO_4$ are important host lattices for emitting ions and have intrinsic luminescence properties. They are in general constituted of tetrahedral or octahedral MO_n^{x-} (M= V^{5+}, Nb^{5+}, W^{6+}, etc.; n= 4 or 6) units developing along the crystalline building giving rise to cages (sites) with suitable geometries that can be occupied by the cations. Their absorption spectra show strong and broad bands in the ultraviolet. The transition involved is a charge transfer from oxygen to the d^0 ion [3]. An electron is excited from a non-bonding orbital (on the oxygen ions) to an anti-bonding orbital. Therefore the bonding is strongly weakened after optical absorption, so that $\Delta R >> 0$ and the band width is large. The spectral position of this absorption transition depends on many factors: the $d^1 \rightarrow d^0$ ionization potential, the number and the nature of the ligands, the interaction between ions in the lattice, etc..

Trivalent rare earth ions.

The rare earth ions are characterized by unfilled $4f^n$ ($n=1...13$) electronic shells. The *4f* orbitals are shielded from the surroundings by the filled $5s^2$ and $5p^6$ shells, then the influence of the crystal field on the optical transitions within the $4f^{\,n}$ configuration is relatively small. The electronic levels are classified using the classical $^{2S+1}L_J$ Russell-Saunders notation for the spherical symmetry and their energy position is nearly independent on the host lattice [4]. Fig. 1.9, referred to as the *Dieke diagram*, reports the energy levels originating from the $4f^n$ configuration as a function of n for the trivalent ions in $LaCl_3$. The thickness of the bars indicates the order of magnitude of the crystal field splitting, that is rather small. The Dieke diagram is a very useful tool for the assignment of the absorption and emission bands. The *f-f* transitions are symmetry forbidden and the electron-phonon coupling is small, i. e. $\Delta R=0$. The optical spectra of trivalent rare earth ions will then be composed of a number of weak manifolds constituted of sharp lines. The quantum mechanical approach to the allowance problem is at the basis of a generally accepted and widely applied method for the analysis of the absorption spectra of the rare earth doped materials.

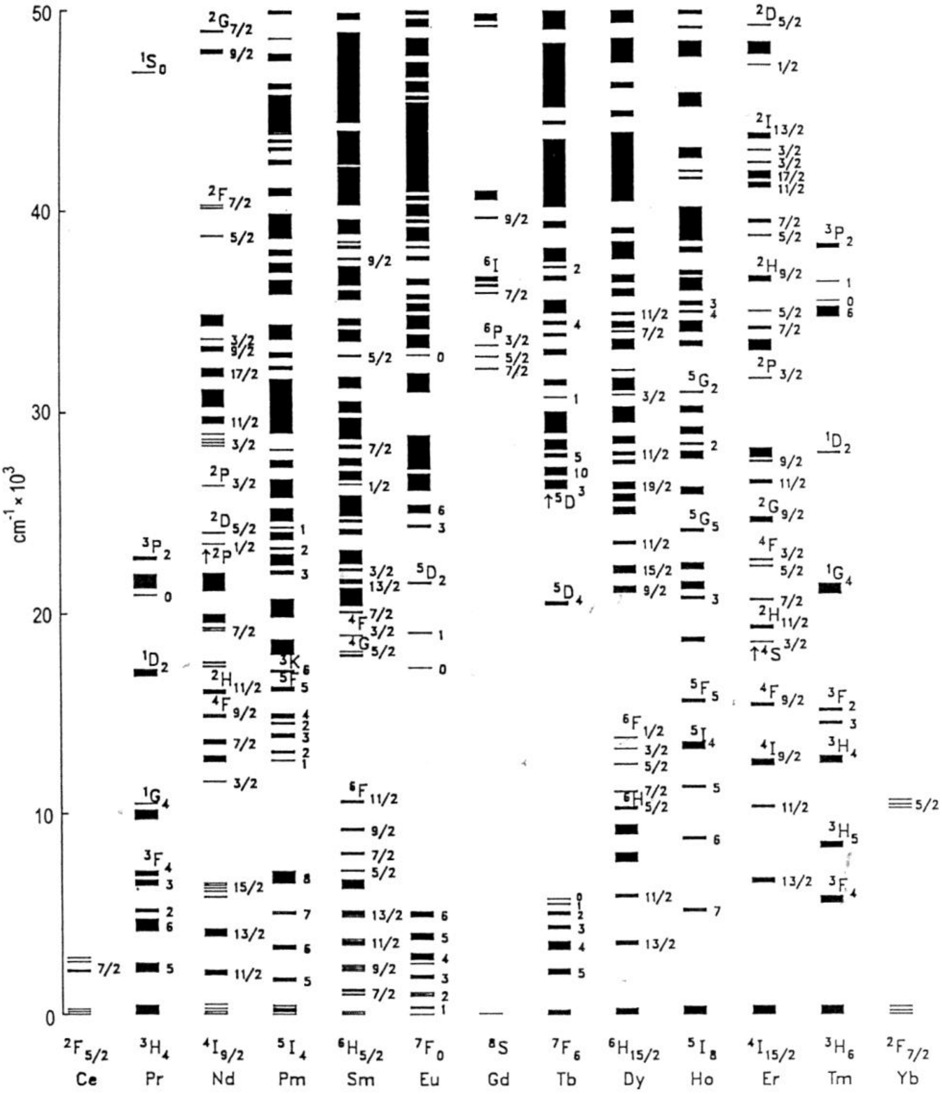

Fig. 1.9. Energy levels of the 4f ^{n} configurations of the trivalent lanthanide ions.

The main aspects of this method are briefly summarized in the following.

It can be demonstrated that the probability of a transition from an *i* to a *j* electronic state is proportional to the square of the matrix element $\langle i|\hat{P}|j\rangle$, where $\hat{P}$ is a suitable electric dipole, magnetic dipole or electric quadrupole operator. The intensity ratios between transitions allowed for the three above mechanisms are $1:10^{-6}:10^{-9}$, respectively. This is the reason why the electric dipole mechanism is considered by far the main origin of the optical spectra. In the case of materials containing trivalent lanthanide ions, the electric dipole mechanism takes place between states belonging to the same $4f^{n}$ configuration and the transitions are symmetry forbidden. They become partially allowed thanks to static or dynamic odd crystal field components inducing some mixing of the $4f^{n}$ wave functions into $4f^{n-1}nl$ (where *nl* usually is *5d*) functions having opposite parity. Consequently, their intensity is low and the contribution of other mechanisms cannot be neglected.

In summary, the optical transitions of the rare earth compounds can be classified as follows (in decreasing order of importance):

- electric dipole transitions induced by odd crystal field components (forced dipole transitions),
- electric dipole transitions induced by odd vibrations (vibronic transitions),
- magnetic dipole transitions,
- electric quadrupole transitions (usually negligible).

Judd and Ofelt [5, 6] demonstrated that the oscillator strengths of the transitions observed in the room temperature absorption spectra, given by:

$$f_{ij}^{ed} = \frac{8\pi^2 m\nu}{he^2}\chi\langle i|\hat{P}_{ed}|\,j\rangle \qquad (1.2)$$

can be expressed by the following equation:

$$f_{ij}^{ed} = \sum_{\lambda=2,4,6}\frac{8\pi^2 m\nu}{he^2}\chi(2J+1)^{-1}\Omega_{\lambda}\left|\left\langle f^{N}J\left\|U_{\lambda}\right\|f^{N}J'\right\rangle\right|^2 \qquad (1.3)$$

where m is the electron mass, ν the frequency of the transition, $\chi = \frac{n(n^2+2)^2}{9}$ the local field correction, n the refractive index of the host material, $\langle f^N J \| U_\lambda \| f^N J' \rangle$ are the reduced matrix elements of the irreducible tensor operator of rank λ, whose values are reported in suitable tables, and Ω_λ (λ= 2, 4, 6) are the intensity or Judd-Ofelt parameters. They are properties of the host material and can be determined by means of the least square fitting of the experimental oscillator strengths:

$$f^{\exp} = \frac{mc}{N\pi e^2} \int \alpha(\nu) d\nu \qquad (1.4)$$

where N is the doping concentration (in ion·cm^{-3}) and $\int \alpha(\nu) d\nu$ is the integrated absorption coefficient.

The intensity parameters give information about the efficiencies of different materials containing the same rare earth activator, and allow the calculation of other interesting parameters like the spontaneous emission coefficients:

$$A_{ij}^{ed} = \frac{8\nu^2 e^2 \pi^2}{c^3 m} \cdot f_{ij}^{ed} = \frac{64\pi^4 e^2 \nu^3}{3hc^3(2J+1)} \chi \sum_{\lambda=2,4,6} \Omega_\lambda \left| \langle f^N J \| U_\lambda \| f^N J' \rangle \right|^2 \qquad (1.5)$$

the radiative lifetime of an emitting state i:

$$\tau_i^R = \frac{1}{\sum_j A_{ij}^{ed}} \qquad (1.6)$$

and the fluorescence branching ratios:

$$\beta_{ij} = \frac{A_{ij}^{ed}}{\sum_{j} A_{ij}^{ed}} \qquad (1.7)$$

These can be compared with the experimental results in order to obtain information about the nonradiative processes.

Some general selection rules for electric dipole transitions have been obtained from the Judd-Ofelt theory:

a. $J \leq 6$, $\Delta S = 0$, $\Delta L \leq 6$ **(**Russell-Saunders approximation).

b. For a rare earth ion with an even number of electrons:

1. $J = 0 \leftrightarrow J' = 0$ is forbidden
2. $J = 0 \leftrightarrow$ *odd* J' values are weak
3. $J = 0 \leftrightarrow J' = 2, 4, 6$ should be strong

In most cases, the intensities of the $f \leftrightarrow f$ transitions of the trivalent lanthanides are relatively independent on the coordination geometry. There are however certain transitions associated to specific host-ion combinations that are very sensitive to changes in local environment. These are called *hypersensitive transitions* [7]. They have large values of the Ω_2 parameter and obey the selection rules:

$\Delta J \leq 2$, $\Delta L \leq 2$ and $\Delta S = 0$

The origin of the hypersensitivity has yet to be clarified. Most probably, it can be related to the covalent character of the metal-ligand bond.

As stated before, the contribution of the transitions allowed for the magnetic dipole mechanism is significant and cannot be neglected in the calculation of the intensity parameters. They obey the selection rules:

- $\Delta J = 0, \pm 1$ with $0 \leftrightarrow 0$ forbidden

- $\Delta S = 0$, $\Delta L = 0$

The oscillator strengths of the most important magnetic dipole transitions have been calculated and are tabulated.

In addition to the *f-f* transitions, the trivalent rare earth ions can give rise to intense absorption broadbands located in the UV region, that can be ascribed to two different types of allowed interconfigurational transitions:

- charge-transfer transitions ($4f^{n} \rightarrow 4f^{n+1} L^{-1}$, where L=ligand)
- $4f^{n} \rightarrow 4f^{n-1} 5d$ transitions

The trivalent ions that have a tendency to become divalent (Sm^{3+}, Eu^{3+}, Yb^{3+}) show charge-transfer absorption bands in the ultraviolet. Those that tend to the tetravalent state (Ce^{3+}, Pr^{3+}, Tb^{3+}) give rise to $4f \rightarrow 5d$ absorption bands in the UV region.

Ions with s^2 *configuration.*

Ions with s^2 configuration (Tl^{+}, Bi^{3+}, Pb^{2+}, etc.) show strong optical absorption in the ultraviolet due to a parity allowed $s^2 \rightarrow sp$ transition. The s^2 configuration of the ground state gives rise to the $^1S_0$ energy level. The *sp* excited configuration yields, in sequence of increasing energy, the $^3P_0$, $^3P_1$, $^3P_2$ and $^1P_1$ levels [8]. The most intense band observed in the absorption spectrum is assigned to the $^1S_0 \rightarrow {}^1P_1$ transition, that is both spin and symmetry allowed. It is a broad transition, since the ground and the excited state belong to different configurations and then $\Delta R \neq 0$. A second, weaker band at lower energy is usually observed. It is ascribed to the spin forbidden $^1S_0 \rightarrow {}^3P_1$ transition, that becomes partially allowed in consequence of the spin-orbit coupling.

Metal-to-ligand and metal-to-metal charge transfer transitions.

The above discussed charge-transfer processes involving a rare earth ion and its surroundings are classified as ligand-to-metal charge transfer (LMCT) transitions. Other charge transfer transitions are possible, like the metal-to-ligand charge transfer (MLCT) for instance, although not very probable in oxide materials. More interesting is the metal-to-metal charge transfer (IVCT or MMCT) transition in which an electron is transferred from one metal to another. It is a sort of radiation induced redox process that can generate a charge transfer state, with interesting consequences on the emission dynamics of the system [9, 10]. All absorption bands due to these types of transitions are usually rather broad.

1.5 The luminescent center

Fig. 2.5 shows the configurational coordinate diagram with an offset between the parabolas of the ground and the excited state. As discussed in Sect. 1.2 the absorption results in populating a high vibrational level of the excited state. The system first relaxes to the lowest vibrational level of the excited state releasing the excess energy to the surroundings. This relaxation is very fast, its rate being of the order of 10^{13} s^{-1}, then it is reasonable to suppose that it takes place in absence of emission processes (a very fast emission has a rate of 10^{8} s^{-1}). From the lowest vibrational level of the excited state the system can radiatively decay to the ground state. The selection rules for the absorption and emission process are the same, with the difference that the emission occurs spontaneously, whereas for the absorption a radiation field must be present.

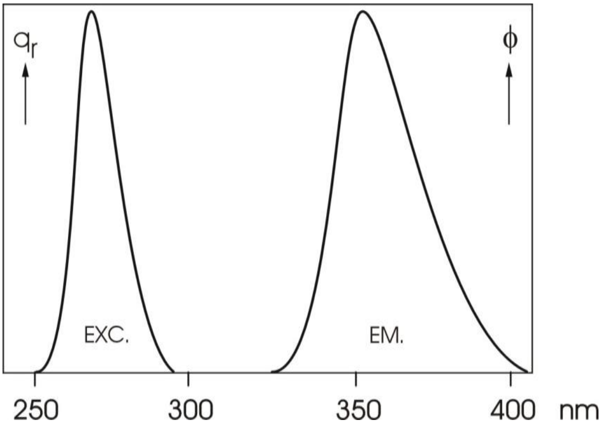

Fig. 1.10. Example of emission and excitation spectra in the $\Delta R \neq 0$ case.

The emission process results in populating a high vibrational level of the ground state. The system successively relaxes to the lowest vibrational level of the ground state. As a consequence, the emission occurs at lower energy than the absorption transition (see Fig. 1.10 as an example). The energy difference between the maxima of the excitation and emission band is referred to as the Stokes shift. It is obvious that the larger the ΔR is, the larger the Stokes shift and the broader the optical bands are. If the two parabolas have equal force constants (the same shape), the amount of energy lost in the relaxation process is $Sh\nu$, where $h\nu$ is the separation between two vibrational levels and S an integer. The Stokes shift amounts to $2Sh\nu$. The constant S is called the Huang-Rhys coupling constant. It is proportional to (ΔR^2) and measures the strength of the electron-lattice coupling. On the basis of the value of S, three cases can be individuated:

$S < 1$ - weak-coupling regime: the absorption and emission transition will consist of sharp zero-phonon lines. Weak vibrational sideband will be observable at low temperature in some cases (Fig. 1.11a).

1< S < 5 - intermediate-coupling regime: the optical bands will have a limited broadness. In the low temperature spectra it will be possible to observe the zero-phonon line and a vibronic structure. (Fig. 1.11b).

S> 5 - the strong-coupling regime: the zero-phonon line is absent, only broadbands will be observed in both absorption and emission spectra. (Fig. 1.11c).

Whereas in absorption spectroscopy the strength of the optical absorption is easily measurable, this is more complicate in the case of the emission spectroscopy. Here the key property is the lifetime of the excited state. For allowed emission transitions the lifetime is short, around 10^{-7}-10^{-8} s, whereas for strongly forbidden transitions in solids it is much longer, of the order of 10^{-3} s. The measure of the lifetime is of great importance.

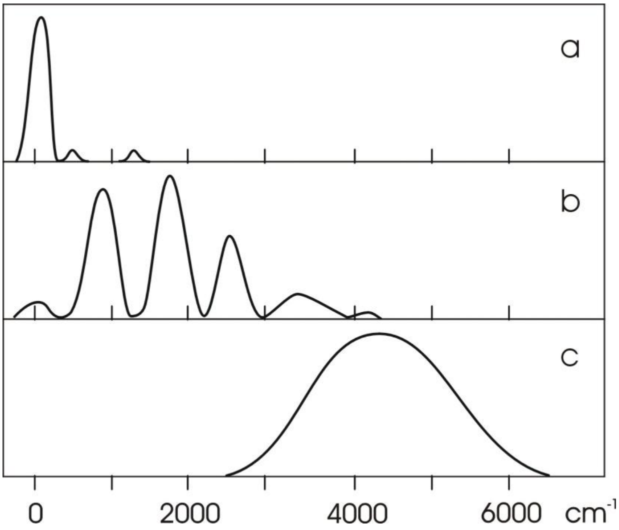

Fig. 1.11. Examples of emission profiles. (a) weak coupling regime; (b) intermediate coupling regime; (c) strong coupling regime. The position of the zero-phonon line is always at 0 cm^{-1}. In (a) the zero-phonon line dominates ($S\sim 0$), in (b) it is still observable ($S\sim 2$) and in (c) it is vanished ($S>5$).

For the two level system of Fig. 1.5 the population of the excited state decreases according to:

$$\frac{dN_e}{dt} = -N_e \cdot P_{eg} \qquad (1.8)$$

where N_e is the number of luminescent ions in the excited state after an excitation pulse, t the time, and P_{eg} the probability for spontaneous emission from the excited to the ground state. Integration yields:

$$N_e(t) = N_e(0)e^{-P_{eg}t} \qquad (1.9)$$

which is also written as:

$$N_e(t) = N_e(0)e^{-t/\tau_R} \qquad (1.10)$$

where τ_R $(=P_{eg}^{-1})$ is the radiative decay time. A plot of the logarithm of the intensity versus time should give a linear curve.

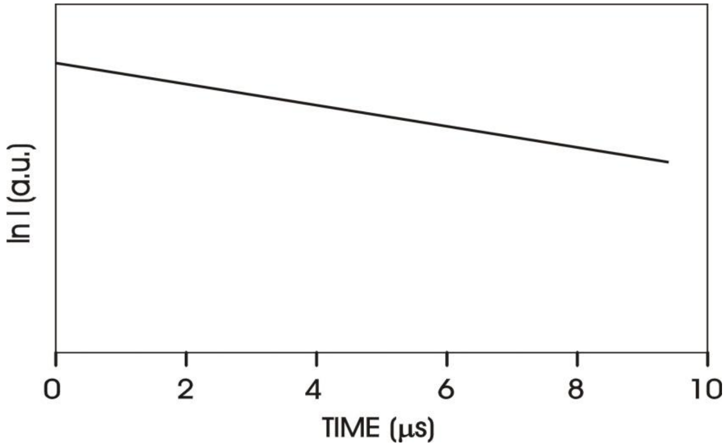

Fig. 1.12. Exponential decay curve. The luminescence intensity I is plotted logarithmically versus the time after the excitation pulse.

An example is shown in Fig. 1.12. After a time τ_R the population of the excited state has decreased to *1/e* (37%).

1.6 The rare earth emission

The energy levels of the trivalent rare earth ions which arise from the $4f^n$ configuration are given in Fig. 1.9. The electron-phonon coupling is weak, $\Delta R=0$ and $S<1$, and the intraconfigurational emission transitions consist of manifolds constituted of sharp lines, whose separation is of the order of the hundreds of cm^{-1}. These transitions are parity and often also spin forbidden, then they are usually weak and characterized by relatively long lifetimes ($\sim 10^{-3}$-10^{-6} s). The composition (Stark splitting) of the emission (and absorption) manifolds reflects the geometry of the crystal field acting on the active ion and can be analyzed by means of group theoretical considerations. The luminescence dynamics of the lanthanide ions are often rather complex in consequence of the high number of states and processes involved. In the following we present a summary of the relevant emission properties of the rare earth ions investigated in the present thesis [11].

Pr^{3+} $(4f^2)$

The most interesting emission transitions of Pr^{3+} are in the visible region (Fig. 1.13), in particular in the blue-green ($^3P_0 \rightarrow {}^3H_4$) and red ($^3P_0 \rightarrow {}^3H_6$, $^3F_2$; $^1D_2 \rightarrow {}^3H_4$) regions. The relative intensities of these transitions depends on the host lattice and on the doping concentration. In addition, Pr^{3+} shows some tendency to oxidize and to form the Pr^{4+} ion. When accommodated into an oxidizing host lattice (vanadates, tungstates, niobates, etc.) it can give rise to a photoinduced redox mechanism resulting in the formation of a charge transfer state (IVCT) than can influence the emission dynamics of the system.

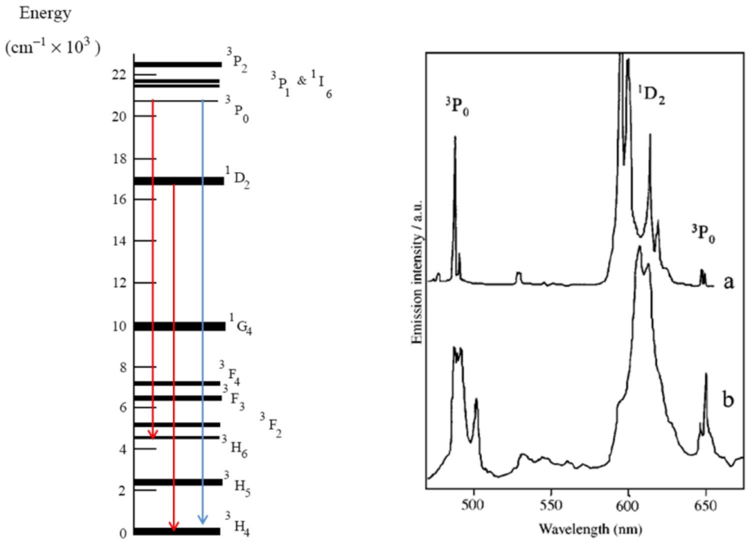

Fig. 1.13. Energy levels scheme of Pr^{3+} in solids (left) and emission spectra of $YVO_4:Pr^{3+}$ (upper curve) and $LaVO_4:Pr^{3+}$ (lower curve) (right).

The decay time of the $^3P_0$ emission is short, of the order of some microseconds. This is a consequence of the fact that the transitions from this state are spin allowed, and, in addition, that the *4f* orbitals are probably more spread out in the lighter rare-earth ions like Pr^{3+} (with lower nuclear charge), and this favors the mixing with opposite parity states.

Nd^{3+} ($4f^3$)

Nd^{3+} emits in the NIR region, and its transitions are important for laser applications. They are shown in Fig. 1.14. The $^4F_{3/2} \rightarrow {}^4I_{11/2}$ channel at 1060 nm is the most widely used in the realization of solid state laser devices.

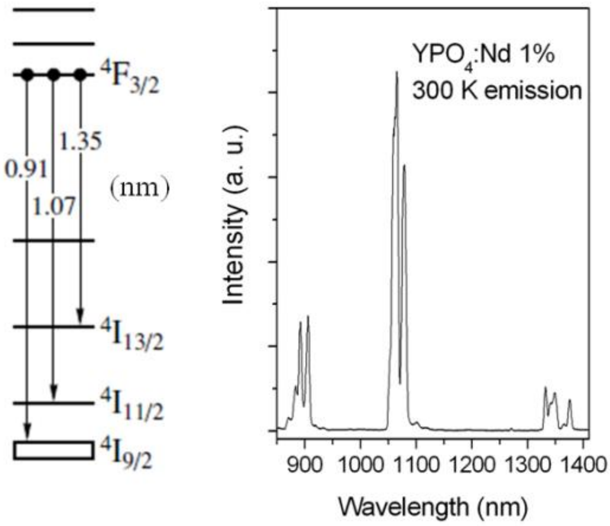

Fig. 1.14. Energy levels scheme of Nd^{3+} in solids (left) and emission spectrum of $YPO_4:Nd^{3+}$ (right).

The transitions from the $^4F_{3/2}$ level are spin allowed and scarcely affected by non radiative processes. The decay times are rather long (hundreds of μs) and relatively independent on the temperature.

Sm^{3+} ($4f^5$)

The emission of Sm^{3+} is situated in the orange-red spectral region (Fig. 1.15) and consists of transitions from the $^4G_{5/2}$ level to the ground state $^6H_{5/2}$ and higher levels ^6H_J ($J = 7/2, 9/2, 11/2$). Since the gap between the emitting and the lower-lying level is rather large, the emission is efficient and marginally affected by non radiative processes. Despite this, Sm^{3+} is much less popular with respect other red emitting ions like Eu^{3+} in consequence of the minor spectral purity and of the less favorable excitation conditions. Nevertheless, the interest towards Sm^{3+} doped materials is increasing because its low cost and some interesting applicative and theoretical aspects.

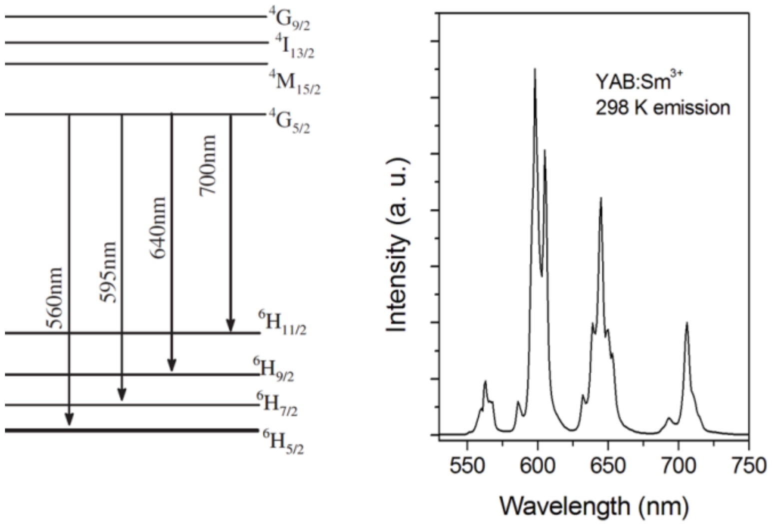

Fig. 1.15. Energy levels scheme of Sm^{3+} in solids (left) and emission spectrum of YAB:Sm^{3+} (right).

Eu^{3+} ($4f^6$)

Eu^{3+} is commercially important for the realization of red emitting phosphors. The most interesting luminescence channel is $^5D_0 \rightarrow {}^7F_2$, that is a hypersensitive transition and then its intensity strongly depends on the host material (see Fig. 1.16 for example). Conversely, the $^5D_0 \rightarrow {}^7F_1$ transition is allowed for the magnetic dipole mechanism and then it is relatively host insensitive. The other transitions are weaker, in particular the $^5D_0 \rightarrow {}^7F_0$ is both spin and symmetry forbidden and it is sometimes barely visible only because of J-mixing. The emission decay time is of the order of some milliseconds, being the involved transitions spin forbidden and not affected by multiphonon relaxation processes.

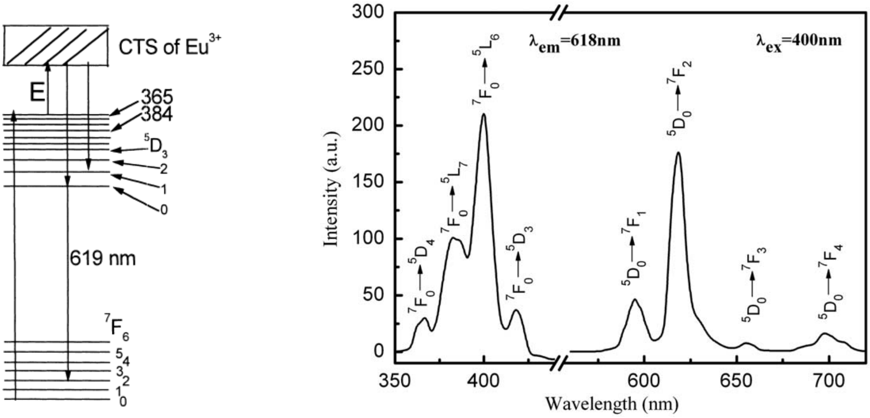

Fig. 1.16. Energy levels scheme of Eu^{3+} in solids (left) and emission spectrum of CTO:Eu^{3+} (right).

Tb^{3+} ($4f^8$)

The emission of Tb^{3+} is due to transitions $^5D_4 \rightarrow {}^7F_J$ which are mainly in the green region. Often there is a considerable contribution to the emission from the higher energy $^5D_3 \rightarrow {}^7F_J$ transitions, mainly in the blue.

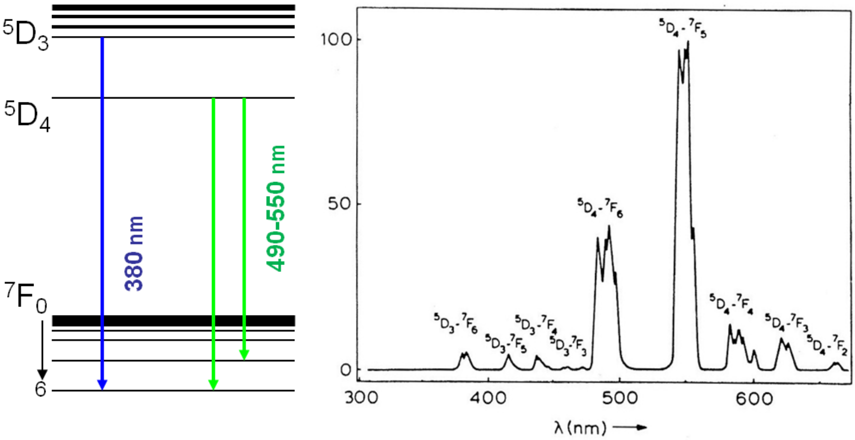

Fig. 1.17. Energy levels scheme of Tb^{3+} in solids (left) and emission spectrum of $GdTaO_4$:Tb^{3+} (right).

Fig. 1.17 reports the energy levels scheme of $Tb^{3+}$and an example of an emission spectrum. Since the J values, involved in the transitions, are high, the crystal field splits the levels in many sublevels which gives the spectrum its complicated structure. The relative intensity of the emission from the $^5D_3$ and from the $^5D_4$ level depends on the doping level.

Dy^{3+} ($4f^9$)

The visible emission of Dy^{3+} originates from the $^4F_{9/2}$ level. The most intense transitions are the $^4F_{9/2}\rightarrow{}^6H_{15/2}$ (~ 470 nm) and $^4F_{9/2}\rightarrow{}^6H_{13/2}$ (~ 570 nm). They are shown in Fig. 1.18, together with a typical emission spectrum. Their relative intensity depends on the characteristics of the host material. The luminescence has a whitish color which turns to yellow in host lattices where the hypersensitivity is pronounced. The decay times are of the order of hundreds of microseconds, and often tend to increase with the temperature, for reasons that have yet to be fully understood.

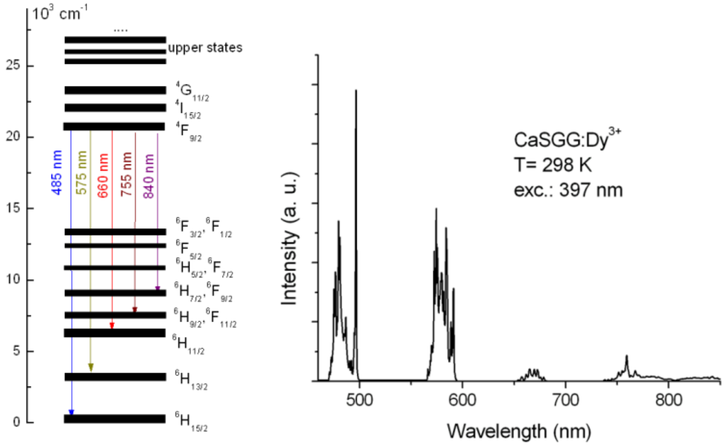

Fig. 1.18. Energy levels scheme of Dy^{3+} in solids (left) and emission spectrum of CaSGG:Dy^{3+} (right).

1.7 Emission properties of d^0 ions

Complexes of transition metal ions with a d^0 electronic configuration show often intense broad band emission with a large Stokes shift (10000 – 20000 cm^{-1}). Examples are VO_4^{3-}, NbO_6^{7-}, WO_4^{2-}, WO_6^{6-} [3]. The excited state a charge-transfer state in which an oxygen *2p* electron is transferred into one of the empty *5d* orbitals of the central metal ion. This implies a considerable amount of electronic reorganization resulting in large values of ΔR and of the Stokes shift, and consequently the optical bands are broad. The emitting state is a spin triplet, then the emission transition is spin forbidden. As a consequence the lifetimes are long, of the order of the hundreds of μs. Octahedral complexes have a smaller Stokes shift than the tetrahedral ones, and their luminescence is usually weaker.

The presence of ions with low-lying energy levels, for example ions with s^2 configuration, drastically influences the d^0-complex luminescence. For example, $CaWO_4:Pb^{2+}$ shifts its emission to longer wavelength relative to undoped $CaWO_4$ and the quenching temperature increases. Another example is $YVO_4:Bi^{3+}$ which has a yellow emission whereas YVO_4 has blue emission. This aspect has been extensively dealt with in the frame of the present work (Sect.5).

1.8 Emission properties of s^2 ions

The emission properties of the ions with outer s^2 configuration originate in the $^3P_1$ level and strongly depend on the host material. For instance, the Stokes shift between the absorption and emission bands of Bi^{3+} ranges from 800 to 20000 cm^{-1}, depending on the host lattice. This large variation has been ascribed to the amount of space available for the Bi^{3+} ion in the lattice.

The small Stokes shift case is observed only for six-fold coordinated Bi^{3+}. The Bi^{3+} ion is too large for six coordination and has no possibility to relax to a different equilibrium distance. In a larger site the situation is different. It has been proposed that in the ground state the Bi^{3+} goes off center when there is enough space, in order to realize its preferred asymmetrical coordination. The optical transitions are followed by relaxation processes resulting in a large Stokes shift.

1.9 Nonradiative transitions in an isolated luminescent center

The radiative return from the excited state to the ground state is always accompanied by non-radiative processes. Since one of the most important requirement for a luminescent material is a high light output, it is imperative that in such a material the radiative processes have a much higher probability than the non-radiative ones. In this section we will deal with the main radiationless processes of an excited isolated center [11].

In the configurational coordinate scheme of Fig. 1.19a the absorption and emission transitions can take place and will be separated by a Stokes shift.

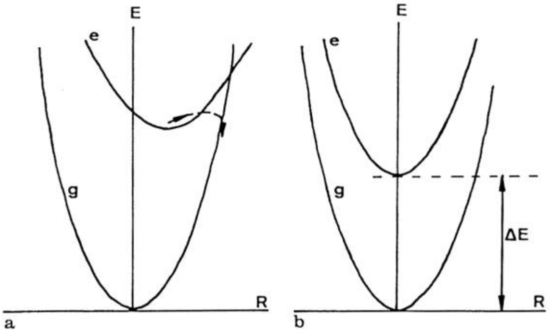

Fig. 1.19. Configurational coordinate diagrams illustrating non radiative transitions. The ground state parabola is indicated by ***g***, the excited state parabolas by ***e*** and ***e′***. In (a) the arrow indicates a nonradiative transition from ***e*** to ***g***.

However if the temperature is sufficiently high to populate the energy levels located in proximity or above the crossing point between the two parabolas, the system will relax non-radiatively through the vibrational levels of the electronic ground state. This model accounts for the thermal quenching of luminescence. The probability of this process increases as the offset between the two parabolas increases. In the $S=0$ case (Fig. 1.19b) this mechanism is not possible, since the parabolas cannot cross. However, if the separation between the two minima, ΔE, is equal to or less than 4-5 times the higher vibrational frequency of the surroundings, this amount of energy can simultaneously excite a few high-energy vibrations and is then lost for the radiative process. Usually this non-radiative process is called multi-phonon relaxation. It is a very important depopulation mechanism, that has been extensively studied. Its temperature dependence is characteristic and can be expressed by:

$$W(T) = W(0)(n+1)^P \qquad (1.11)$$

where $W(T)$ is the rate at temperature T, $p= \Delta E/h\nu$, ΔE the energy difference between the levels involved, and

$$n = [\exp(\frac{\Delta \nu}{KT} - 1]^{-1} \qquad (1.12)$$

$W(0)$ is large for low p, i. e. for small ΔE or high vibrational frequencies. Further:

$$W(0) = \beta \exp[-(\Delta E - 2h\nu_{\max})\alpha] \qquad (1.13)$$

with α and β constants, and $\nu_{\max}$ the highest available vibrational frequency of the surroundings of the rare earth ion. This is the energy-gap law, that allows the calculation of W with an accuracy of one order of magnitude.

1.10 Energy transfer

In addition to radiatively and nonradiatively emission, the return to the ground state can occur by the transfer of the excitation energy from the excited center (S^*) to another center (A):

$$S^* + A \rightarrow S + A^*$$

The energy transfer may be followed by emission from A. The S center is then said to sensitize the A center. A^* may also decay non-radiatively; in this case A is referred to as a quencher of the S emission. The energy levels of the two centers, separated in a solid by distance R, are schematized in Fig. 1.20. Energy transfer can occur only if the energy differences between the ground and the excited states of S and A are equal (resonance condition) and if R is short enough to allow interaction between the two centers. The interaction may be either an exchange interaction (if there is overlap of the wave functions) or an electric or magnetic multipolar interaction. In practice the resonance condition can be tested by considering the spectral overlap of the S emission and the A absorption spectra. The Dexter expression for the transfer probability is [12]:

$$P_{SA} = \frac{2\pi}{h} |< S, A^* | H_{SA} | S^*, A >|^2 \int g_S(E)\, g_A(E)\, dE \qquad (1.14)$$

where H_{AS} is the interaction Hamiltonian and the overlap integral reflects the requirement of energy conservation. $g_S(E)$ and $g_A(E)$ are the normalized shape function of the S emission and A absorption bands. The transfer rate P_{SA} vanishes for vanishing spectral overlap. The dependence of the transfer rate on the distance R depends on the type of interaction. For electric multipolar interaction the distance dependence is given by R^{-n} (n = 6, 8, … for electric-dipole electric-dipole interaction, electric-dipole electric-quadrupole interaction, …). For the exchange interaction the distance dependence is exponential, since it requires overlap of the wave functions. Only for some specific cases the type of interaction is known. The distance between sensitizer and activator plays then a key role in the energy transfer process. An important parameter has been defined in this connection: the critical distance for energy transfer R_C. It is the distance for which the transfer rate P_{SA} equals P_S, the rate of the radiative emission from the sensitizer S. For $R > R_C$ radiative emission from S prevails, whereas for $R < R_C$ the energy transfer from S to A prevails. If we consider transfer between two identical ions, S and S, there is no reason why the transfer should be restricted to one step, so that the first transfer step is followed by many others. This can bring the excitation energy far from the site where the excitation took place, i. e. there is energy migration. If in this way the excitation energy is transferred to a site where it is lost non-radiatively (killer or quenching site), the luminescence efficiency of that composition will be low. This phenomenon is called concentration quenching. This type of quenching will not occur at low concentrations, because the average distance between the S ions is so large that the migration is hampered.

At first sight, energy transfer between identical rare earth ions seems to be a process with a low rate, because their interaction will be weak in view of the well-shielded character of the *4f* electrons.

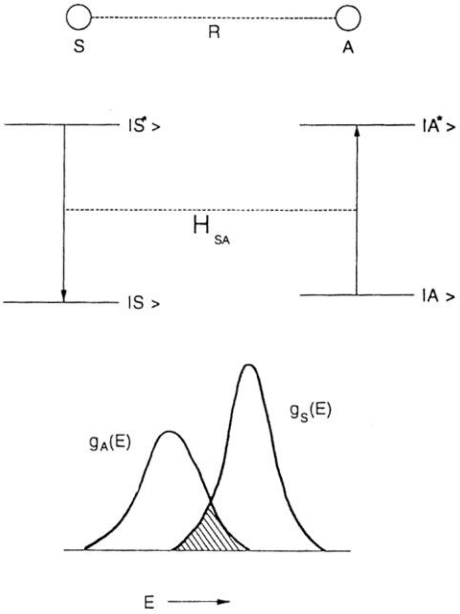

Fig. 1.20. Energy transfer between the *S* and *A* centers. The two centers are at distance *R* (top). The energy levels schemes and the interaction H_{SA} are given in the middle. The spectral overlap is illustrated at the bottom.

However, although the radiative rates are small, the spectral overlap can be large. This originates from the fact that $\Delta R \approx 0$, so that the absorption and emission lines will coincide. Further the transfer rate will easily surpass the radiative rate, since the latter is low. In fact energy migration has been observed in many rare earth compounds, and concentration quenching usually becomes effective for concentrations of a few atomic percent of dopant ions. Energy transfer over distances of up to some 10 Å is possible. The energy transfer processes are usually investigated by means of pulsed light and site selective measurements. The shapes of the decay curves are in fact characteristic of the physical processes. Let suppose to have a compound activated with a rare earth ion *S* and containing also some ions *A* able to trap the excitation energy of *S* by *SA* transfer. Different cases are possible:

1. if the *S* excitation results in the emission from *S* only, both in absence of in presence of migration, the decay is exponential:

$$I = I_0 \exp(-\gamma t) \qquad (1.15)$$

where I_0 is the emission intensity at time $t = 0$ (immediately after the pulse), and γ is the radiative rate.

2. if some *SA* transfer occurs, but no *SS* transfer at all, the *S* decay is given by the Inokuti-Hirayama equation [13]:

$$\phi(t) = A\exp\left[-\frac{t}{\tau} - \alpha\left(\frac{t}{\tau}\right)^{3/s}\right] \qquad (1.16)$$

where $\phi(t)$ is the emission intensity after pulsed excitation, *A* is the intensity of the emission at $t=0$, τ is the lifetime of the isolated donor, α is a parameter containing the energy transfer probability and $s=6$ for dipole–dipole (*D*–*D*), 8 for dipole–quadrupole (*D*–*Q*) and 10 for quadrupole–quadrupole (*Q*–*Q*) interaction. Immediately after the pulse the decay is faster than in the absence of *A*. This is due to the presence of *SA* transfer. After a long time the decay becomes exponential with the radiative rate as a slope. This represents the decay of *S* ions which do not have *A* ions in the surroundings. The parameter α provides information on the probability of the energy transfer process

$$\alpha = \frac{4}{3}\pi\Gamma\left(1-\frac{3}{s}\right) N_a\, R_0^3 \qquad (1.17)$$

where Γ is the gamma function, N_a the concentration of the acceptor expressed in ions·cm^{-3} and R_0 is the critical distance for the transfer.

3. in case of migration the analysis is more difficult and it is necessary to individuate some limit cases. This is beyond the scope of the present thesis and will not be discussed further.

The complex energy levels structure of the rare earth ions allows to realize particular types of energy transfer processes that strongly influences the dynamics of the system [14].

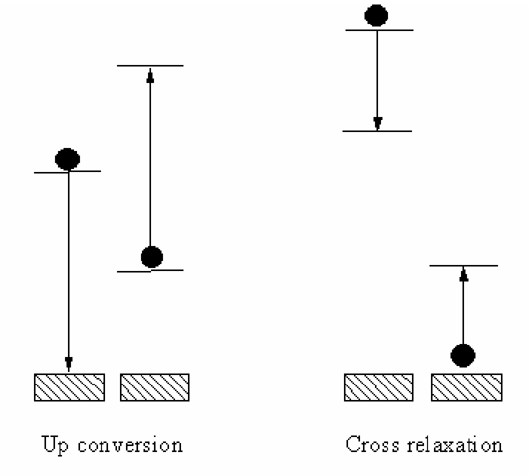

Fig. 1.21 Up conversion and cross relaxation processes.

The *up conversion* consists of a energy transfer to an excited center that will be raised to an excited level located at higher energy with respect the original one, followed by emission at a wavelength shorter than that of the absorbed radiation. The *cross relaxation* mechanism occurs when an excited donor decays to a lower excited state and transfers part of its excitation energy to an acceptor that will be raised to an excited level lower than the starting one.

References

[1] G. Blasse, A. Grabmaier, ‘Luminescence Materials’, (Springer Verlag, Berlin Heidelberg 1994).

[2] B. Henderson, G. F. Imbusch, Contemp. Phys. 29 (1988) 235.

[3] G. Blasse, Struct. Bond. 42 (1980) 1.

[4] S. Hüfner, ‘Optical Spectra of Transparent Rare Earth Compounds’ (Academic Press, New York 1978).

[5] B. R. Judd, Phys. Rev. 127 (1962) 750.

[6] G. S. Ofelt, J. Chem. Phys. 37 (1962) 511.

[7] R. D. Peacock, Struct. Bond. 22 (1980) 83.

[8] G. Boulon in ‘Spectroscopy of Solid-State Laser-Type Materials’ ed. B. Di Bartolo (Plenum Press, New York 1987) pag. 223.

[9] P. Boutinaud, P. Putaj, R. Mahiou, E. Cavalli, A. Speghini, M. Bettinelli, Spectroscopy Letters 40 (2007) 209.

[10] P. Boutinaud, E. Cavalli, Chem. Phys. Lett. 503 (2011) 239.

[11] B. Henderson, G. F. Imbusch, ‘Optical Spectroscopy of Inorganic Solids’ (Clarendon Press, Oxford 1989).

[12] R. C. Powell, G. Blasse, Struct. Bond. 42 (1980) 43.

[13] M. Inokuti, F. Hirayama, J. Chem. Phys. 43 (1965)1978.

[14] Kaminskii A A, Crystalline Lasers: Physical Processes and Operating Schemes (CRC Press, Boca Raton, Fla. 1996).

Chapter 2

Experimental section

2.1 Synthesis

Pechini method

The Pechini method was proposed in 1967 as a technique for depositing dielectric films of lead and alkaline-earth titanates and niobates in the production of capacitors. Later, the process was customized for the synthesis of multicomponent finely dispersed oxide materials. It consists in the formation of complexes of metal ions with bi- and tridentate organic chelating agents such as citric acid. A polyalcohol such as ethylene glycol is then added to establish linkages between the chelates by a polyesterification reaction, resulting in gelation of the reaction mixture [1].

Variations of the method mostly involve the substitution of citric acid with alternative chelating agents, such as ethylenediaminetetraacetic acid (EDTA), oxalic acid, polyvinyl alcohol (PVA) etc.. Today, the Pechini route is widely used in the synthesis of dielectric, fluorescent and magnetic materials, high-temperature superconductors and catalysts, as well as for the deposition of oxide films and coatings.

Positive aspects of this technique include the low temperature required for the thermal treatments, the formation of particles in the nanoscale range with homogeneous size and distribution and the possibility to obtain transparent thin films. Moreover the Pechini method does not requires the use of organic solvents, with evident advantages in terms of final cost and environmental sustainability. On the other hand, the method does not allow a reliable control of the particle shape and morphology, and the control of the particle size is mainly achieved through the variation of the calcination conditions. In the standard procedure (shown in Fig. 2.1) the starting materials are mixed in stoichiometric amounts, dissolved in an appropriate solvent (nitric acid) and then chelated with citric acid in order to stabilize the solution. A polyethylene glycol with high molecular weight is then added to form a polymeric matrix. The obtained gel is dried at 80 °C in oil bath in order to remove the excess of nitric acid. Successively a thermal treatment at 500 °C induces the pyrolysis of the polymeric matrix and of the citric acid. The target compound is finally obtained after calcination and sintering at 900 °C.

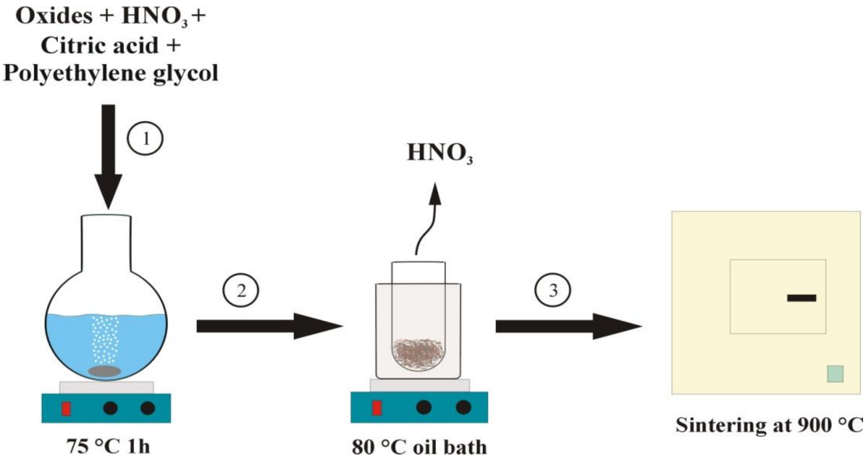

Fig. 2.1. The Pechini method: (1) Dissolution of starting materials. (2) Evaporation of the nitric acid to obtain the gel. (3) Sintering of the nanoparticles at high temperature.

Solid state reaction

In the solid state reaction the starting materials are thoroughly mixed in stoichiometric amount in an alumina crucible and then heated to a temperature usually ranging from 1000 to 1500 °C, depending on the reactivity of the reagents. It is the most widely used method for the preparation of polycrystalline solids starting from simple oxides (or nitrates, carbonates, etc.) in powder form. At room temperature the reaction practically does not proceed, then it is necessary to heat the mixture to considerably high temperature in order to achieve an appreciable rate. Both thermodynamic and kinetic aspects are important in the solid state reactions; the former is correlated to the energy balance of the process, the latter to its rate and mechanism [2]. In this connection, the diffusion processes play a key role, since the ions have to move through the lattice in order to reach the reaction site. The kinetics of the solid state reactions are therefore largely dependent on the structural properties.

The solid state reaction method does not require the use of solvents, does not imply the production of chemical waste and it is relatively inexpensive. The sintering temperatures and the reaction times are however significantly higher than those applied, for instance, in the sol-gel route, and the control of the particle morphology is much more difficult.

Hydrothermal synthesis

The term ‘hydrothermal’ is of geological origin. It was first used by the British geologist, Sir Roderick Murchison (1792-1871) to describe the role of the water at elevated temperature and pressure in the formation of various rocks and minerals in the earth’s crust. The hydrothermal chemistry has been extensively developed for the synthesis of nanostructured materials which are difficult to obtain by high temperature solid state reactions [3]. It is nowadays applied in the processing of advanced inorganic materials for applications in electronics, optoelectronics, catalysis, ceramics, etc..

A hydrothermal processing can be defined as any heterogeneous reaction in the presence of aqueous solvents or mineralizers under high pressure and temperature conditions to dissolve and recrystallize materials that are relatively insoluble under ordinary conditions. Sometimes the chemists prefer to use the word ‘solvothermal’, referred to a chemical reaction in the presence of a non-aqueous solvent or solvent in supercritical or near supercritical conditions. A fluid is in the supercritical domain when both pressure and temperature are above their critical values, $P\mathrm{c}$ and $T\mathrm{c}$. These fluids possess physicochemical properties, such as density, viscosity and diffusivity, which are intermediate between those of liquids and gases. The main interest in supercritical fluids as reaction media relies on their continuously adjustable properties from gas to liquid with small pressure and temperature variations. Usually the preparation of materials in supercritical fluids involves three steps:

1) solubilization of solutes in dense fluid;
2) transformation of fluids in the supercritical domain, characterized by specific properties;
3) materials recovery in the low density fluid domain order to obtain dry materials.

Fig. 2.2 shows the details of a typical hydrothermal procedure adopted in this Thesis work. The starting materials are dissolved in diluted nitric acid (1) and the obtained mixture is poured into a Teflon-lined stainless steel autoclave (60% filling) and heated at 180 °C for 12 h (2). The resulting suspension is then washed several times with distilled water and then centrifuged (3). The separated powder is dried at 120 °C for 1 h and finally heated at 500 °C for 2h (4).

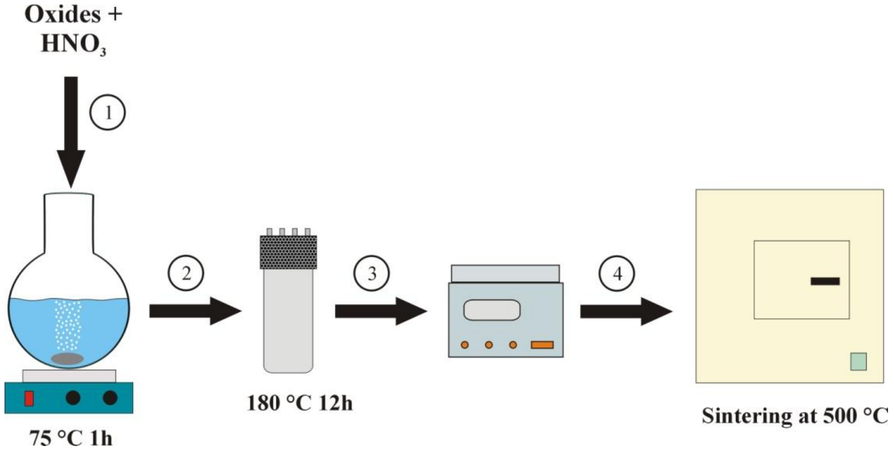

Fig. 2.2 General hydrothermal procedure for the synthesis of oxide materials.

The hydrothermal method allows to obtain materials with high purity and homogeneity, good crystallinity and narrow particle size distribution in the sub-micron to nano range. It does not require high sintering temperature and it is suitable for processing a wide range of chemical compositions through single-step processes, using a simple equipment, with low energy consumption and fast reaction times. On the other hand, the use of expensive autoclaves can constitute a serious drawback specially in case of massive production.

Flux growth

The crystals used in this work were grown by means of the “flux growth” method, consisting in the slow cooling of suitable molten salts solutions [4]. The crystals grow by spontaneous nucleation at a temperature much below its melting point, thanks to the presence of the high temperature solvent. There are different reasons leading to prefer the flux method rather than other techniques. The most important are:

- The melting point of the desired material is too high for the available experimental apparatus.
- The material melts incongruently.
- The material is non-stoichiometric at its melting point.
- High quality crystals are required, the quality of the crystals obtained by this technique is often better than that obtained by any other method.
- The flux growth is relatively inexpensive and very versatile with respect to other growth methods.

In principle it is possible to find a solvent for every kind of material and there are no limits to its potential applications. There is in fact a wide choice of suitable fluxes and the criteria for the identification of the optimum solvent for the growth of a given crystal have not yet been established with precision. In this context, the lack of information about the phase diagrams, the viscosities and the vapor pressures of possible fluxes play an important role. The basic requirements for a good flux are:

- Low melting temperature;
- High solubility for the solute, without forming a stable compound;
- Very low solubility for platinum or other crucible material;
- Low volatility in the working temperature range;
- Easy to be prepared and to be separated from the crystals;
- Low toxicity.

Other aspects have to be taken into account. For instance, the presence of a common ion with the solute is certainly an advantageous condition, since it excludes at least in part the contamination of the growing crystals by the solvent constituents. Moreover, a mixture of different fluxes often allows a better compromise between different requirements to be achieved like, for example, good solubility and low volatility, with respect to the use of pure solvents. In general, an eutectic composition represents the most suitable choice, if the required material crystallizes as the stable solid phase. It is also important that the flux does not contain ions which may enter the crystal lattice substitutionally and/or which can form stable compounds with the solute constituents.

Tab. 2.1. Fluxes commonly used for the growth of crystals.

Flux	**Melting point/eutectic**	**Room temperature solvent**
BaO/Ba_2O_3	870	HNO_3
$BaO/Bi_2O_3/B_2O_3$	600	HNO_3
$Bi_8V_2O_{17}$	900	HNO_3
$Li_2O/MoO3$	532	H_2O
$Na_2B_4O_7$	741	HNO_3
$Na_2W_2O_7$	620	H_2O
Pb_2F	840	HNO_3
PbO/B_2O_3	500	HNO_3
PbO/PbF_2	494	HNO_3
$PbO/PbF_2/B_2O_3$	494	HNO_3
$Pb_2P_2O_7$	824	HNO_3
$Pb_2V_2O_7$	720	HNO_3

From these considerations, it is evident that it is not easy to establish 'a priori' the best batch composition for the growth of a new crystal. Information concerning the phase diagrams and/or the growth of similar materials, if available, can provide useful indications. Table 4.1 shows a list of the most popular fluxes. In order to avoid evaporation the majority of these fluxes must be used in sealed crucibles, only BaO/Ba_2O_3, $BaO/Bi_2O_3/B_2O_3$, $Bi_8V_2O_{17}$ and $Pb_2V_2O_7$ are sufficiently non-volatile to be used in non-sealed crucibles. At the end of the growth, the crystals are separated from the flux by dissolving it in suitable acid or basic solutions in which the crystals are not attacked. The growth experiments are carried out in programmable muffle furnaces with crusilite (silicon carbide) heating elements, suitable for temperatures up to 1450 °C. A Pt/Pt(Rh) thermocouple is used for the control of the temperature. The heating/cooling cycle is controlled by suitable programs. The details of thermal cycles for the growth of the crystals studied in this work will be reported in the respective experimental sections together with the compositions of the starting mixtures. In general, a thermal cycle implies the heating of the mixture at a rate ranging from 10 to 70°C/h up to the melting temperature, a 'soaking time' of approximately 6-24 h in order to favor the homogenization of the melt, and finally the cooling at a rate of 0.5-5 °C/h, during which the crystals spontaneously nucleate and grow. These experiments take from one to three weeks, depending on the case. The flux growth method allow to grow of crystal of small size, of the order of some mm^3, then suitable for spectroscopy and other experiments, but not for device applications. This also because the crystals can contain inclusions (usually from the flux), the control of the doping level can be rather difficult and the reproducibility of the experiments is not always good. For these reasons it is considered a good solution more for research than for practical purposes.

2.2 Morphological and structural characterization

Scanning electron microscopy

The scanning electron microscope (SEM) is an instrument that produces a largely magnified image by using electrons instead of light [5]. A focused beam of high-energy electrons interacts with the sample generating different signals including secondary electrons, backscattered electrons, diffracted backscattered electrons, photons, characteristics X-rays, etc. These signals can be detected and provide information about the morphology and the composition of the sample surface. Fig. 2.3 shows the main constituents of a SEM. The electron gun at the top of the microscope (1) generates a beam of electrons (2) that passes through a system of electromagnetic fields and lenses (3) that focuses it onto the sample (4). The ejected X-rays, backscattered electrons, and secondary electrons are collected on the detector (5) and converted into a signal that is sent to a screen similar to a television screen (6) to produce the final image. The whole setup is maintained under high vacuum conditions. In order to avoid charge accumulation on the surface, the samples must be electrically conductive; nonconducting samples are often coated with an ultrathin coating of metal. The SEM technique has an extremely wide range of applications thanks to its versatility and to the possibility of obtaining different kinds of information in a short time.

On the other hand, a SEM apparatus is usually very expensive, large and must be housed in a special area free of any possible electric, magnetic or vibration interference. In addition, its use is limited to the study of solid samples that can be properly prepared and introduced into the vacuum chamber. The morphology of the phosphors particles investigated in this Thesis work was examined by means of a 515 Philips scanning electron microscope (SEM).

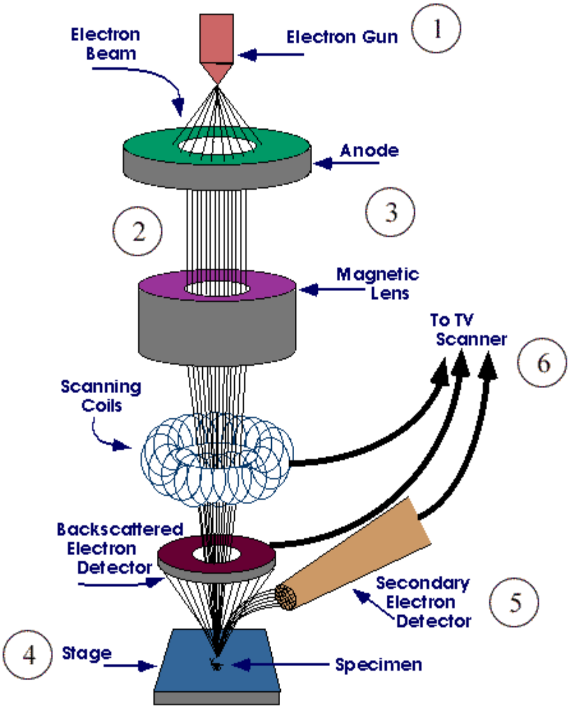

Fig. 2.3. Schematic representation of a scanning electron microscope.

X-ray powder diffraction

The X-ray powder diffraction technique is based on the interaction of a monochromatic X-ray beam with a crystalline sample in powder form [6]. The X-ray powder diffractometer is constituted of three main elements: a X-ray tube, a sample holder and a X-ray detector (see Fig. 2.4). The X-rays are generated by a cathode ray tube, filtered to produce monochromatic radiation (whose wavelength depends on the metal constituting the cathode) and collimated onto the sample. The interaction of the incident rays with the sample produces constructive interference (and a diffracted ray) when the Bragg's Law ($n\lambda=2d\sin\theta$) is satisfied. This law describes the relation between the wavelength λ of the electromagnetic radiation, the diffraction angle θ and the lattice spacing *d* in a crystalline sample. The diffracted X-ray is detected in the *2θ* range around the sample and processed. The diffracted intensity of the signal is then reported as function of the scattering angle in the diffractogram, that can be suitably analyzed or simply compared with standard reference patterns.

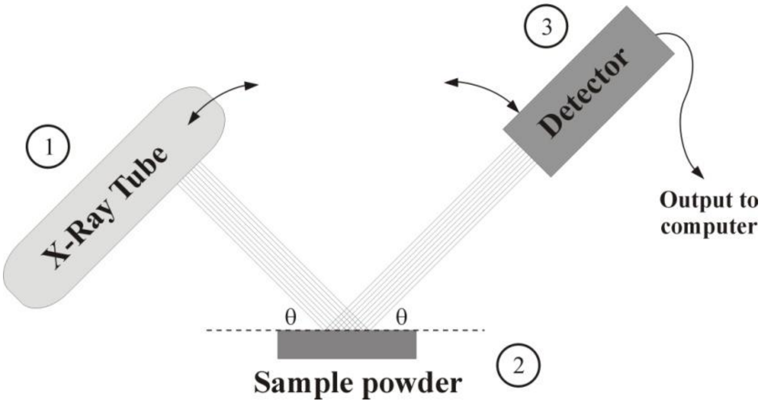

Fig. 2.4. Three main constituting elements of a powder X-ray diffractometers: X-ray tube (1), sample holder (2) and X-ray detector (3).

The powder X-ray diffraction allows for rapid, non-destructive analysis since it does not require particular sample preparation. It is extensively used in the structural characterization of the materials including phase identification (search/match), investigation of high/low temperature phases, solid solutions, determinations of unit cell parameters of new materials and evaluation of the sample purity. Our samples were characterized using a Thermo ARL X'tra diffractometer equipped with a Si(Li) Thermo Electron solid state detector with CuK_α radiation. Rietveld diffraction patterns were collected in the 5-120° 2θ range, with 0.02 step and counting time of 15s.

2.3 Optical spectroscopy measurements

The samples obtained with the synthetic methods above describe where characterized by optical spectroscopy measurements [7]. The typical spectroscopic characterization includes:

Room temperature emission spectrum: it provides information about the effective emission characteristics of the material. The spectrum is characteristic of the emitting substance and of the excitation conditions.

Room temperature excitation spectrum: it allows to individuate the effective excitation channels.

10 K excitation and emission spectra: they allow to investigate the Stark levels structure of the optical center. Moreover, considerations concerning the number and the width of the components of the observed manifolds can provide indications about the presence of non-equivalent active ions and of structural disorder. Finally, they provide information concerning the thermally induced emission processes.

Temperature dependent decay profiles measurements: they allow to evaluate the efficiencies of the emission channels and to investigate the mechanisms of the radiative and non-radiative processes.

A general scheme of a setup for photoluminescence measurements is schematized in Fig. 4.5. The sample (1) is excited with a xenon lamp (2), which is followed by the excitation monocromator (3) or a laser beam. The emitted light is collected by a focusing lens and analyzed by means of a second monochromator (4), followed by a suitable detector (5) connected to a computer.

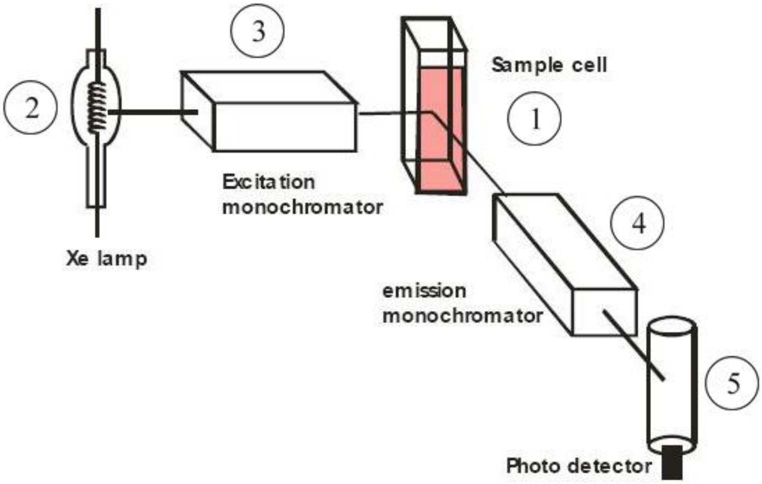

Fig. 4.5. General scheme of a setup for photoluminescence experiments.

Different experimental setups and arrangements have been used in the ambit of this thesis work, depending on the problem dealt with.

They will be described case by case in the following sections.

References

[1] B. L. Cushing, V. L. Kolesnichenko, C. J. O'Connor, Chem. Rev. 104 (2004) 3893.

[2] R. C. Ropp, 'Luminescence and the Solid State' (Elsevier Science Publisher B. V., 1991).

[3] K. Byrappa, T. Adschiri, Progr. Cryst. Growth Char. Mat. 53 (2007) 117.

[4] B. R. Pamplin, 'Crystal Growth' (Pergamon Press Ltd., Oxford 1975)

[5] J. I. Goldstein, D. E. Newbury, P. Echlin, D. C. Joy, C. Fiori, E. Lifshin, 'Scanning Electron Microscopy and X-Ray Microanalysis' (Plenum Press, New York 1981).

[6] M. M. Woolfson, 'An Introduction to X-Ray Crystallography' (Cambridge University Press 1997).

[7] J. García Solé, L. E. Bausá, D. Jaque, 'An Introduction to the Optical Spectroscopy of Inorganic Solids' (Wiley 2005).

Chapter 3

Dy^{3+} based phosphors for white light generation

3.1 Introduction

In the recent years the demand for environment-friendly technology is significantly increasing. The fossil fuel based industry consumes large amount of natural resources to produce energy, but more than half of them is wasted due to inefficient devices. Nowadays lightings constitute about 20% of total energy consumption in the world and in this context efficient lighting devices have a strategic roles to develop a sustainable technology. Fluorescent lamps for example are four times more efficient at least ten times more enduring than standard incandescent light bulbs. A fluorescent lamp is filled with a noble gas at a pressure of 400 Pa, containing 0.8 Pa mercury. In the discharge the mercury atoms are excited. When they return to the ground state, they emit (mainly) UV radiation. About 85 % of the emitted radiation is at 254 nm and 12 % at 185 nm. The remaining 3 % is found in the longer wavelength and visible region. The fluorescent lamp contains a phosphor or a mixture of phosphors that absorbs the 254 and 185 nm radiation and convert it into visible light. A lamp for lighting has to emit white light with a sun-like spectral distribution. White light phosphors are usually constituted by mixtures of blue and yellow/orange or of blue, green and red phosphors. All of them are in general rare earth containing materials. Blue light is mostly generated by means of Eu^{2+}-based phosphors, the yellow, red and green components by means of Ce^{3+}-, Eu^{3+}-, Tb^{3+}-based phosphors, respectively. The perspective of replacing a mixture of two or three phosphors with a single white light emitting material would be very attractive in terms of costs and processing. Recent studies have demonstrated that in Dy^{3+}-doped yttrium phospho-vanadate lattices the color of the luminescence can be suitably tuned by varying the host composition, opening the possibility of developing a white light emitting phosphor. Their emission spectra present the blue (480 nm), yellow (570 nm) and red (660 nm, weak) bands of Dy^{3+} superimposed to the blue host emission. Bao et al. [1] have synthesized a series of phosphors with general formula $Y_{1-y}Dy_y(P_xV_{1-x})O_4$ and investigated their luminescence properties as a function of the host composition and of the doping concentration, concluding that the $Y_{0.99}Dy_{0.01}(P_{0.8}V_{0.2})O_4$ system is very promising for applications as a white phosphor. Starting from these results we have decided to deepen the study of this kind of materials in order to better understand the effect of the host characteristics on the emission properties. We have taken into consideration three different synthetic methodologies and verified their impact on the luminescence performances. We have also investigated the processes governing the emission dynamics in these systems and pointed out the role of the host lattice characteristics formalized in the framework of the Judd–Ofelt theory.

3.2 Experimental

Synthesis

Y_2O_3 (Aldrich, 99.99%), $(NH_4)H_2PO_4$ (Merck, 99%), NH_4VO_3 (Riedel-deHaën, 98.5%) and Dy_2O_3 (Aldrich, 99.9%) were used as starting materials. A series of compounds with general formula $Y_{0.99}Dy_{0.01}(P_xV_{1-x})O_4$ (x=0, 0.2, 0.5, 0.8, 1) were synthesized ‘via’ solid state reaction: stoichiometric amounts of the precursors were thoroughly mixed in alumina crucible, pre-sintered at 500 °C for 2 h and then calcined at 1200 °C for 12 h. The hydrothermal and the sol–gel Pechini methods were then applied to the synthesis of the $Y_{0.99}Dy_{0.01}(P_{0.8}V_{0.2})O_4$ phosphor. The starting solution for both procedures was obtained after dissolution of the components in HNO_3 3 M at 75 °C under vigorous stirring and addition of citric acid as chelating agent. In the hydrothermal route, the obtained mixture was poured into a Teflon-lined stainless steel autoclave (60% filling) and heated at 180 °C for 12 h. The resulting suspension was then washed several times with distilled water and then centrifuged. The separated powder was dried at 120 °C for 1 h and then heated at 500 °C for 2 h and successively annealed at 900 °C for 2 h. In the Pechini procedure the gel, obtained after addition of PEG (20% w/w) to the starting solution, was dried at 120 °C for 12 h and then thermally treated as in the previous case. Table 3.1 reports the list of the synthesized samples and the acronyms used along the chapter.

Tab. 3.1. List of the synthesized samples and identifying acronyms.

Phosphor	Synthetic technique	Acronym
$Y_{0.99}\,Dy_{0.01}\,(P_{0.8}V_{0.2})O_4$	Sol-Gel	SGD_1
$Y_{0.99}\,Dy_{0.01}\,(P_{0.8}V_{0.2})O_4$	Hydrothermal method	HTD_1
$Y_{0.99}\,Dy_{0.01}PO_4$	Solid state reaction	SS_1D_1
$Y_{0.99}\,Dy_{0.01}\,(P_{0.8}V_{0.2})O_4$	Solid state reaction	SS_2D_1
$Y_{0.99}\,Dy_{0.01}\,(P_{0.5}V_{0.5})O_4$	Solid state reaction	SS_3D_1
$Y_{0.99}\,Dy_{0.01}\,(P_{0.2}V_{0.8})O_4$	Solid state reaction	SS_4D_1
$Y_{0.99}\,Dy_{0.01}VO_4$	Solid state reaction	SS_5D_1

Characterization

The samples were structurally characterized by powder XRD and their morphology was examined by means of a SEM (see chapter 2 for experimental details). The room temperature emission and excitation spectra were measured using a Fluoromax-3 (Jobin-Yvon) spectrofluorimeter. The decay profiles were measured at 300 K upon 355 nm laser excitation using a pulsed Nd:YAG laser (Quanta System model SYL 202); the emission was isolated by means of a Hilger–Watts Model D330 double monochromator and detected with a Hamamatsu R943-022 photomultiplier connected to a LeCroy 9410 transient digitizer.

3.3 Results and discussion

Solid state synthesis and host effects on the luminescence properties

The samples obtained by solid state reaction were used to investigate the crystallographic and emission properties as a function of the host composition. Their powder X-Ray diffraction (PXRD) patterns, reported in Fig. 3.1a, are characterized by a progressive shift of the peaks towards lower 2θ values with increasing vanadium concentration.

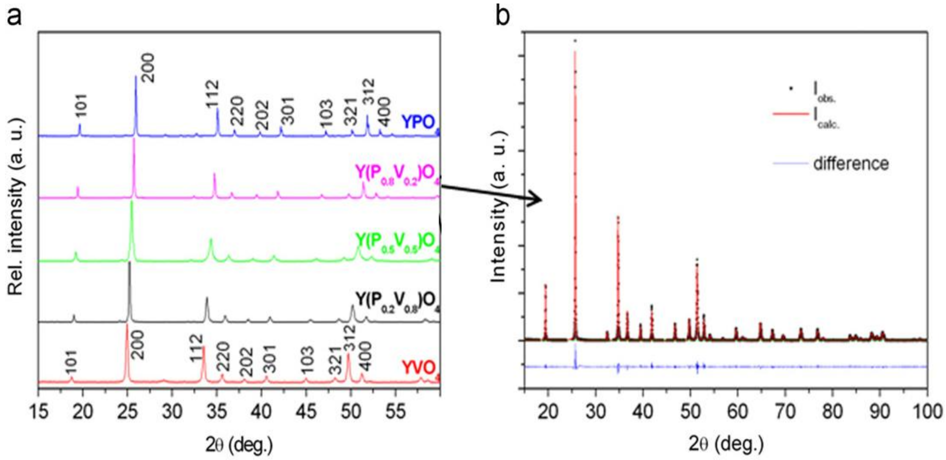

Fig. 3.1. (a) PXRD patterns along the $Y_{0.99}Dy_{0.01}(P_{1-x}V_x)O_4$ system synthesized by solid state reaction. (b) Rietveld plot.

A close inspection of the patterns has revealed that the occasional presence of extra phases, mostly unreacted V_2O_5, does not exceed 1% of the total amount. A refinement by the Rietveld method was been carried out using the GSAS package [2,3] in the $I4_1/amd$ space group (zircon-type structure). The agreement between measured and calculated intensities was good, (see the Rietveld plot of Fig. 3.1b as an example). The most relevant parameters resulting from the refinements are collected in Table 3.2.

Table 3.2. Rietveld refinement of the XRD patterns of Fig. 3.1.

Sample	**Lattice parameters**			**Refined P occupancy**	**Atomic coordinates**		**Isotropic thermal parameters (Å^2)**			**R (F^2)**	χ^2
	a=b (Å)	*c* (Å)	V (Å^3)		O y	O z	Y	P/V	O		
SS_1D_1	6.885 (1)	6.022 (1)	285.45 (2)	0.99(1)	0.075 (1)	0.213 (1)	0.006 (1)	0.008 (1)	0.003 (1)	5.35	1.95
SS_2D_1	6.929 (1)	6.073 (1)	291.66 (2)	0.84(2)	0.075 (1)	0.213 (1)	0.009 (1)	0.006 (2)	0.006 (2)	3.31	5.83
SS_3D_1	6.987 (1)	6.138 (1)	299.63 (2)	0.58(1)	0.078 (1)	0.208 (1)	0.004 (1)	0.004 (1)	0.007 (1)	5.86	7.25
SS_4D_1	7.072 (1)	6.239 (1)	311.98 (1)	0.26(1)	0.071 (3)	0.206 (1)	0.011 (1)	0.004 (1)	0.006 (1)	5.06	5.94
SS_5D_1	7.119 (1)	6.292 (1)	318.92 (1)	0.01(1)	0.434 (1)	0.202 (1)	0.005 (1)	0.007 (1)	0.007 (1)	5.53	0.65

They are consistent with those previously published [4, 5]. The evaluated mean bond lengths are reported in Table 3.3. As expected, the yttrium–oxygen distances slightly increase (no more than 1% in total), while the average phosphor/vanadium–oxygen distances progressively increase (up to about 10%) with the vanadium concentration, consistently with the individual bond lengths reported for the tetrahedrally coordinated P^{5+} and V^{5+} cations (1.52 and 1.70 Å respectively, [6]).

Table 3.3. Relevant bond distances.

Sample	**Y-O avg. distance**	**P-O avg. distance**
SS_1D_1	2.346(1)	1.551(1)
SS_2D_1	2.358(1)	1.562(1)
SS_3D_1	2.365(1)	1.583(1)
SS_4D_1	2.371(1)	1.648(1)
SS_5D_1	2.369(1)	1.704(1)

The SEM image of the SS_2D_1 phosphor, Fig. 3.2, reveals that it is composed of micrometric grains having roundish contours, as a consequence of the partial sintering process taking place during the solid state reaction occurring at relatively high temperature (1200 °C).

The visible emission spectra of the Dy^{3+} ion in oxide lattices are composed of two main bands in the blue (480 nm) and yellow (575 nm) region and of a weaker feature in the red, assigned to the transition from the $^4F_{9/2}$ level to $^6H_{15/2}$, $^6H_{13/2}$, and $^6H_{11/2}$, respectively. Bao et al. [1] have observed that the relative intensity of the yellow and blue bands (expressed as Y/B ratio) depends on the host composition and is in great part responsible for the color of the emitted radiation. We have discussed this aspect by considering the results of the Judd–Ofelt (J–O) theory [7, 8] applied to the analysis of the absorption spectra of Dy^{3+} in YVO_4 and YPO_4 single crystals [9,10]. In this connection, Faoro et al. [10] pointed out that the vanadate host is characterized by much larger values of the Ω_2 and Ω_4 intensity parameters with respect to the phosphate lattice: this implies a higher value of the spontaneous emission coefficient of the $^4F_{9/2}$ emission, a shorter lifetime and a larger ratio between the spontaneous emission probabilities associated to the yellow and to the blue emission. In analogy with the $Eu^{3+}:Y(P,V)O_4$ case

[11], we expect that these properties progressively vary with the composition along the $Y_{0.99}Dy_{0.01}(P_xV_{1-x})O_4$ isomorphic series.

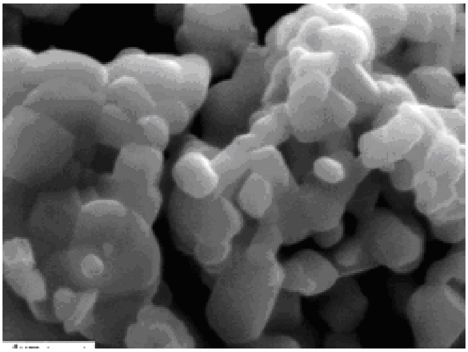

Fig. 3.2. SEM image of the SS_2D_1 sample.

In Fig. 3.3 we compare the emission spectra of the SS_nD_1 (n=1–5) samples measured upon 390 nm excitation, in correspondence of the most intense Dy^{3+} absorption transition.

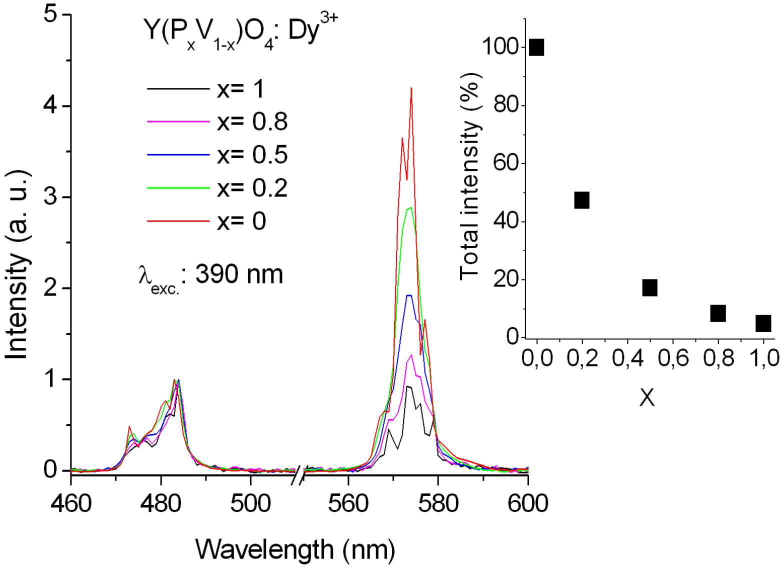

Fig. 3.3. Emission spectra of the SS_nD_1 samples.

They have been normalized with respect to the maximum of the blue emission band. As expected, the Y/B intensity ratio and the total emission intensity increase with the vanadium content. The decay curves of the Dy^{3+} emission are shown in Fig. 3.4: they are nearly single exponential for $x \leq 0.2$ and non exponential for $x > 0.2$. Different factors can affect the emission decay profiles, like the presence of lattice defects, of non-equivalent emitting centers [11] as well as energy transfer processes, certainly active at the adopted doping level. The average decay times have been estimated by means of the formula [12]:

$$\tau = \frac{\int t\, I(t)dt}{\int I(t)dt} \qquad (3.1)$$

where *I(t)* represents the luminescence intensity at time *t*. They are listed in Table 4, together with the radiative lifetimes of the $^4F_{9/2}$ level in the pure phosphate and vanadate hosts.

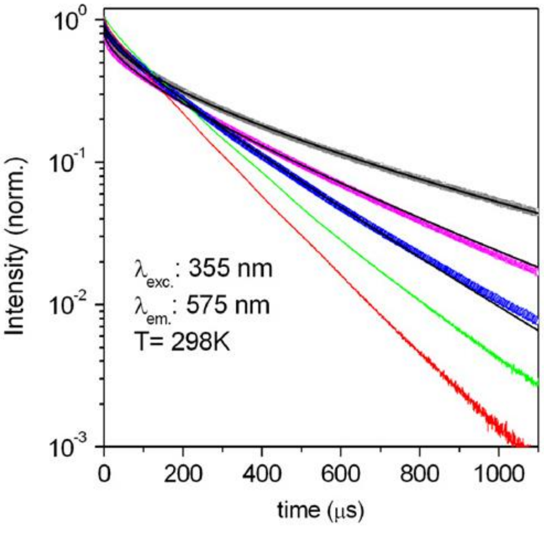

Fig. 3.4. Decay profiles of the emission of the SS_nD_1 samples.

In the same table the experimental values of the Y/B ratio, obtained from the integrated areas of the corresponding emission bands, are compared with the theoretical values calculated from the ratios of the appropriate spontaneous emission coefficients averaged over the host compositions. It is evident that the experimental data follows only qualitatively the trend individuated by the J–O approach, and that there is a significant discrepancy between the expected and the observed values. The intrinsic uncertainty of the model (of the order of ± 30%), the possibility of calibration errors, the presence of defect centers and the non-radiative processes can only in part account for this discrepancy. On the other hand, it is well known that there are aspect of the spectroscopy of the Dy^{3+}-doped compounds that are not yet fully understood [13] and we do not exclude that further work in this direction could imply a revision of the J–O analysis applied to these materials.

Table 3.4. Radiative lifetimes and experimental decay times of the $^4F_{9/2}$ state, calculated and experimental Y/B ratios along the$Y_{0.99}Dy_{0.01}(P_xV_{1-x})O_4$ series.

x	**$\tau(\mu s)_{calc.}$**	**$\tau(\mu s)_{exp.}$**	**$Y/B_{calc.}$**	**$Y/B_{excp.}$**
1	1279	485	1.36	0.76
0.8	-	315	1.91	1.06
0.5	-	232	2.74	1.45
0.2	-	182	3.57	1.89
0	440	150	4.12	2.28

The average decay times evaluated using Eq. (1) take into account the effects of different optical centers and have the advantage of being comparable, then suitable for the previous considerations. However, a more accurate examination of the non exponential curves of Fig. 3.4 reveal that they have the profiles typically observed in the case of Dy^{3+}–Dy^{3+} energy transfer processes [13,14] associated to resonant or nearly resonant cross relaxation mechanisms such as:

${}^4F_{9/2} + {}^6H_{15/2} \rightarrow {}^6H_{5/2} + {}^6F_{7/2}$

${}^4F_{9/2} + {}^6H_{15/2} \rightarrow ({}^6F_{3/2}, {}^6F_{1/2}) + ({}^6H_{9/2}, {}^6F_{11/2})$

schematized in Fig. 3.5. We have analyzed these decay curves by means of the Inokuti–Hirayama model. The best fit of the decay curves has been carried out using Eq. (1.16) by considering a *D–D* process and A, τ and α as adjustable parameters. The values of τ deduced from the fit procedures of the critical distances calculated by means of eq. (1.17) are reported in table 3.5, together with the average distances between the Dy^{3+} ions calculated using the data reported in Table 3.3. These results raise interesting considerations.

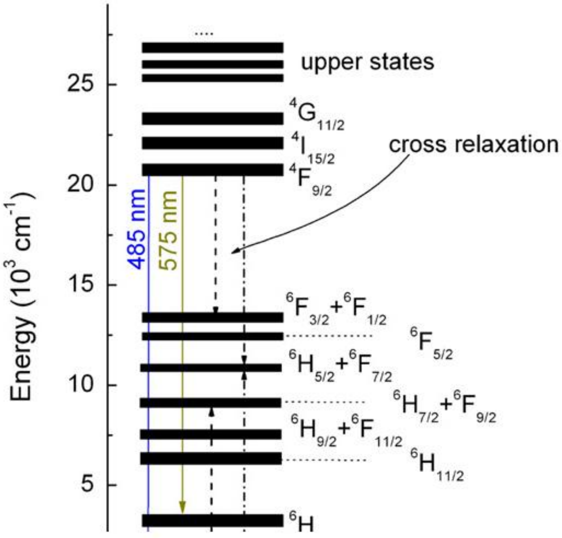

Fig. 3.5. Energy levels scheme of the Dy^{3+} ion with the most important emission transitions and cross relaxation pathways.

First of all, the lifetimes of the isolated donors are significantly longer than the average decay times calculated by means of Eq. (3.1): in the case of the pure phosphate the obtained value is very close, compatibly with the approximations involved, to that calculated by means of the J–O approach. This is not sufficient to account for the discrepancies between experimental and theoretical results, but it provides good indications in this direction.

Table 3.5. Lifetimes and critical distances for the Dy^{3+}-Dy^{3+} energy transfer process in$Y_{0.99}Dy_{0.01}(P_xV_{1-x})O_4$ obtained from the Inokuti–Hirayama fit of the decay curves of Fig. 3.4.

x	**τ_{rad}(μs)**	**$d_{crit.}$(Å)**	**d_{av}(Å).**
1	1346	13.4	11.9
0.8	589	11.2	12
0.5	306	9.1	12.1

Second, the critical distance for the energy transfer is of the same order of magnitude of the average distance between the doping ions when the radiative lifetime is long, i.e. for x=1 and 0.8, and significantly decreases for x=0.5. When the vanadium content exceeds that of phosphor in the host composition, the decay profile become exponential. We conclude that the probability of the Dy^{3+}–Dy^{3+} energy transfer process increases with the intrinsic lifetime of the donor, namely with the P/V ratio. Excitation in the UV region is attractive in the perspective of applications in the phosphor technology. The excitation spectrum shown in Fig. 3.6 is constituted of a strong absorption edge starting at about 330 nm and extending in the UV, ascribed to the charge transfer transition of the vanadate units. The absorption features of Dy^{3+} are much weaker and located at 352 ($^4M_{5/2}+^6P_{7/2}\leftarrow^6H_{15/2}$), 366 ($^4P_{3/2}+^6P_{3/2}\leftarrow^6H_{15/2}$) and 390 nm ($^4I_{13/2}+^4K_{17/2}\leftarrow ^6H_{15/2}$). The relative intensity of the host band allows to infer that the energy transfer from the VO_4^{3-} group to the Dy^{3+} ion is rather efficient. Obviously this process does not take place in the pure phosphate lattice. In the emission spectra measured upon 280 nm excitation, shown in Fig. 3.6, the expected trends of both Y/B ratio and overall Dy^{3+} luminescence intensity are confirmed. In addition, the spectra present the characteristic broadband vanadate emission in the blue region, with maximum at 440 nm.

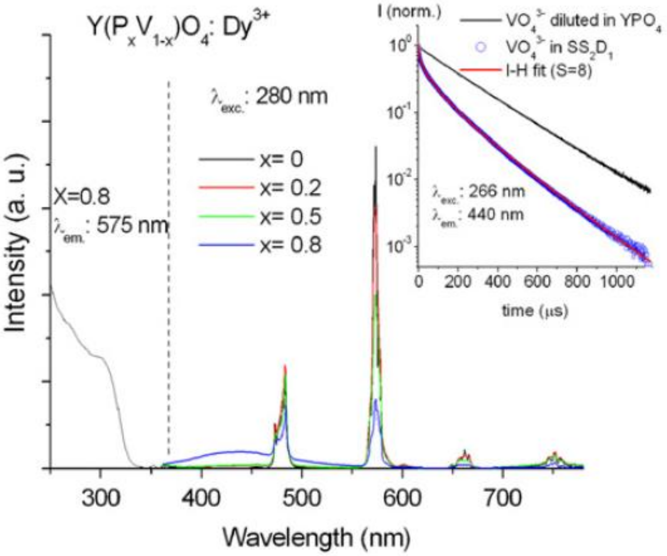

Fig. 3.6. Excitation (representative example) and UV excited emission spectra of the SS_nD_1 samples. Inset: VO_4^{3-} decay profiles.

This band, intense in the spectrum of SS_2D_1 ($(Y_{0.99}Dy_{0.01}(P_{0.8}V_{0.2})O_4$ composition) and rather weak in the other cases, influences the color of the emitted radiation, as evidenced in the chromaticity diagram shown in Fig. 3.7. When this latter emission is weak in fact, the luminescence of the material is yellowish and its representative point moves towards the pure yellow color as the vanadium content of the host, and consequently the Y/B ratio increases. When strong, it introduces an additional blue component that completely alters the color characteristics giving rise to a bluish luminescence. The presence of this band with proper intensity is necessary in order to realize a white emitting phosphor. In summary, the color of the luminescence of this material result from different concomitant processes: the matrix effect on the Y/B intensity ratio, already discussed, the concentration quenching of the vanadate emission and the VO_4^{3-}-Dy^{3+} energy transfer.

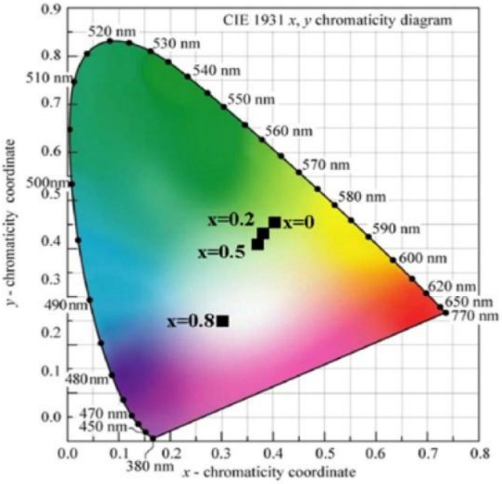

Fig. 3.7. Chromaticity coordinates evaluated from the emission spectra.

The quenching of the vanadate luminescence is a known phenomenon [15] associated to the migration of the excitation favoring non radiative processes. On the other hand, the mechanism at the origin of the host sensitization of the Dy^{3+} ions has not yet been characterized in details, to the best of our knowledge. In order to investigate this aspect we have measured the decay profile of the vanadate emission of the SS_2D_1 sample upon 266 nm pulsed laser excitation (see inset of Fig. 3.6). We have reproduced the vanadate decay curve using the Inokuti–Hirayama model (Eq. (1.16)) and considering a *D*-*Q* process. The τ value obtained from the fit is 259 µs (see inset of Fig. 3.6). The critical distance for the transfer, calculated by means of Eq. (1.17), is 12 Å. In order to test the applicability of the Hinokuti–Hirayama model in the present case we have measured the decay profile of VO_4^{3-} very diluted (less than 0.5%) into a YPO_4 single crystal grown from $Pb_2P_2O_7$ flux. The curve, shown in the inset of Fig. 3.6, is a single exponential with a decay constant of 222 µs, in good agreement with the radiative lifetime provided by the analysis, especially in consideration of the theoretical approximations and of the unavoidable experimental uncertainties. As a last consideration, we point out that the solid state route allows a good control of the stoichiometry and then it is suitable to analyze the relations between structure, composition and spectroscopic properties. On the other hand, it requires high temperature processing that results in a partial sintering of the phosphor grains, whose size and morphology are difficult to control [16]. For this reason we have extended the investigation to other synthetic methodologies.

Sol–gel synthesis and emission performance

The XRD pattern of the powder resulting from the synthesis described in section 2 and the SEM image are reported in Fig. 3.8. The formation of a single phase system is confirmed as well as the host composition, the broadness of the diffraction peaks indicates that the average size of the grains is smaller than that of the SS_nD_1 samples. The SEM image is consistent with this observation and reveals that most of the grains are well crystallized with the rod-like shape often observed in the case of the macroscopic yttrium phosphate and vanadate crystals grown by spontaneous nucleation from molten salts solutions [17].

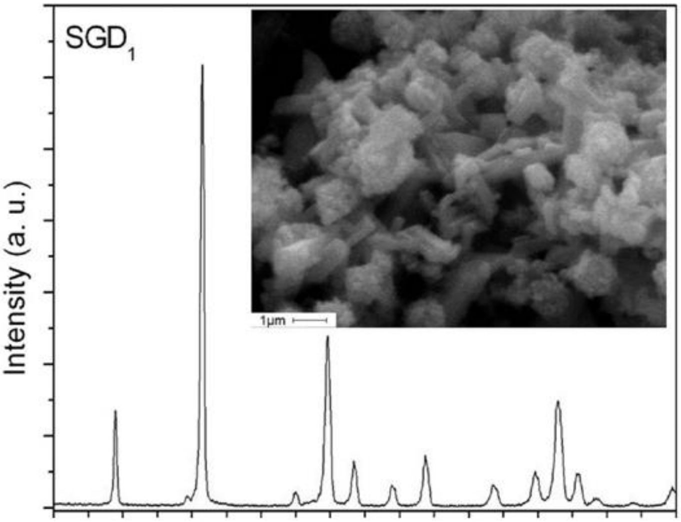

Fig. 3.8. PXRD pattern and SEM image of the SGD$_1$ phosphor.

The morphology of the particles influences the emission properties: for instance, nano-sized grains allow to realize very homogeneous coatings with high pixel resolution. On the other hand however, the luminescence of a phosphor (in terms of brightness, intensity, etc.) can be affected by phenomena occurring at grain surface like adsorption of impurities, structural distortions, alterations of the coordination geometries around the active ions, of the electron phonon coupling and of the refractive index [18]. As a consequence, the emission mechanisms in proximity of the grain surface can be different than in the bulk. Concerning the energy transfer processes, the situation is even more complicate: other than the abovementioned effects, boundary effects can modify the excitation profiles of the donor [19] and quantum confinement effects could limit the migration of the energy inside the particles [20]. For these reasons the rationalization of the relationships between the morphology and the luminescence properties is a difficult task and consequently the optimization of the performances requires the application of different experimental techniques depending on the synthetic approach and on the application perspectives of the material. This lies beyond the scope of the present work. Nevertheless, since Bao et al. [1] have pointed out the device potentiality of the phosphor prepared by the sol–gel route, we have decided to compare the emission spectrum of the SGD_1 sample with those of a red and a blue commercial phosphors, measured in similar experimental conditions. The result, shown in Fig. 3.9, is encouraging, since the three spectral intensities are of the same order of magnitude.

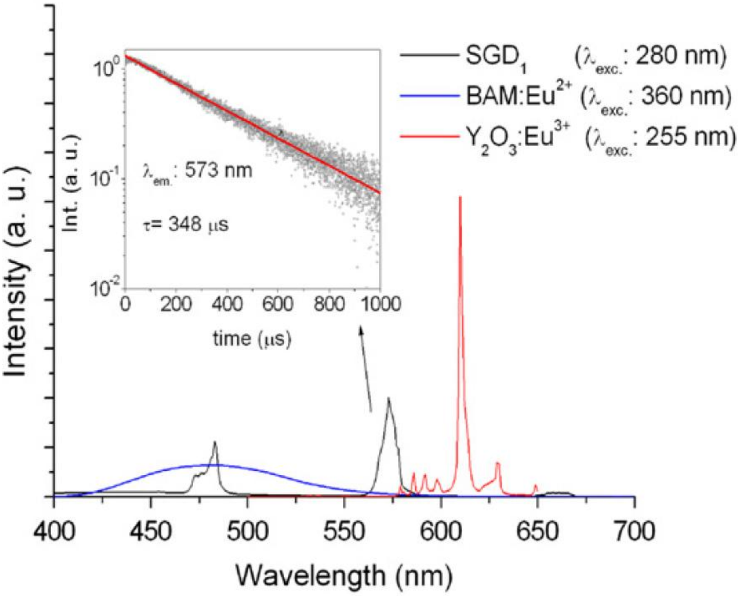

Fig. 3.9. Comparison between the emission spectra of SGD_1 and those of the $BAM:Eu^{2+}$ and $Y_2O_3:Eu^{3+}$ commercial phosphors. Inset: decay profile of the Dy^{3+} emission in SGD_1.

It is interesting to compare the emission properties of SGD_1 and SS_nD_1 (Fig. 3.12): the Y/B ratios are similar, the decay time of the Dy^{3+} emission are 348 and 315 μs, respectively, and the total emitted intensity is slightly larger whereas the relative intensity of the vanadate emission is moderately lower in the former case. We suppose that the reason of this behavior could be connected to the different morphologies of the two phosphors: it is conceivable that the better crystallinity and the smaller size of the SGD_1 grains can give rise to a brighter luminescence and to a limited migration of the Dy^{3+} excitation towards killer centers.

Consequently, the global intensity of the emitted radiation is higher and its color white, as shown in Fig. 3.10, as an effect of the reduced contribution of the blue component.

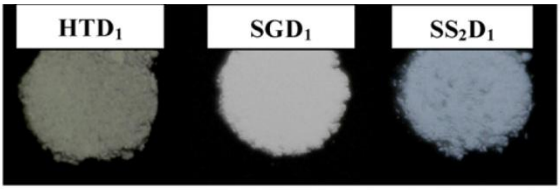

Fig. 3.10. Emissions of the $Y_{0.99}Dy_{0.01}(P_{0.8}V_{0.2})O_4$ phosphors upon 254 nm lamp excitation.

Hydrothermal synthesis and comparative evaluation

We have investigated for the first time, to the best of our knowledge, the possibility of applying the hydrothermal method to the synthesis of the $Y_{0.99}Dy_{0.01}(P_{0.8}V_{0.2})O_4$ mixed system. In the frame of the procedure described in section 2, we have monitored the XRD patterns and the emission properties along the various steps of the thermal treatment. The results are shown in Fig. 3.11. It is evident that the target compound is formed after the low temperature/long time treatment; on the other hand, the broadness of the diffraction peaks indicates a rather small grain size, namely a low crystallinity degree.

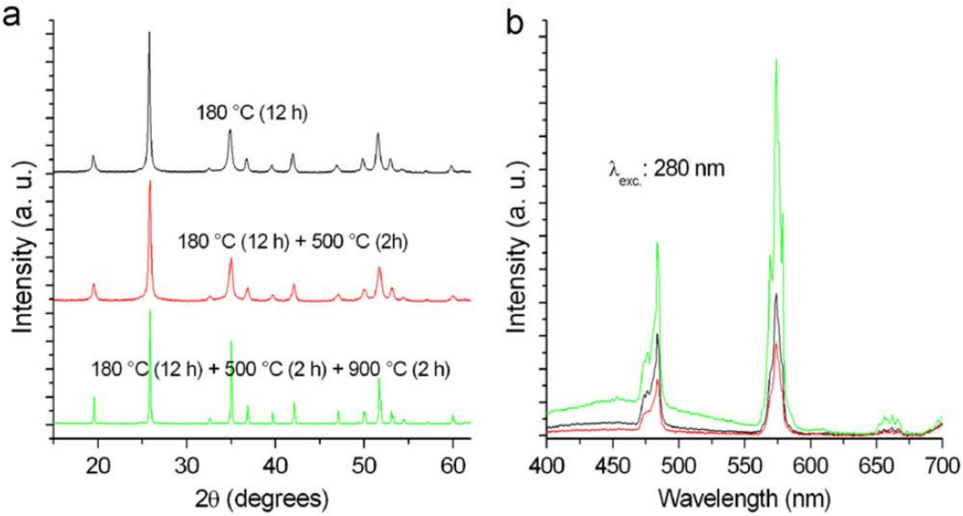

Fig. 3.11. PXRD patterns (a) and emission spectra (b) of the HTD_1 phosphor after the different steps of the thermal treatment.

The intensity of the emission spectrum is low. These properties do not substantially change after the second treatment at 500 °C, whose main purpose is completing the elimination of water and organic residuals. After the annealing at 900 °C the diffraction features become narrower and the luminescence intensity considerably increases. However, compared with the one shown by the previously examined phosphors (see Fig. 3.12) it remains rather weak. The color of the emitted radiation is more grayish than white, as already shown in Fig. 3.10. We ascribe this behavior to the low quality of the particle morphology: the SEM image of the HTD_1 sample (inset of Fig. 3.12) in fact reveals the formation of agglomerates of shapeless grains having different sizes.

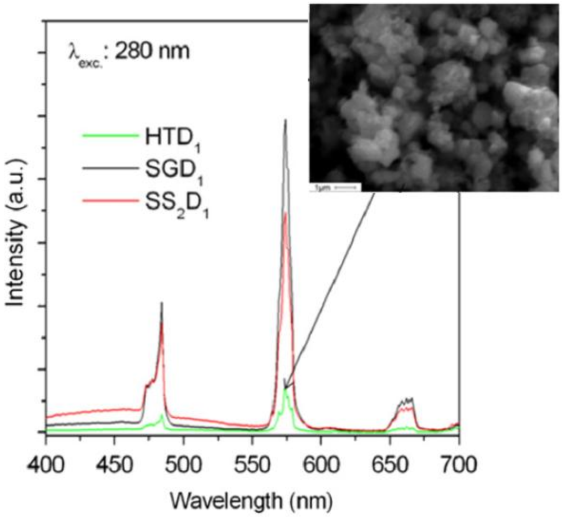

Fig. 3.12. Comparison between the emission spectra of the $Y_{0.99}Dy_{0.01}(P_{0.8}V_{0.2})O_4$ phosphors obtained by the different synthesis methodologies. Inset: SEM image of the HTD_1 phosphor.

The investigated hydrothermal route has provided an inferior quality phosphor with respect to the solid state and the sol–gel synthesis procedures. Further experiments will be necessary in order to verify the actual reliability of this technique and its perspectives of improvement.

3.4 Concluding remarks

In the frame of a comparative study concerning three different methods for the synthesis of the $Y_{0.99}Dy_{0.01}(P_{0.8}V_{0.2})O_4$ phosphor we have explored the relations between host composition, structural and morphological characteristics and emission dynamics. The luminescence properties of this system are the result of the combination of different interacting factors, whose full control is not an easy task. We have demonstrated that not only the intensity ratio between the yellow and blue emission bands of Dy^{3+} depend on the host composition, but also the lifetime of the fluorescent level as well as the efficiency of the energy transfer between the rare earth ions. These effects can be formalized in the framework of the Judd–Ofelt approach, starting from the consideration that the values of the Ω_2 and Ω_4 intensity parameters of the pure phosphate and vanadate lattices are very different. These are related to short range (covalent) effects and long range bulk properties of the local field, and their variation induced by the progressive substitution of phosphor by vanadium (or vice versa) implies the concomitant variation of the polarizability of the oxygen anions and of the local distortion around the optical centers, and then of the oscillator strengths of the radiative transitions. Considering the involved approximations, it is not surprising that the agreement between theory and experiments is more qualitative than quantitative, even if there are reasons to believe that there is room for the improvement of the model. The white luminescence obtained upon UV excitation is the result of the balanced contributions of the host and Dy^{3+} emissions. We have considered the factors affecting the relative intensities, pointing out the key role of the $VO_4^{3-} \rightarrow Dy^{3+}$ energy transfer process, whose mechanism has been characterized. Finally, the tests concerning the three different synthesis methodologies allow to conclude that the adopted solid state, sol–gel and hydrothermal procedures yield the desired phase and composition with good purity. On the other hand, the morphologies of the resulting materials are rather different, and their impact on the luminescence performances is significant: the emissions of the phosphors obtained 'via' sol–gel and solid state reaction have similar intensities but slightly different colors, whereas the phosphor obtained by the hydrothermal route emits rather weakly. The possible reasons of these behaviors have been proposed and briefly discussed.

References

[1] A. Bao, H. Yang, C. Tao, Y. Zhang, L. Han, J. Lumin. 128 (2008) 60.

[2] A.C. Larson, R.B. Von Dreele, General Structure Analysis System (GSAS), Los Alamos National Laboratory Report LAUR 86-748, 2000.

[3] H.B. Toby, J. Appl. Cryst. 34 (2001) 210

[4] W.O. Milligan, D. Mullica, G.W. Beall, L.A. Boatner, Inorg. Chim. Acta 60 (1982) 39.

[5] B.C. Chakoumakos, M. Abraham, L.A. Boatner, J. Solid State Chem. 109(1994) 197.

[6] R.D. Shannon, C.T. Prewitt, Acta Cryst. B 25 (1969) 925.

[7] B.R. Judd, Phys. Rev. 127 (1962) 750.

[8] G.S. Ofelt, J. Chem. Phys. 37 (1962) 511.

[9] E. Cavalli, M. Bettinelli, A. Belletti, A. Speghini, J. Alloys Compd. 341 (2002) 107.

[10] R. Faoro, F. Moglia, M. Tonelli, N. Magnani, E. Cavalli, J. Phys. Condens. Matter 21 (2009) 275501.

[11] G. Pan, H. Song, Q. Dai, R. Qin, X. Bai, B. Dong, L. Fan, F. Wang, J. Appl. Phys. 104 (2008) 084910.

[12] S. Shionoya, W.M. Yen, Phosphor Handbook, CRC Press, Boca Raton,FL, 1999.

[13] S. Bigotta, M. Tonelli, E. Cavalli, A. Belletti, J. Lumin. 130 (2010) 13

[14] E. Cavalli, E. Bovero, A. Belletti, J. Phys. Condens. Matter 14 (2002) 5221.

[15] H. Ronde, G. Blasse, J. Inorg. Nucl. Chem. 40 (1978) 215

[16] S. Ye, F. Xiao, Y.X. Pan, Y.Y. Ma, Q.Y. Zhang, Mater. Sci. Eng. R 71 (2010) 1.

[17] G. Garton, S.H. Smith, B.M. Wanklyn, J. Cryst. Growth 13/14 (1972) 588.

[18] B.M. Tissue, J. Lumin. 131 (2011) 362.

[19] W. Xu, Y. Wang, X. Bai, B. Dong, Q. Liu, J. Chen, H. Song, J. Phys. Chem. C 114 (2010) 14018.

[20] A. Huignard, V. Buissette, A.-C. Franville, T. Gacoin, J.-P. Boilot, J.Phys. Chem. 107 (2003) 6754.

Chapter 4

Optical spectroscopy and excited state dynamics of $CaMoO_4$:Pr^{3+}

4.1 Introduction

Mixed oxides activated with Pr^{3+} are extensively investigated as materials for photonics [1,2]. Their application perspectives depend on the efficiency of the emission channels and of the excitation modalities. In many closed shell transition metal oxides, Pr^{3+} ions can be excited either directly in the blue ($^3H_4 \rightarrow {}^3P_{0,1,2}$, $^1I_6$ intraconfigurational transitions) or in the UV (interconfigurational $4f^2 \rightarrow 4f^1 5d^1$ transitions), or indirectly through UV host excitation followed by an energy transfer and/ or an intervalence charge transfer (IVCT) process. The fluorescence dynamics of these systems depend not only on the structure of the energy levels of the rare earth ion but also on their relative position with respect to the host fundamental bands [3,4]. The analysis of the optical spectra measured as a function of the temperature and of the excitation wavelength provides an important information in this connection. In this work we investigate the spectral properties of $CaMoO_4$:Pr^{3+}. This material was studied long time ago by Reut and Ryskin in the ambit of a systematic on the ‘virtual recharge’ (i.e. IVCT) mechanism [5] and was investigated more recently by Zhu et al. [6,7] for white light generation. The emission mechanism proposed by Reut and Ryskin implied the formation of Pr^{4+} as a transient species, while Zhu et al. have discussed their experimental results by asserting that the dopant was stably present in the two valence states +3 and +4, without considering the possibility of charge transfer processes. These different points of view evidence that the excited states dynamics of this system has not been sufficiently clarified yet. Their study, on the other hand, has practical motivations. $CaMoO_4$ belongs to the family of the scheelite structured tungstates and molybdates with general formula MXO_4 (M=Ca, Sr, Ba; X= W, Mo), that can be conveniently activated with rare earth ions in order to develop active media for solid state lasers [1], Raman lasers in particular [8], and phosphors technologies [9,10]. In this context the characterization of Pr^{3+}-doped $CaMoO_4$ is important in order to extend the available information and the device potentialities of this class of materials.

4.2 Experimental details

Synthesis

$CaMoO_4$ pure (CMO) and doped with Pr^{3+} (Pr:CMO) was synthesized in form of single crystals and powders by different methods. Undoped, 0.1% and 0.5% (Pr/Ca nominal ratio) single crystals, denoted as C00, C01 and C05 respectively, were grown by means of a 'flux growth' method developed in our laboratory. The starting composition (in wt%) was: CaO 7%, Na_2CO_3 18%, MoO_3 75%, Pr_6O_{11} (in suitable amount). The mixture was put in a platinum crucible and slowly heated to 1350 °C in a horizontal furnace. After an appropriate soaking time (10–12 h) the temperature was lowered to 600 °C at a rate of 4–5 °C h^{-1}. Transparent crystals up to 3×2×1 mm^3 were separated from the flux using hot diluted HCl [11]. Powders of Pr:CMO (0.75% concentration) with different grain sizes were synthesized by solid state reaction (SS07 sample) and Pechini sol–gel (SG07 sample) procedures. In the former case, stoichiometric amounts of MoO_3 (Aldrich, 99.5%), $CaCO_3$ (Carlo Erba,99.5%) and Pr_6O_{11} (Aldrich, 99.9%) were thoroughly mixed in alumina crucible and fired following the sequence 550 °C (12h), 650 °C (2h), 750 °C (2h) and finally at 900 °C (2h). In the sol–gel route, appropriate amounts of $CaCO_3$ and Pr_6O_{11} were dissolved in HNO_3 3M at 75 °C under vigorous stirring. Citric acid with a 2:1 M ratio with respect to the metal ions was then added as a chelating agent. A stoichiometric amount of $(NH_4)_6Mo_7O_{24}$ (Carlo Erba, 99.5%) was dissolved in hot water and then added to the cationic solution together with PEG (20%w/w) as a gelling agent. The resulting solution was dried at 80 °C for 4h and then at 120 °C for 12h. The phosphor was finally obtained after successive calcinations at 500 °C for 2h and 900 °C for 2h. The samples were characterized by XRD and SEM techniques as described is Sect. 2.

Spectroscopic measurements

The luminescence properties have been measured in different excitation and temperature conditions. The experiments on the powder samples have been carried out at room temperature only by means of a Fluoromax 3 (Jobin-Yvon) spectrofluorimeter. The 10 K emission spectra of the crystals were measured with a spectroscopic system equipped with a 450W xenon lamp fitted with a 0.25 m Spex monochromator as source, and a 1.26 m Spex monochromator with a RCA C31034 photomultiplier to analyse and detect the output radiation. The crystals were mounted onto the cold finger of a He-cryocooler (Air Products Displex DE-202). The 300–600 K spectra were measured using a Triax 550 monochromator equipped with a nitrogen-cooled CCD camera and a R928 Hamamatsu photomultiplier (Jobin-Yvon Symphony system). The excitation light was selected from a xenon lamp using a Triax 180 monochromator. The crystals were mounted on a homemade copper holder heated by a thermocoax wire connected to a Thermolyne regulator. The temporal decay profiles were measured at room temperature upon dye (480 nm), nitrogen (337 nm) or Nd:YAG (266 nm) laser excitation and displayed by means of a 400 MHz Lecroy digital oscilloscope with 50 Ω input impedance.

4.3 Results

Structural considerations, host luminescence and impurity effects

$CaMoO_4$ is tetragonal (space group $I4_1/a$), with $a=b=5.226$ Å and $c=11.430$ Å, $Z=4$ [12]. In this scheelite-type structure (Fig. 4.1) the isolated MoO_4^{2-} distorted tetrahedral (S_4 real point symmetry) share their vertices with the CaO_8^{14-} dodecahedral units (distorted, S_4 real point symmetry), which are connected one to another through the edges to form zig-zag chains developing along the crystallographic *c* axis.

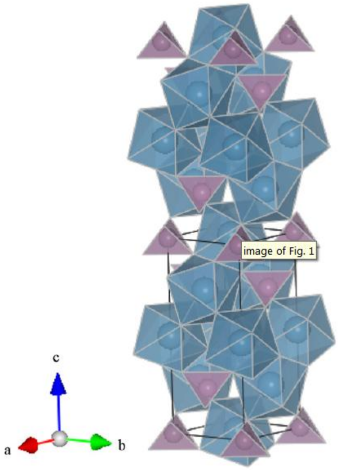

Fig. 4.1. $CaMoO_4$ structure (elaborated using the VESTA software [13]).

Pr^{3+} replaces Ca^{2+}, and this substitution requires charge compensation. It is probably achieved in the crystals by the accommodation of Na^{+} ions (present in the flux) at the Ca^{2+} sites and by formation of cationic vacancies in the case of the powders. Whatever the case, the charge compensation results in the perturbation of the local crystal fields acting on the optically active ions. This results in a marked inhomogeneous broadening of their absorption and emission features, even at low temperature. The structure, the phase purity and the morphology of the SS07 and SG07 samples were analyzed using XRD and SEM techniques (Fig. 4.2).

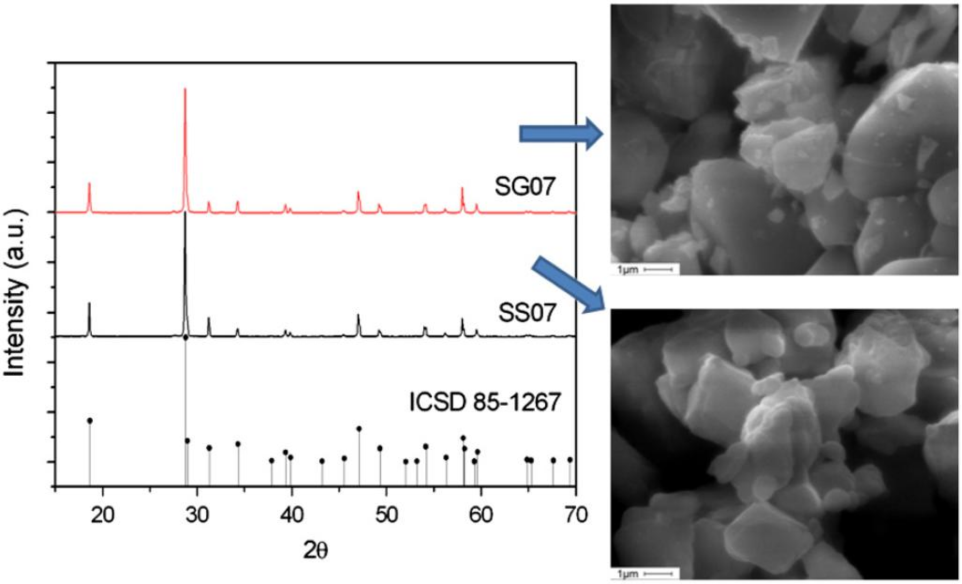

Fig. 4.2. XRD patterns and SEM images of the SS07 and SG07 samples.

The XRD pattern evidence the formation of the desired compounds and the absence of unwanted phases. The SEM image reveals that the SS07 sample has a more uniform morphology and larger average particle size than the

SG07 one, whose grains have rather irregular shape and size distribution, with the presence of nanometric particles.

The room temperature excitation and emission spectra of pure CMO (C00 sample) were measured at different emission/excitation wavelengths. They are shown in Fig. 4.3.

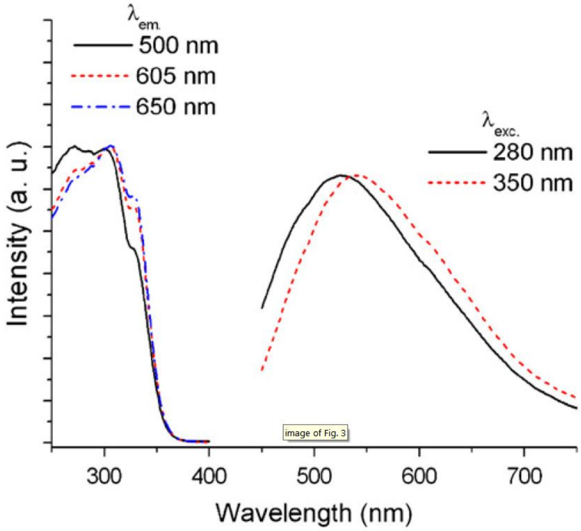

Fig. 4.3. Room temperature excitation and emission spectra of pure $CaMoO_4$ crystals. The band intensities have been normalized.

The emission band with maximum at 520 nm is assigned to the spin forbidden $^3T_{1,2}\rightarrow{}^1A_1$ transition. The corresponding excitation system is ascribed to the spin allowed $^1T_2\leftarrow{}^1A_1$ charge transfer transition of the regular $MoO_4{}^{2-}$ unit [14]. The fact that these units are well separated from each other allows inferring that the energy migration is not a favored process in this system, consistently with the relatively large Stokes shift (about 14000 cm^{-1}) between the excitation and emission maxima. The excitation at around 350 nm reveals an orange component ascribed to charge compensating defects (likely MoO_3) subsequent to the accommodation of aliovalent impurities like Na^+, present in excess in the growth batch [15]. The shoulder occurring at 320 nm in the excitation spectrum has the same origin. The electronic structure and the spectral properties of CMO still constitute an open research topic [16, 17] that is beyond the purpose of the present work. It is however clear that the Pr^{3+} incorporation increases the amount of perturbed centers. In addition, it is known that Pr^{3+} can interact with the host giving rise to a photoinduced redox process of the type:

$$\mathrm{Pr}^{3+} + \mathrm{Mo}^{6+} \rightarrow \mathrm{Pr}^{4+} + \mathrm{Mo}^{5+}$$

resulting in the formation of the IVCT state. This metal-to-metal charge transfer state can interfere with the fluorescence dynamics of the Pr^{3+} ions, giving rise to various interesting effects [18-20]. The analysis of the IVCT mechanism not only accounts for the experimental observations, but also allows compiling a ‘host lattice plus rare earth ion’ energy level scheme that can be extended to the whole lanthanide series [4,21]. In the case of CMO this scheme is already available [22] and will be conveniently applied in the present study. As reported in literature [18], the position of the IVCT state is related to the host properties by the empirical equation:

$$\mathrm{IVCT}\,(\mathrm{Pr}^{3+}, \mathrm{cm}^{-1}) = 58800 - 49800\,\frac{\chi_{\mathrm{opt}}(M^{n+})}{d(\mathrm{Pr}^{3+} - M^{n+})} \qquad 1$$

where χ_{opt} (M^{n+}) is the optical electronegativity of the closed-shell transition metal ion M^{n+} (Mo^{6+} in the present case) and $d(Pr^{3+}–M^{n+})$ is the shortest interatomic distance between Pr^{3+} and M^{n+}. This equation allows estimating the expected energy for the IVCT transition in the investigated material within ±1500 cm^{-1}. Its value, about 330 nm, is very close to the excitation edge associated to the perturbed molybdate absorption.

10–600 K luminescence spectra and emission dynamics of the Pr^{3+}-doped crystals

The 10 K emission spectra (Fig. 4.4) of the 0.5% doped crystals (C05) were measured upon excitation at 450 nm in correspondence of the $^3P_2 \leftarrow {}^3H_4$ absorption transition of Pr^{3+} and at 330 nm in correspondence of the host absorption edge and of the $Pr^{3+}(4f^{\,2})Mo^{6+}(5d^0) \rightarrow Pr^{4+}(4f^1)Mo^{5+}(5d^1)$ IVCT transition.

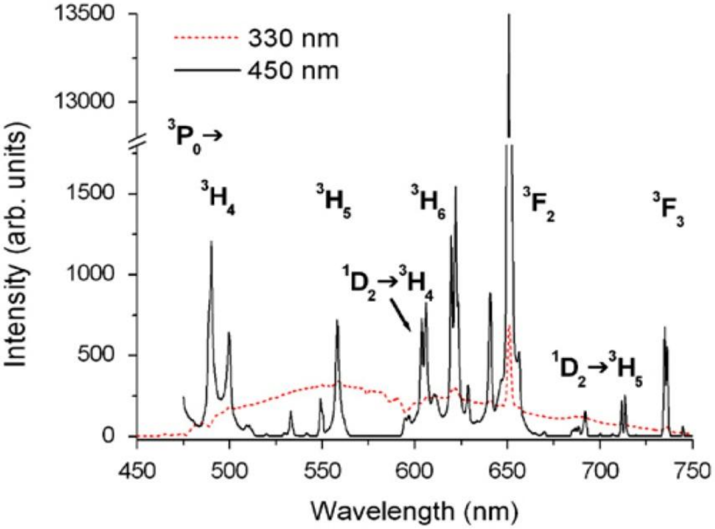

Fig. 4.4. Low temperature emission spectra of $CaMoO_4$:Pr^{3+}(C05). Excitation wavelengths: 450 nm (full line) and 330 nm (dotted line).

In the former case the spectrum consists of manifolds originating from the $^3P_0$ level, with the exception of two multiplets centered at 603 and at 690 nm that are assigned to transitions from the $^1D_2$ state. The observed features are inhomogeneously broadened (FWHM ranging from 40 to 100 cm^{-1}) in consequence of the local disorder around the active ions. The intensity of the $^3P_0 \rightarrow ^3F_2$ hypersensitive transition at 650 nm is high and compatible with a large value of the Ω_2 Judd–Ofelt parameter, in analogy with the $CaMoO_4$:Dy^{3+} case [11]. Only the most intense Pr^{3+} features are observable in the 330 nm excited spectrum, in which they are superimposed to the broad host emission. The dips observed in the 480 and 580 nm regions indicate radiative re-absorption from Pr^{3+}.

The room temperature emission spectra of the C01 and C05 crystals measured upon 450 nm excitation are presented in Fig. 4.5.

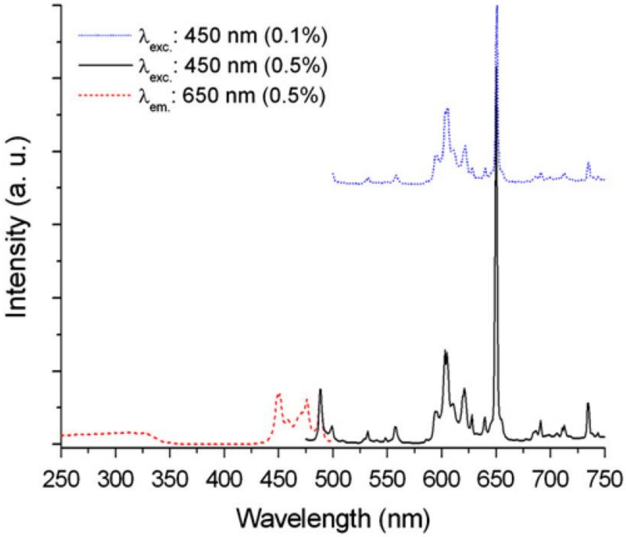

Fig. 4.5. Room temperature emission spectra of $CaMoO_4$:Pr^{3+} (C01 and C05 crystals) measured upon Pr^{3+} excitation. Excitation spectrum of the 650nm emission of C05.

It can be noted that the intensity ratio $R(^1D_2/^3P_0)$ between the $^1D_2$ and $^3P_0$ emission components decreases as the Pr^{3+} concentration is raised and increases as the temperature grows up. These effects result from the de-excitation of the $^3P_0$ state by $^3P_0 \rightarrow {}^1D_2$ multiphonon relaxation and by cross relaxation processes of the type:

$[^3P_0, {}^3H_4] \rightarrow [^1G_4, {}^1G_4]$ and $[^3P_0, {}^3H_4] \rightarrow [^1D_2, {}^3H_6]$

that are not resonant (the former in particular) and then favored by phonon assistance [23]. The cross relaxation involving the $^1D_2$ state:

$[^1D_2, {}^3H_4] \rightarrow [^1G_4, {}^3F_4]$

is in practice resonant, so that strong concentration and weak temperature dependences are expected for this process. These mechanisms are schematized in Fig. 4.6, the excitation process being denoted as the process (1).

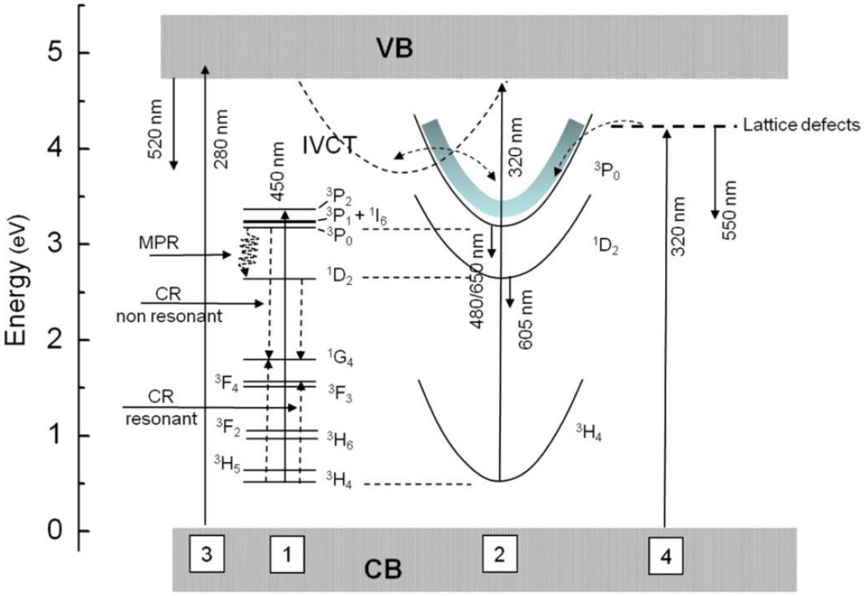

Fig. 4.6. 'Host lattice + doping ions' energy levels scheme showing the main de-excitation mechanisms following the host excitation. Full arrows indicate emission processes, dotted arrows non-radiative processes.

The excitation spectrum in Fig. 4.5 is composed of two bands systems: the most intense, in the 420–500 nm range, is assigned to the transitions from the $^3H_4$ ground state to the ^3P_J (J=0, 1, 2) and $^1I_6$ levels of Pr^{3+}. The second weaker system, located in the UV region, consists of a broad band ascribed to the host. The superimposition of the host and Pr^{3+} emission signals in the visible region makes it difficult to assess the nature and the effects of the interactions between the host lattice and the optically active dopants. To clarify the situation, in Fig. 4.7 we show the emission spectra measured upon different excitation wavelengths in the 280–340 nm range.

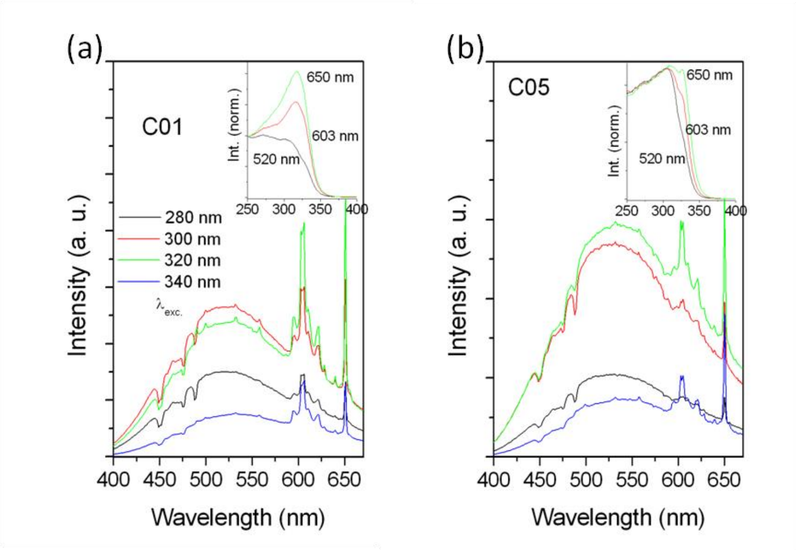

Fig. 4.7. (a) 298 K emission spectra of the C01 crystals excited at different wavelengths and (b) and 298 K emission spectra of the C05 crystals excited at different wavelengths.

The spectra are composed of the Pr^{3+} emission manifolds overlapping the broad host luminescence. Dips are also present on the high energy side of the host emission, indicating radiative Pr^{3+} re-absorption. In the case of the C01 crystals (Fig. 4.7a), the most intense spectra are those measured upon excitation at 300 and 320 nm. In general, the intensity ratio between the Pr^{3+} and host emissions increases as the excitation wavelength increases, whereas the relative depth of the re-absorption features increases as the excitation wavelength decreases. This indicates that different mechanisms are involved in the excitation of the Pr^{3+} emission. The 280–300 nm radiation absorbed by the bulk, i. e. by the 'regular' molybdate units, induces the formation of self trapped excitons (STEs), that can decay either radiatively giving rise to the broadband emission centered at 520 nm or non-radiatively through internal non-radiative relaxation and/or energy transfer processes. Owing to the lack of interconnection between the molybdate units, the migration of the STEs through the lattice is reduced and the probability of energy transfer to the rare earth centers very small. We therefore infer that the Pr^{3+} emission is mostly subsequent to radiative re-absorption of the host emission. Upon excitation in the 320–340 nm range, the dominant processes involve (1) the excitation of the perturbed molybdate centers and their radiative (broadband orange emission) or non-radiative (energy transfer) decays and (2) the population of the IVCT state, thus generating alternative de-excitation pathways. The presence of the IVCT band in the 320 nm region is clearly evidenced in the excitation spectra that are reproduced in the inset of Fig. 4.7a). Its intensity progressively grows up as the monitored emission wavelength shifts from 520 nm (regular host emission) to 650 nm (mostly Pr^{3+} $^3P_0 \rightarrow {}^3F_2$ transition). Other evidences of the IVCT effects are also provided by the analysis of the intensity ratio $R(^1D_2/^3P_0)$ vs the excitation wavelength and by investigating the temperature dependence of the Pr^{3+} emission signals up to 600 K. Comparing Figs. 4.5 and 4.7a, it is clear that $R(^1D_2/^3P_0)$ is larger upon excitation at 320 nm than upon excitation at 450 nm. This is explained by the fact that the excitation in the IVCT state is followed by radiationless relaxation to the $^1D_2$ level, by-passing partly the $^3P_0$ level [18]. Despite a general similarity of behavior, a careful analysis of Fig. 4.7 allows to evidence that the emission spectra of C05 differ from those of C01 in some aspects concerning: (1) a significant decrease of the intensity ratio between the Pr^{3+} and host emissions, (2) a weaker depth of the re-absorption features, (3) a slight red shift of the host emission maximum and (4) a negligible modification of the excitation spectra upon the monitored emission wavelength (see inset in Fig. 4.7b). It can be deduced from these observations that increasing the Pr^{3+} doping level in the crystal results in a lower excitation efficiency of the Pr^{3+} ions and/or in a reinforcement of the de-excitation rates operating on the excited Pr^{3+} centers. Concomitantly, the red shift of the host emission suggests an increase of the perturbed molybdate concentration.

Fig. 4.8 shows the temperature dependence of the emission spectra of C01 and C05 in the range 300–600 K, upon excitation at 337 nm.

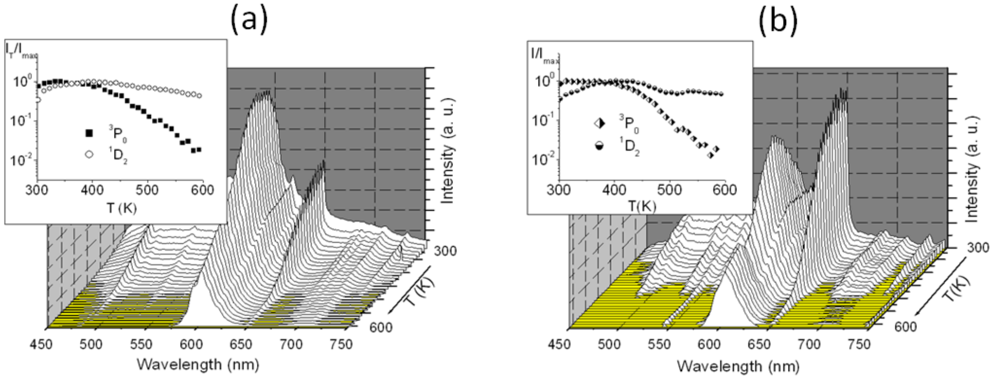

Fig. 4.8. Emission behavior in the high temperature regime. (a): CMO:Pr0.1%, $\lambda_{exc.}$: 337 nm and (b) CMO:Pr0.5%, λ_{exc}: 337 nm. The insets of the figures report the temperature behavior of the integrated intensities of the $^1D_2$ and $^3P_0$ emissions.

Similar behaviors are observed for both crystals: the integrated emission from the $^1D_2$ state is nearly constant with the temperature, whereas that from $^3P_0$ is characterized by a plateau in the 300–400 K range, followed by a marked decrease to almost complete quenching at 600 K. These trends are typically observed when the thermal depopulation of the $^3P_0$ state takes place through a cross-over to a Franck–Condon shifted state (IVCT), as observed for Pr^{3+}-doped $CaNb_2O_6$ and $YNbO_4$[18]. They are rather different from that occurring by mean of multiphonon relaxation and/or cross relaxation mechanisms, as in Pr^{3+}:$KLa(MoO_4)_2$ [3]. We have then reproduced the temperature evolution of the $^3P_0$ emission intensity by means of the Struck and Fonger model [24]:

$$\frac{I}{I_0} = \left[1 + A\exp\left(-\frac{\Delta E}{KT}\right)\right]^{-1} \qquad (4.1)$$

where A is close to 10^7 and ΔE is the activation energy from the emitting state to its crossover with the quenching state. Its value is of about 4100 cm^{-1}, and it is consistent with the relative positions of the parabolas associated to the $^3P_0$ and IVCT states in the single configurational coordinate diagram presented in Fig. 4.6.

The decay profiles of the host emission were measured at room temperature upon 337 nm excitation as a function of the Pr^{3+} doping level (Fig. 4.9a). They are similar one to another and can be reproduced by means of the sum of two exponential functions yielding decay times of 4 and 19 μs. These values are much shorter than the intrinsic lifetime of the emitting triplet state that is usually of the milliseconds order, and reflect the strong temperature quenching operating on the molybdate emission [15]. In principle these double exponential profiles could be related to the presence of regular and defect molybdate centers.

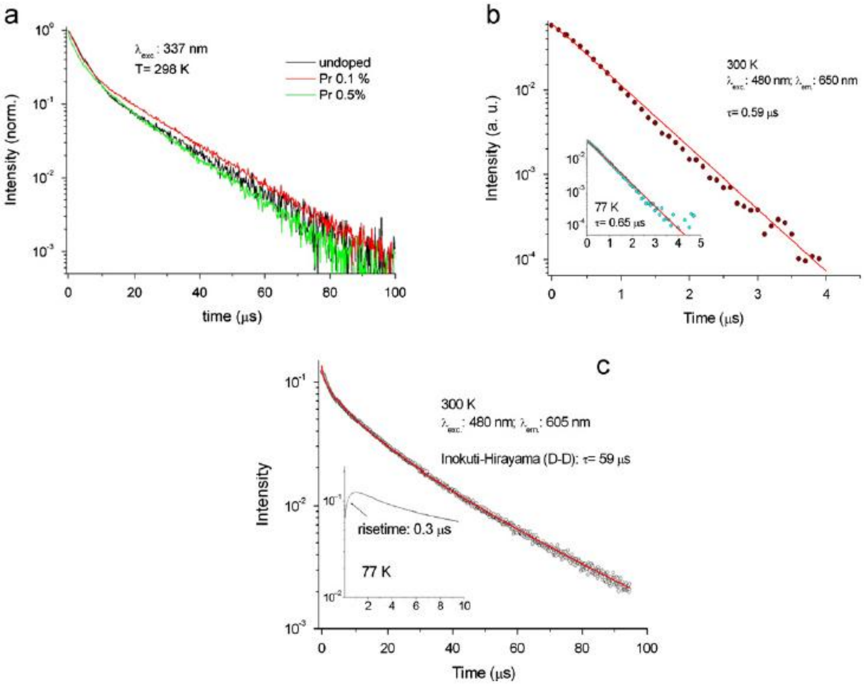

Fig. 4.9. Emission decay profiles of the broad band emission in pure and Pr^{3+} doped crystals (a) and of the $^1D_2$ (b) and $^3P_0$ emission (c) in CMO:Pr0.5%.

The Pr^{3+} decay profiles were measured at 77 and 298 K in C05, upon direct excitation into the ^3P_J (J=0, 1, 2) manifold. The $^3P_0$ emission (Fig. 4.9b) decays as a single exponential with a time constant of the order of 0.6 μs. This short value confirms that different processes contribute to the non-radiative depopulation of this level, as already pointed out. The $^1D_2$ decay curve (Fig.4.9c) is not single exponential. At 300 K it was reproduced by the Inokuti–Hirayama model for energy transfer in absence of migration [25]. We have fitted the decay curves by means of Eq. (1.16) by considering a *D–D* process and A, τ and α as adjustable parameters. The obtained τ value is 59 μs and the critical distance for the transfer, evaluated by means of Eq. (1.17), is of about 16 Å, consistent with the statistically estimated mean shortest distance between the doping ions in the lattice (15.5 Å). The mechanism responsible for this behavior is presumably the abovementioned cross relaxation process. The 77 K decay curve presents a risetime in its initial part, as a result of the feeding process from the upper $^3P_0$ level.

Luminescence spectra of the Pr^{3+}-doped powders

It is interesting to compare the spectra of the crystals to those of micro-sized polycrystalline SG07 and SS07 samples. These are reported in Fig. 4.10.

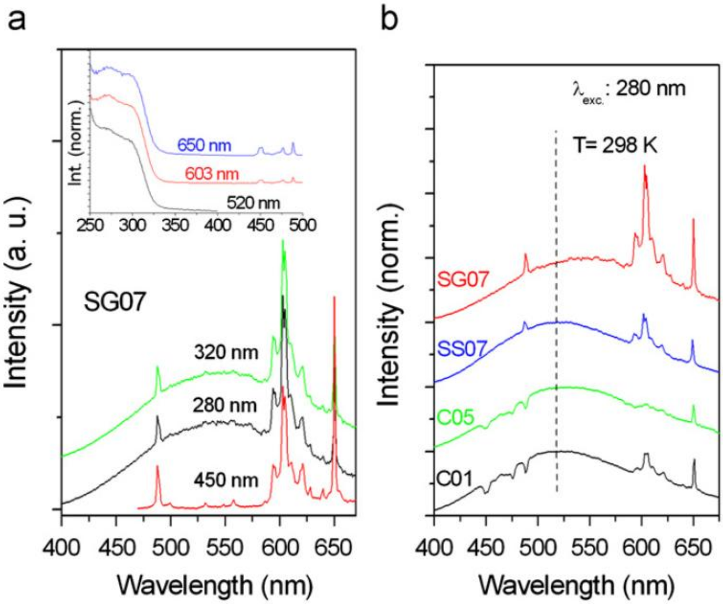

Fig. 4.10. (a) 298 K emission spectra of the SG07 sample upon different excitation wavelengths. In the inset: excitation spectra measured at different emission wavelengths. (b) comparison between the emission spectra of all samples upon 280 nm excitation. The spectra are normalised with respect to the broadband maximum.

We note: (1) the absence of re-absorption effects in the powders, (2) the independence of the structure of the UV excited emission on the excitation wavelength (Fig. 4.10a), (3) the high energy shift of the UV excitation band with respect to the crystals case (Fig. 4.7) and its independence on the monitored emission wavelength, (4) the much stronger intensity of this band relative to the Pr^{3+} intraionic and IVCT transitions (inset of Fig. 4.10a).This indicates that the Pr^{3+} emission in the powders is mostly governed by host sensitization processes, in agreement with the observations of Zhu et al. [6]. It is also interesting to note the red shift of the broadband emission in the SG07 spectrum compared to the SS07 spectrum (Fig. 4.10b). This is consistent with the more effective role of the defects associated to the wider distribution of the grain morphology and to the presence of nanoparticles.

4.4 Discussion

The UV excited luminescence processes of Pr^{3+}:$CaMoO_4$ have been summarily schematized in the diagram sketched in Fig. 4.6. In the low concentrated crystal (C01), the Pr^{3+} emission is mostly generated upon excitation in the IVCT state (process (2)). This charge transfer state originates from the photoinduced interaction between ‘regular’ MoO_4^{2-} units and Pr^{3+} ions. Internal relaxation then takes place to feed the $^3P_0$ and $^1D_2$ levels, and the relative population of these two levels depends on the temperature (Fig. 4.8). Most of the energy absorbed in the 280–300 nm region is relaxed radiatively as a broadband emission (process (3) of Fig. 4.6). Part of it is reabsorbed to raise the Pr^{3+} emission. As the Pr^{3+} concentration is raised in the crystal (C05), the probability for the STEs to carry their energy to a Pr^{3+} ion is increased and the re-absorption process is less probable (i.e. reduced dips in Fig. 4.7b). The Pr^{3+} emission is however not enhanced compared to C01 crystal because of the concomitant reinforcement of quenching processes (cross-relaxation mostly). In the powder samples, the density of perturbed molybdates centers is increased with respect to the single crystals, as attested by the broader emission profile (compare Fig. 4.7 and Fig. 4.10). The spectroscopic data (Fig. 4.10b) evidence that the maximum presence of defects is found in the SG07 case. Curiously, this is the sample in which the Pr^{3+} emission is the stronger upon excitation at 280 nm. In order to account for this behavior we have to consider that in the powders case the interaction with the excitation light gives rise to scattering processes to a much greater extent than in single crystals and constitutes, as a matter of fact, a superficial phenomenon. In these conditions the direct excitation of the Pr^{3+} ions ‘via’ intraionic $4f \rightarrow 4f$ or IVCT transitions become less efficient in consequence of the reduced penetration depth of the incident radiation. The remaining excitation process is the host sensitization. Moreover, it has to be pointed out that in the powder samples the nature of the defects is different and the probability of having Pr^{3+} ions located in proximity of perturbed molybdate units is much higher than in the crystals, in consequence of their morphological properties, of their higher doping level and also of their different charge compensation mechanisms, as pointed out in Section 3. We suppose, consistently with the behavior observed in Fig. 4.10, that the energy transfer process from the defect molybdate centers to the active dopants (described by process (4) of Fig. 4.6) could be relatively efficient, at variance with that involving the regular MoO_4^{2-} ions. The relative stronger Pr^{3+} emission features in SG07 (constituted in part by nano-sized particles) compared to SS07 is in agreement with this hypothesis, even if it could also be ascribed to a lower efficiency of cross-relaxation processes in the former case. We think in fact that the sol–gel methodology allows a better statistical distribution of the dopants within the host lattice than the solid state reaction procedure. In our opinion, the role played by the defect centers in the sensitization of the Pr^{3+} emission is certainly important but has yet to be fully understood.

4.5 Concluding considerations

The emission dynamics of the CMO:Pr system have been explored under different experimental conditions. Direct excitation of Pr^{3+} at 450 nm gives rise to a fluorescence spectrum composed of features originating in the $^3P_0$ and $^1D_2$ levels, whose relative intensities depend on intermanifold processes like multiphonon relaxation and cross relaxation processes. In the case of UV excitation the situation is much more complicated, since the experimental results have evidenced that the sample morphology plays an important role in determining the main mechanism involved in the de-excitation pathways. Measurements carried out on samples obtained by different synthetic routes have allowed us to stress the role of the lattice defects, that in the investigated system are optically active. In this connection, we have proposed two different host excitation mechanisms: in the single crystals the UV excitation energy is preferentially transferred to the Pr^{3+} ions from the ‘regular’ MoO_4^{2-} units through a mechanism involving the IVCT state, whereas in the powder materials the Pr^{3+} emission is mainly excited through the energy transfer from perturbed molybdate centers. This hypothesis is consistent with the experimental data and constitutes, in our opinion, a model that will be conveniently extended to the analysis of the optical properties of a number of analogous materials in order to verify its reliability. We are planning further work in this direction.

References

[1] A. A. Kaminskii, Crystalline Lasers: Physical Processes and Operating Schemes, CRC Press, New York, 1996.

[2] W. M. Yen, Phosphor Hand book, CRC Press, Boca Raton USA, 2000.

[3] E. Cavalli, P. Boutinaud, M. Bettinelli, P. Dorenbos, J. Sol. Stat. Chem. 181(2008) 1025.

[4] P. Dorenbos, A. H. Krumpel, E. vander Kolk, P. Boutinaud, M. Bettinelli, E. Cavalli, Opt. Mater. 32 (2010) 1681.

[5] E. G. Reut, A. I. Ryskin, Phys. Status Solidi (a) 17 (1973) 47.

[6] F. Zhu, Z. Xiao, F. Zhang, L. Yan, A. Huang, J. Lumin. 131 (2011) 22.

[7] F. Zhu, Z. Xiao, F.Zhang, L. Yan, A. Huang, Appl. Phys. A 101 (2010) 689.

[8] T. T. Basiev, A. A. Sobol, Y. K. Voronko, G.P. Zverev, Opt. Mater. 15 (2000) 205.

[9] J. Liu, H. Lian, C. Shi, Opt. Mater. 29 (2007) 1591.

[10] Z. Zhang, H. Chen, X. Yang, J. Zhao, Mater. Sci. Eng. B 145 (2007) 34.

[11] E. Cavalli, E. Bovero, A. Belletti, J. Phys. Condens. Matter 14 (2002) 5221.

[12] E. Gürmen, E. Daniels, J. S. King, J. Chem. Phys. 55 (1971) 1093.

[13] K. Momma, F. Izumi, J. Appl. Crystallogr. 41 (2008) 653.

[14] Y. Zhang, N. A. W. Holzwarth, R. T. Williams, Phys. Rev. B 57 (1998) 12738.

[15] J. A. Groenink, C. Hakfoort, G. Blasse, Phys. Status Solidi (a) 54 (1979) 477.

[16] M. Fujita, M. Itoh, S. Takagi, T. Shimizu, N. Fujita, Phys. Status Solidi (b) 243 (2006) 1898.

[17] C. Pu, T. Liu, Q. Zhang, Phys. Status Solidi (b) 245 (2008) 1586.

[18] P. Boutinaud, R. Mahiou, E. Cavalli, M. Bettinelli, J. Lumin. 122-123 (2007) 430.

[19] P. Boutinaud, P. Putaj, R. Mahiou, E. Cavalli, A. Speghini, M. Bettinelli, Spectroscopy Lett. 40 (2007) 209.

[20] P. Boutinaud, E. Cavalli, M. Bettinelli, J. Phys. Condens. Matter 19 (2007) 386230.

[21] A. Krumpel, E. van der Kolk, P. Dorenbos, P. Boutinaud, E. Cavalli, M. Bettinelli, Mater. Sci. Eng. B 14 (2008) 114.

[22] E. Cavalli, P. Boutinaud, R. Mahiou, M. Bettinelli, P. Dorenbos, Inorg. Chem.49 (2010) 4916.

[23] R. Naccache, F. Vetrone, A. Speghini, M. Bettinelli, J.A. Capobianco, J. Phys. Chem. C 112 (2008) 7750.

[24] C.W. Struck, W.H. Fonger, J. Appl. Phys. 42 (1971) 4515.

[25] M. Inokuti, F. Hirayama, J. Chem. Phys. 43 (1965) 1978.

Chapter 5

The luminescence of the Bi^{3+} ion in the $YP_xV_{1-x}O_4$ ($0\leq x\leq 1$) host lattice

5.1 Introduction

The beneficial effect of Bi^{3+} co-doping on the luminescence performance of different lanthanide ions has been demonstrated, among others, in various host materials like YAG [1], YBO_3 [2], $CaTiO_3$ [3], YPO_4 , YVO_4 and in their mixed phases [4-6]. Nevertheless, the nature of the sensitization mechanism is not always well assessed. In most cases, energy transfer processes are invoked in order to account for the increasing of the rare earth emission intensity, but sometimes the proposed mechanism is not fully convincing. In our opinion it is very important to understand as much as possible the spectroscopic properties of all active species involved in the luminescence dynamics, and for this reason we have decided to investigate systematically the optical spectroscopy of the Bi^{3+} ion along the YVO_4-YPO_4 mixed system. Old studies on the $YPO_4:Bi^{3+}$ luminescence report that this material emits at 330 nm upon 230 nm excitation [7, 8], whereas more recent VUV spectroscopy experiments [9] have revealed a strong emission band in the UV region, at 240 nm. The yellow luminescence of $YVO_4:Bi^{3+}$ was investigated in the late 60’s [7] and ascribed to the formation of a charge transfer state between host and doping ions. Investigations of the absorption and emission properties along with energy transfer processes in YVO_4 and Bi^{3+}-doped YVO_4 are reported in ref. 10. A recent paper [11] has confirmed the present interest on $YVO_4:Bi^{3+}$ but proposed an assignment in contrast with the previous results, evidencing the opportunity of at least an updated survey of its spectroscopic properties. Starting from the end members of the $Y(P_xV_{1-x})O_4$:Bi^{3+} series, we have then carried out a series of emission measurements as a function of the host composition, of the excitation wavelength and of the temperature. The results have been analyzed in the framework of a recently presented model [12] in which the Bi^{3+}-related yellow emitting state is identified with a metal-to-metal charge transfer (MMCT) state originating from the interaction of the doping ions with the vanadate host.

5.2 Experimental

Synthesis and structure

$Y(P_xV_{1-x})O_4$:Bi^{3+}(y%) (x= 0, 0.2, 0.5, 0.6, 0.7, 0.8, 1; y= 0, 0.1, 1, replacing Y^{3+}) phosphors were synthesized by a sol-gel Pechini methodology already described in previous papers [13, 14]. This route has been preferred with respect to the solid state reaction because it requires a final thermal treatment at lower temperature (900 °C instead of 1200 °C) preventing Bi^{3+} loss by sublimation and allowing a better control of the sample morphology. The zircon-like structure of YPO_4 and YVO_4 has already been described in Sect. 3.3. Powder x-ray diffraction (PXRD) studies along the mixed system [13] have confirmed that they form an isomorphic series. The Bi^{3+} doping ions replace Y^{3+} in dodecahedrally coordinated sites with D_{2d} point symmetry.

Spectroscopical measurements

VUV emission and excitation spectra of $YPO_4:Bi^{3+}$ were measured at the SUPERLUMI station of HASYLAB (DESY,Germany) using the synchrotron radiation (SR) from the DORIS III storage ring as excitation source. Luminescence measurements were carried out at the SUPERLUMI station of HASYLAB (Hamburg, Germany) using the SR from the DORIS III storage ring as excitation source. For the measurement of excitation spectra in the range of 3.7-19 eV a 2 m monochromator in McPherson mounting with a resolution of 3.2 Å was used. The detection of the luminescence was performed with a 0.3 m ARC SpectraPro-308i monochromator equipped with a high-speed R3809U-50S (Hamamatsu) microchannel plate detector. Time-integrated spectra were recorded counting emission signal within the whole time period of 192 ns available between SR pulses at the normal (5) bunch mode (BM) of the storage ring. The measurements were performed in the ultra-high-vacuum chamber (~10^{-9} mbar) at 7 and 300 K. The excitation spectra were corrected for the wavelength-dependent variation of the SR intensity using the sodium salicylate signal. Room temperature emission and excitation spectra were measured using a Fluoromax-3 (Jobin-Yvon) spectrofluorimeter. 10 K emission spectra were recorded using a spectroscopic system consisting of a 450 W Xe lamp fitted with a 0.2 m monochromator as source and a 1.26 m Spex monochromator with a RCA C31034 photomultiplier to analyze and detect the output radiation. The samples were mounted onto the cold finger of a He-cryocooler (Air Products Displex DE-202). The decay profiles were acquired in the temperature range 30 – 300 K using a HR1000 Jobin-Yvon monochromator, a R1104 Hamamatsu photomultiplier and a 400 MHz Lecroy digital oscilloscope with an input impedance of 50 Ohm. The samples were excited at 337 nm by a nitrogen laser or at 306.5 nm by means of the radiation generated by frequency doubling the output of a ND 60 dye laser operated with a Rhodamine 640 and pumped with a pulsed frequency doubled Nd:YAG laser. The quantum yields values and the trichromatic coordinates of all powders were measured at room temperature using the C9920-02G PL-QY measurement system from Hamamatsu. The setup comprises a 150 W monochromatized Xe lamp, an integrating sphere (Spectralon Coating, Ø = 3.3 inch) and a high sensitivity CCD camera for the detection of the whole spectral luminescence. The automatically controlled excitation wavelength range spread from 250 nm to 950 nm with a spectral bandwidth better than 5 nm.

5.3 Results and discussion

YPO_4:Bi^{3+}

The 7 K excitation and emission spectra of YPO_4:Bi^{3+} are shown in Fig. 5.1. The emission is composed of two bands peaking at 245 and 335 nm. As the temperature is raised to 298 K the relative intensity of the 335 nm broadband increases with respect to the narrow 245 nm emission (inset of Fig. 5.1). This band can be ascribed to the $^3P_1 \rightarrow {}^1S_0$ transition of Bi^{3+} [9]. The origin of the broad sideband still constitutes an open question. In fact, different hypotheses have been so far proposed for the assignment of the visible luminescence bands observed in Bi^{3+}-activated wide gap lattices, in consideration also of the properties of the host material and of the possible interactions with the doping ions. The most frequently invoked mechanism implies emission from trapped excitons [15-17]) or from Bi^{3+} pairs or clusters [18, 19].

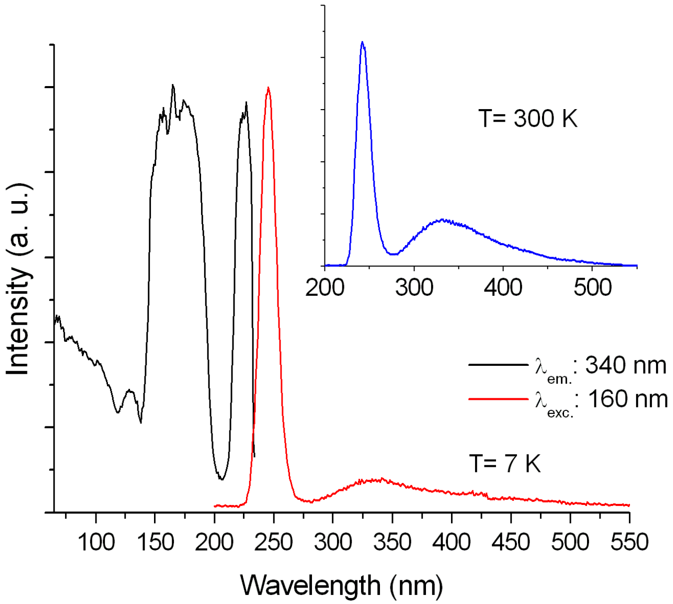

Fig 5.1 Excitation and emission spectra of $YPO_4:Bi^{3+}$.

The excitation spectrum is constituted of two main features: an intense single band at 227 nm, a composed system in the 150-190 nm region, both overlapping a baseline rising with increasing energy. They can be assigned to the $^3P_1 \leftarrow {}^1S_0$ and $^1P_0 \leftarrow {}^1S_0$ transitions of Bi^{3+} respectively.

YVO_4 and $YVO_4:Bi^{3+}$

The room temperature excitation and emission spectra of pure and 1% Bi^{3+}-doped YVO_4 are shown in Fig. 5.2a and b respectively. It is evident that in the case of the doped compound the absorption edge is significantly shifted towards lower energies. The excitation edge of pure YVO_4 is at about 335 nm, and its luminescence spectrum consists of a broadband in the blue region (maximum at around 440 nm).

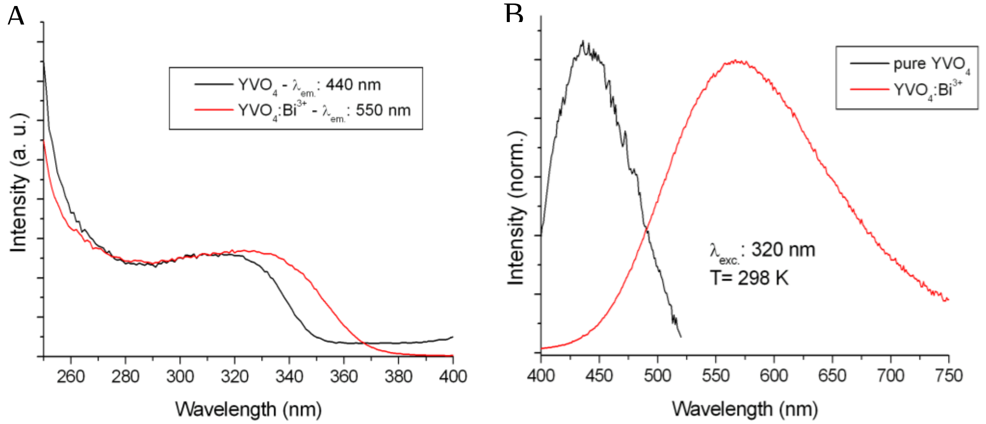

Fig. 5.2. Room temperature excitation (a) and emission (b) spectra of YVO_4 and $YVO_4:Bi^{3+}$. The spectra are normalized with respect to the emission maximum.

The luminescence of $YVO_4:Bi^{3+}$ is extended to the whole visible range, with maximum at around 570 nm, in the yellow region. The shape of the emission spectrum is independent on the excitation wavelength. The excitation edge is significantly shifted towards longer wavelengths with respect to the undoped compound, being located around 355 nm. The maximum of the excitation band in this compound is reported at 340 nm [7]. In the frame of a systematic investigation concerning Bi^{3+}-activated lattices [12] we have ascribed these features to transitions involving a metal-to-metal charge transfer state (MMCT) within the bismuth-vanadate complex, in general agreement with previous literature [7]. The excited MMCT state results from transitions between $Bi^{3+}(6s^2)$-$V^{5+}(3d^0)$ and $Bi^{4+}(6s^1)$-$V^{4+}(3d^1)$ configurations. It is also perceived as a trapped exciton state or referred to as a D-level state. In Fig. 5.3 we show the 10 K emission spectra of $YVO_4:Bi^{3+}$ measured upon different excitation wavelengths with a high resolution setup.

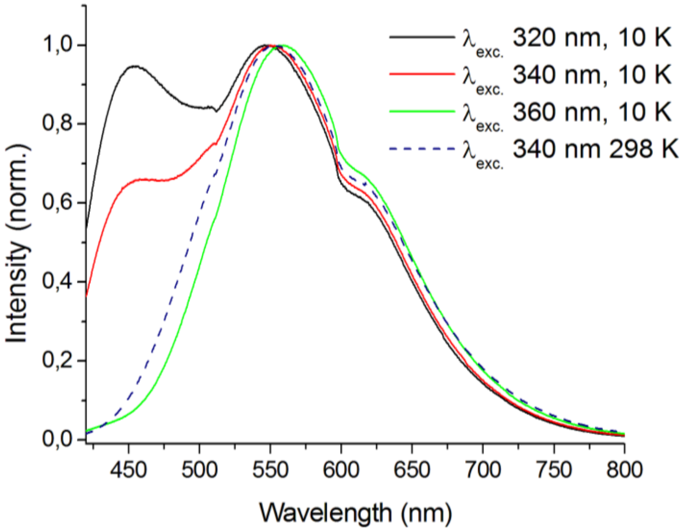

Fig. 5.3 Low temperature emission spectra of YVO_4:Bi^{3+} measured upon different excitation wavelengths.

First of all it is interesting to note that the MMCT emission presents at least two components with maxima at 550 and 630 nm. Moreover, the emission profile strongly depends on the excitation conditions, at variance with the room temperature case. In particular, excitation into the vanadate absorption band results in both blue and yellow emission, whereas excitation into the MMCT band (340-360 nm) yields the yellow emission only. These results are only in partial agreement with those of Moncorgé et al. [10], that only deal with the temperature behaviour of the yellow luminescence for a fixed excitation wavelength (337 nm). These observations can be accounted for in the frame of a model in which the MMCT process is considered as a transition from the ground state of Bi^{3+} to the conduction band of the host followed by a charge rearrangement that gives rise to the MMCT state. Analogously, the excitation of the VO_4^{3-} ion is followed by an intersystem crossing to the triplets states, with subsequent blue emission or energy transfer to nearby acceptors. It has been shown already that the host sensitization of the yellow emission in YVO_4:Bi^{3+} involves a migration process [10]. These processes are schematized in the configurational coordinate diagram of Fig. 5.4.

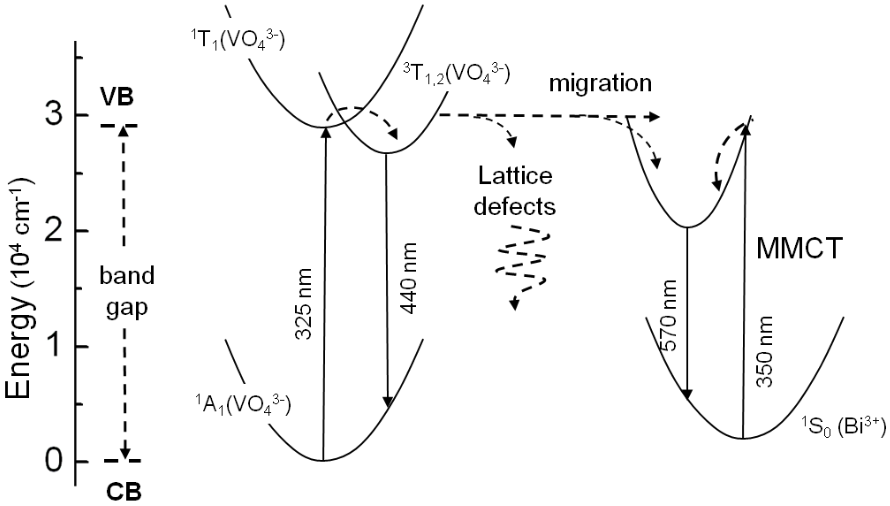

Fig. 5.4. Energy levels scheme illustrating the excited states dynamics of the YVO_4:Bi^{3+} system.

We have carried out a series of pulsed light experiments in order to obtain further information on the excitation mechanisms. The decay profile of pure YVO_4 is reported in Fig. 5.5: at 77 K it is a single exponential with decay time of 473 μs, whereas at room temperature it is approximately a double exponential whose major, and shorter, component has a decay time of 9 μs. These results indicate strong quenching of the vanadate emission. They are in perfect agreement with those reported by Moncorgé et al. [10], who proposed an excitonic model including the formation of self trapped excitons (that can be identified with the vanadate triplet states) and a thermally activated energy migration to radiationless quenching sites (see Fig. 5.4).

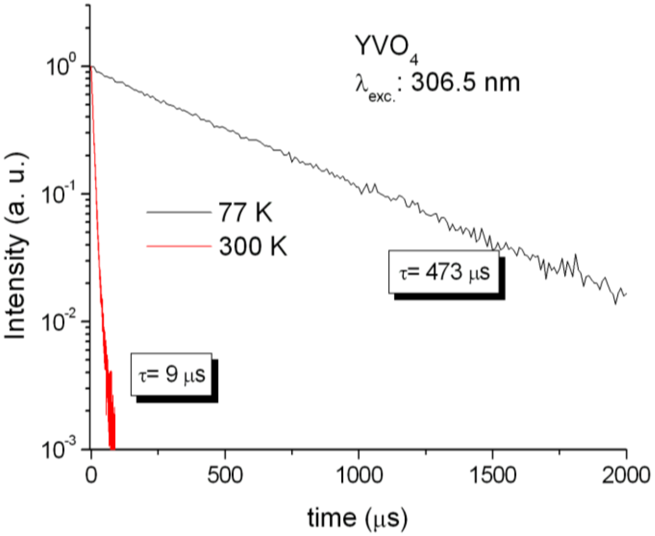

Fig. 5.5. Decay profiles of the host emission.

The decay profiles of $YVO_4:Bi^{3+}$ have been measured upon 306 and 337 nm excitation in the temperature range 77 – 300 K, for two different doping concentrations. Direct pumping into the MMCT band maximum at 337 nm results in single exponential, nearly temperature and concentration independent profiles with decay times of about 4.5 μs, indicating that the emission from the MMCT state is scarcely affected by non radiative processes. We checked that the vanadate emission has negligible contribution under these conditions. These results are in good agreement with those reported by Moncorgé et al. [10]. They supposed that Bi^{3+} induces a distortion of the surrounding vanadate units creating host traps which can trap the excitons and transfer the energy to their nearby activators. The nature of these activators was not explicitly specified. In this connection our interpretative scheme based on the formation of the MMCT state clarifies this aspect and is substantially compatible with the analysis carried out in ref. [10]. As a matter of fact it constitutes a significant evolution of the previously proposed model, supported by a systematic study [12] and new experimental results.

Excited at 306.5 nm, the MMCT emission exhibits very different decays with respect to the temperature. At room temperature (Fig. 5.6b) they are exponential with a time-constant of 5.5 µs and present a build up. The rise time is shorter (0.42 µs) for YVO_4:1%Bi^{3+} and longer (0.69 µs) for YVO_4:0.1%Bi^{3+}. This result confirms that the MMCT state is fed by energy transfer from the host excited states. At 77 K, the migration process is hampered. The decay curves consist of the sum of a long and of a short living component (Fig. 5.6c). The long component has a time constant ranging from 413 µs in YVO_4:1%Bi^{3+} to 446 µs in YVO_4:0.1%Bi^{3+}. It is ascribed to the VO_4^{3-} emission that is not quenched at this temperature and has some contribution at 520 nm. The short living component is ascribed to the MMCT emission, mostly induced by direct energy transfer from the nearest neighbour excited vanadate ions. We show in Fig. 5.6d the decay profiles of the vanadate emission that is observed in YVO_4:Bi^{3+} upon excitation at 306.5 nm. At 77 K, the decay is exponential with a time constant close to that of the undoped compound. At 295 K (inset of Fig. 5.6d), the decay becomes strongly non exponential with a time constant much shorter than in undoped YVO_4. This confirms that part of the energy absorbed by the host is transported by migration to Bi^{3+} ions only when temperature is higher than 77 K.

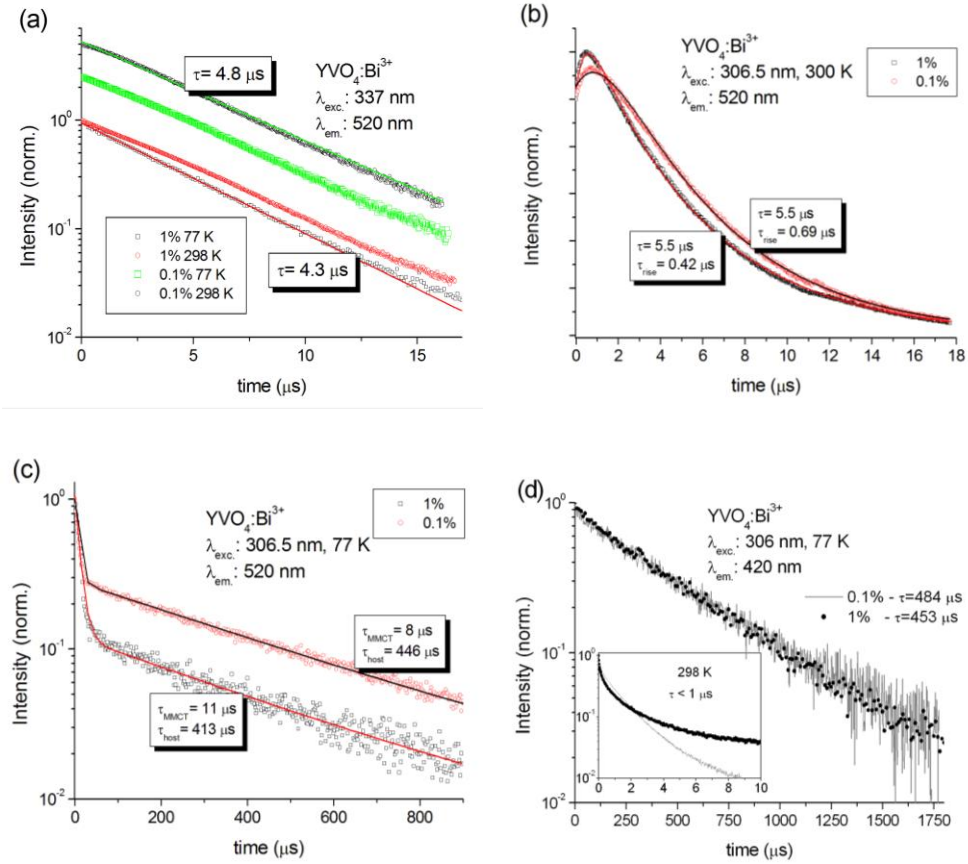

Fig. 5.6. (a) Decay profiles of the yellow emission measured upon MMCT excitation. Full line: single exponential fit; (b) room temperature decay profiles of the yellow emission measured upon host excitation. Full line: fit with difference of exponential function; (c) low temperature decay profiles of the yellow emission measured upon host excitation. Full line: double exponential fit; (d) decay profiles of the blue emission measured upon host excitation.

$Y(P_xV_{1-x})O_4:Bi^{3+}$

The room temperature luminescence spectra along the $Y(P_xV_{1-x})O_4:Bi^{3+}$(1%) (x= 0.2, 0.5, 0.8) compositions have been measured upon different excitation wavelengths and are shown in Fig. 5.7.

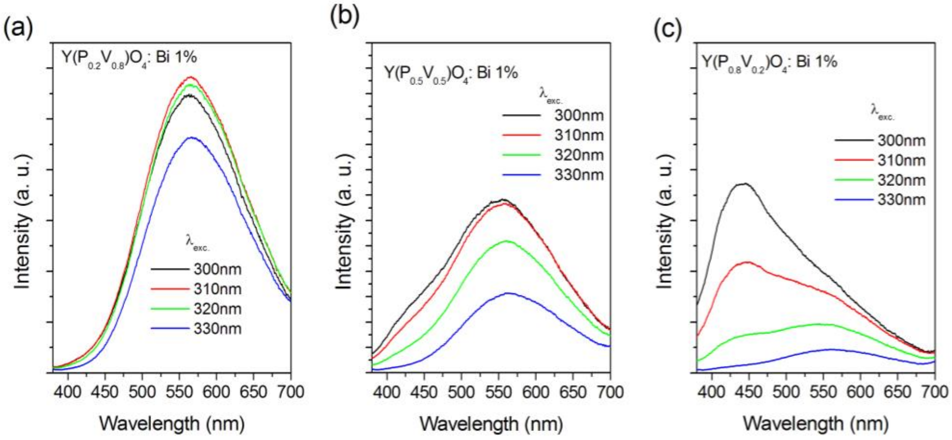

Fig. 5.7. Room temperature emission spectra of $Y(P_xV_{1-x})O_4$:Bi^{3+}(1%). a) x= 0.2; b) x= 0.5; c) x= 0.8. The intensity scale is the same for all spectra, for sake of comparison.

For x= 0.2 (Fig. 5.7a) the observed behaviour is practically identical to that of YVO_4:Bi^{3+}. For x= 0.5 (Fig. 5.7b) the appearance of an incipient blue component is discerned in the emission spectra excited at wavelengths shorter than 320 nm, i. e. upon host excitation. For x= 0.8 (Fig. 5.7c) the emission properties are strongly dependent on the excitation wavelength: the intensity ratio between the blue and the yellow band as well as the overall emission intensity strongly decrease on moving from the host to the MMCT excitation. In this phosphor, the migration process is strongly limited by the amount of VO_4^{3-} units. As a consequence, the luminescence properties are essentially regulated by direct excitation and energy transfer processes occurring between isolated centers. The emission spectra shown in Fig. 5.8 were collected at 10 K with the high resolution setup for x= 0.5 and x= 0.8. The results confirm that the vanadate sensitization of the Bi^{3+} luminescence occurs through a thermal assisted migration process.

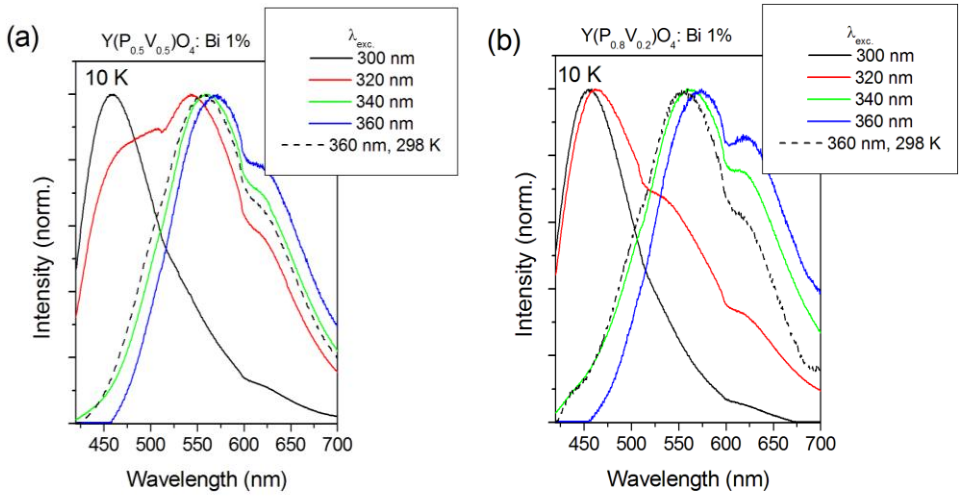

Fig. 5.8. Low temperature, high resolution emission spectra of $Y(P_xV_{1-x})O_4$:Bi^{3+}(1%). a) x= 0.5; b) x= 0.8. The spectra are normalized.

We further note that the maximum of the MMCT emission undergoes a red shift as the excitation wavelength is increased (for a fixed composition of matter) and on passing from x= 0 (maximum at 558 nm, Fig. 5.3) to x = 0.8 (maximum at 573 nm, Fig. 7.8), for a given excitation wavelength. For the phosphate-rich compound, the relative contribution of the 630 nm emission band is significantly enhanced. The decay curves for the two components of the MMCT emission monitored at 520 and 660 nm upon excitation at 337 nm are shown in Fig. 5.9a for the compound $YP_{0.8}V_{0.2}O_4$:1%Bi^{3+}. They are nearly single exponential, with slightly different decay times. The decay profiles of the host vanadate emission was measured in the same compound at 300 and 77 K, upon 306 nm excitation (Fig. 5.9b). Both are nearly single exponential, with decay times (195 and 830 μs) much longer than in the case of the pure vanadate host. This effect is obviously a consequence of the fact that the migration of the excitation is strongly inhibited in this host lattice.

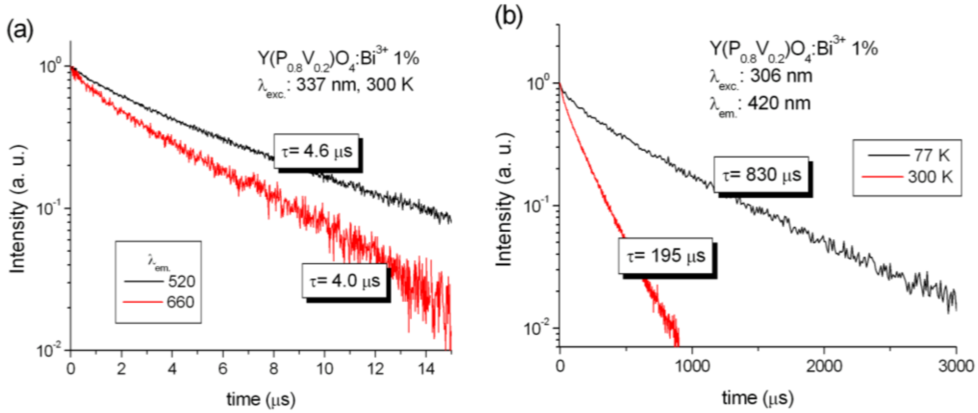

Fig. 5.9. Decay profiles of the $Y(P_{0.8}V_{0.2})O_4:Bi^{3+}$(1%) emission upon MMCT excitation (a) and host excitation (b).

Color measurements and quantum yield

In order to explore the perspective of application of the materials under investigation, we have measured their color coordinates and the internal quantum yields (i. e. the ratio between the integrated intensities of the absorbed and emitted radiation) for different excitation wavelengths. The results are summarized in Tab. 5.1. It is worth noting that the internal quantum yield significantly decreases on passing from x= 0 to x= 0.8, evidencing again the role of the migration in the luminescence process.

In agreement with the emission spectra, the color coordinates are nearly independent on the excitation wavelength for low x values, 0 and 0.2.

Tab. 5.1. Color coordinates and quantum yield along the $Y(P_xV_{1-x})O_4$:Bi^{3+} (1%) series as a function of the excitation wavelength. The format is: X, Y (IQY), where X and Y are the color coordinates (CIE 1931) and IQY the internal quantum yield.

	λ_{exc} = 290 nm	**λ_{exc} = 300 nm**	**λ_{exc} = 310 nm**	**λ_{exc} = 320 nm**
x=0	0.401, 0.479 (0.753)	0.403, 0.480 (0.881)	0.405, 0.482 (0.924)	0.408, 0.483 (0.929)
x=0.2	0.391, 0.471 (0.798)	0.391, 0.470 (0.885)	0.393, 0.471 (0.892)	0.397, 0474 (0.822)
x=0.5	0.335, 0.402 (0.650)	0.339, 0.407 (0.702)	0.349, 0.419 (0.641)	0.366, 0.438 (0.466)
x=0.6	0.295, 0.343 (0.686)	0.302, 0.351(0.729)	0.320, 0.375 (0.656)	0.345, 0.405 (0.481)
x=0.7	0.262, 0.295 (0.613)	0.271, 0.308 (0.588)	0.289, 0.333 (0.459)	0.319, 0.372 (0.238)
x=0.8	0.224, 0.236 (0.540)	0.236, 0.255 (0.507)	0.260, 0.291 (0.353)	0.301, 0.345 (0.177)

As x increases, the dependence of the emitted color on the excitation wavelength progressively increases, as evidenced in Fig. 5.10.

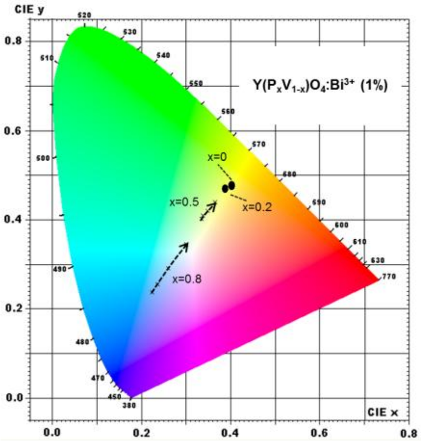

Fig. 5.10. Chromaticity diagram showing the color coordinates of the investigated materials and their evolution with the increasing excitation wavelength (cfr. Tab. 5.1).

The color of the luminescence ranges from blue to yellow depending on the composition and on the excitation wavelength. For sake of example, Fig. 5.11 shows the luminescence along the phosphor series upon 254 nm lamp excitation.

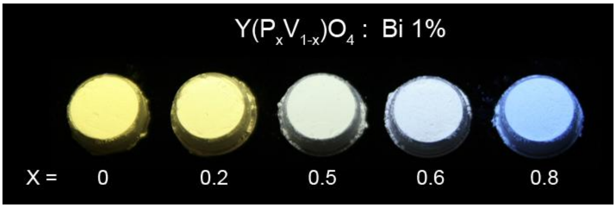

Fig. 5.11 Luminescence along the phosphor series upon 254 nm lamp excitation.

We think that the developed materials could have interesting device potentialities thanks to their versatility and efficiency.

Unfortunately, for the white emitting LED market, the fact that these phosphors cannot be excited at wavelengths longer than 320-330 nm constitutes a serious drawback. We therefore plan to study other phosphate-vanadate mixed systems with the aim of extending the excitation range to the NUV or the blue region.

5.4 Concluding remarks

The emission spectrum of YPO_4:Bi^{3+} presents an intense transition at 245 nm and a weaker and broader feature at around 335 nm, whose asymmetric shape indicates that it is composed of at least two bands. In the spectrum published by Jüstel [9] this feature was barely observable and not discussed in the analysis of the experimental data. It was also observed by Blasse et al. [7, 8] and erroneously assigned to the intrinsic Bi^{3+} emission, most likely in consequence of instrumental limits preventing to explore the whole UV region in which this material emits. In more recent studies on Bi^{3+}-doped into wide bandgap lattices, a similar emission was interpreted as the radiative decay of an exciton state arising from a photoionization process in which the luminescent center ejects an electron into the host lattice conduction band [15-17]. This results in the formation of an impurity bound exciton state in which the electron is delocalized in the host lattice and the hole trapped at the luminescent center. The analogy with the MMCT model proposed in order to account for the yellow $YVO_4:Bi^{3+}$ luminescence is rather evident, even if the two cases present important differences. The bandgap YPO_4 is in fact around 8.6 eV, whereas that of YVO_4 is of the order of 3.9 eV (21). The excited levels of Bi^{3+} are then presumably located within the host band gap in the former case and in the conduction band in the latter. As a consequence the Bi^{3+} excitation results in $^3P_1$ emission in the phosphate and in a photoionisation process involving the formation of a MMCT state in the vanadate lattice. Our experimental data however demonstrates that the MMCT state can be efficiently populated upon host excitation through energy migration.

Another aspect deserving attention concerns the nature of two components of the MMCT emission band. Their decay times, 4.6 μs for the 550 nm and 4.0 μs for the 630 nm band, are rather similar, consistently with the fact that they have the same origin. On the other hand the slightly faster decay of the red component could be a signal of higher probability of the corresponding transition. The spectra of Fig. 5.8 evidence that: i) the red shift of the emission maximum increases with the excitation wavelength and the temperature, and the entity of this shift is directly proportional to the P content and ii) the relative intensity of the 630 nm component as well as its variation with the increasing excitation wavelength increase as the P content increases (i. e. with x increasing). Different hypotheses can be considered in order to account for these observations. For instance, they could be certainly compatible with a local perturbation effect on the coordination environment of the emitting center, ascribable to the presence of lattice defects in proximity of the MMCT state. Another possibility could be related to a symmetry splitting of the involved electronic states, whose definition is not straightforward, considering that the emitting center consists of a cluster including at least two optically active ions that could be affected by the progressive substitution of P for V. Other effects could be taken into account, like the presence of Bi^{3+} pairs, clusters, and so on.

In conclusion, we have carried out a systematic investigation of the emission properties of the $Y(P,V)O_4:Bi^{3+}$ system. We have discussed the nature of the observed transitions by considering the previous literature and analyzed the effect of the host composition on the luminescence dynamics. The application of the MMCT model proposed in ref. [12] has allowed to interpret in a reliable way the experimental data and to stress the role of the migration process in the population of the emitting states. Finally, the emission performances of the developed materials have been measured in order to provide useful information in the perspective of technological application.

References

[1] A.1 Z. Mu, Y. Hu, L. Chen, X. Wang, J. Lumin. 131 (2011) 1687.

[2] A.2X. Zeng, S.-J. Im, S.-H. Jang, Y.-M. Kim, H.-B. Park, S.-H. Son, H. Hatanaka, G.-Y. Kim, S.-G. Kim, J. Lumin. 121 (2006) 1.

[3] A.3 W. Jia, A. Perez-Andújar, I. Rivera, J. Electrochem. Soc. 150 (2003) H161.

[4] Y. He, M. Zhao,Y. Song, G. Zhao, X. Ai, J. Lumin. 131 (2011) 1144.

[5] Z. Xia, D. Chen, M.Yang, T. Ying, J. Phys. Chem. Sol. 71 (2010) 175.

[6] J. Sun, J. Xian, Z. Xia, H. Du, J. Lumin. 130 (2010) 1818.

[7] G. Blasse, A. Bril, J. Chem. Phys. 48 (1968) 217.

[8] A.M. van de Craats, G. Blasse, Mat. Res. Bull. 31 (1996) 381.

[9] T. Jüstel, P. Huppertz, W. Mayr, D.U. Wiechert, J. Lumin. 106 (2004) 225.

[10] R. Moncorgé, G. Boulon, J. Lumin. 18-19 (1979) 376.

[11] J. Li, J. Liu, X. Yu, J. Alloys Comp. 509 (2011) 9897.

[12] P. Boutinaud, E. Cavalli, Chem. Phys. Lett. 503 (2011) 239.

[13] F. Angiuli, F. Mezzadri, E. Cavalli, J. Solid State Chem.184 (2011) 1843.

[14] F. Angiuli, E. Cavalli, A. Belletti, J. Solid State Chem., 192 (2012) 289.

[15] A.M. Srivastava, W.W. Beers, J. Lumin. 81 (1999) 293.

[16] G. Blasse, C. de Mello Donega, I. Berezovskaya, V. Dotsenko, Sol. Stat. Comm., 91 (1994) 29.

[17] V. P. Dotsenko, I.V.Berezovskaya, N.P. Efryushina J. Solid State Chem. 57 (1996) 437.

[18] A. M. Srivastava, Mat. Res. Bull. 37 (2002) 745.

[19] A. A. Setlur, A. M. Srivastava, Opt. Mater. 29 (2006) 410

[20] W. Barendswaard, R. T. Weber, J. H. van der Waals, J. Chem. Phys. 87 (1987) 3731.

[21] P. Dorenbos, A.H. Krumpel, E. van der Kolk, P. Boutinaud, M. Bettinelli, E. Cavalli, Opt. Mater. 32 (2010) 1681.

Chapter 6

Role of Bi^{3+} co-doping on the luminescence properties of YPO_4 activated with RE^{3+} (RE= Tb, Sm, Nd or Eu)

6.1 Introduction

The enhancing effect of Bi^{3+} on the luminescence of rare earth ions has been observed in several host lattice. In particular the sensitization of rare earth ions by Bi^{3+} in various systems including YPO_4 was investigated by Blasse and Bril [1] in a pioneering paper, in which they compared the efficiencies of the involved energy transfer processes and formulated qualitative hypotheses concerning their mechanisms.

In this Section we present a study on the spectroscopic properties of YPO_4 activated with Tb^{3+}, Sm^{3+}, Nd^{3+} or Eu^{3+} and the effect of the Bi^{3+} co-doping on the emission performances of these systems.

YPO_4 is an attractive host lattice for trivalent rare earth ions thanks to its favorable physico-chemical properties like high and extended transparency, thermal and chemical stability, structural characteristics, and it is extensively investigated in order to develop phosphors for solid state lighting, PDP technology, etc. [2].

The yttrium phosphate lattice is very suitable to study the role of bismuth co-doping in the sensitization of the rare earth luminescence since its large bandgap and the absence of host-rare earth energy transfer.

6.2 Experimental

Synthesis

Rod-like YPO_4 crystals nominally doped with 1% Tb (molar ratio with respect to Y) with average size $6\times2\times1$ mm^3 (see Fig. 6.1) were grown by the 'flux growth' technique using $Pb_2P_2O_7$ as a solvent in the 1300–800 °C temperature range [3].

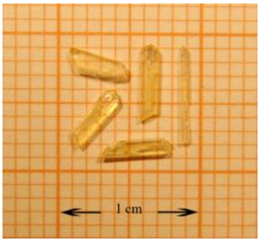

Fig 6.1. Crystals of YPO_4:Tb 1% grown from $Pb_2P_2O_7$ flux.

Four series of samples with composition $Y_{0.95-y}Tb_{0.05}Bi_yPO_4$ (y= 0, 0.0025, 0.005, 0.01, 0.025), $Y_{0.98-y}Sm_{0.02}Bi_yPO_4$ (y= 0, 0.005, 0.01, 0.025, 0.05), $Y_{0.99-y}Nd_{0.01}Bi_yPO_4$ (y= 0, 0.025) and $Y_{0.98-y}Eu_{0.02}Bi_yPO_4$ (y= 0, 0.025) were synthesized by Pechini sol-gel method. Stoichiometric amounts of Y_2O_3, $(NH_4)H_2PO_4$, RE_2O_3 (RE= Sm, Nd or Eu) or Tb_4O_7 and Bi_2O_3 (Aldrich, 99.9%) were dissolved in 3 M HNO_3 water solution at 75 °C under vigorous stirring. Citric acid with a 2:1 M ratio with respect to the metal ions was then added as chelating agent and PEG (20% w/w) as gelling agent. The obtained gel was dried at 80 °C for 4 h and successively at 120 °C for 12 h in order to remove the nitric acid. The phosphors were finally obtained after calcination at 500 °C for 2 h and successively at 900 °C for 2 h. The phosphors with composition $Y_{0.95-y}Tb_{0.05}Bi_yPO_4$ (y= 0, 0.0025, 0.005, 0.01, 0.025) were synthesized also by solid state reaction. Stoichiometric amounts of Y_2O_3 (Aldrich, 99.99%), $(NH_4)H_2PO_4$ (Merck), Tb_4O_7 (Aldrich, 99.9%) and Bi_2O_3 (Aldrich, 99.9%) were thoroughly mixed in alumina crucible and heated first at 900 °C for 12 h (heating rate 100 °C/h) and finally at 1200 °C for 12 h (heating rate 300 °C/h).

Characterization

The samples were characterized by powder XRD and SEM microscopy, as described in Sect. 3. The room temperature emission and excitation spectra were measured using a Fluoromax-3 (Jobin–Yvon) spectrofluorimeter. The excitation spectra were not corrected for the system responsivity because the calibration curves of the setup were not extended to the wavelength range of interest. The low temperature spectra were recorded using a spectroscopic system made up of a 450W Xenon lamp fitted with a 0.20 m monochromator as source, and a 1.26 m Spex monochromator with a RCA C31034 photomultiplier to analyze and detect the output radiation. The crystals were mounted onto the cold finger of a closed cycle He-cryocooler.

The Tb^{3+} decay profiles were measured at 300 K upon 355 nm laser excitation using a pulsed Nd:YAG laser (Quanta System model SYL 202); the emission was isolated by means of a Hilger–Watts Model D330 monochromator and detected with a Hamamatsu R943-022 photomultiplier connected to a LeCroy WS422 transient digitizer. The same setup was used to measure the Nd^{3+} decay curves. In this case the excitation wavelength was 532 nm. The Sm^{3+} decay profiles were acquired in the temperature range 30–300K using a HR1000 Jobin-Yvon monochromator, a R1104 Hamamatsu photomultiplier and a 400 MHz Lecroy digital oscilloscope with an input impedance of 50 Ω. The 406.1 nm radiation was the second anti-Stokes line generated in a H2 Raman cell positioned at the output of a

ND 60 dye laser operated with a Rhodamine 640 and pumped with a pulsed frequency doubled Nd:YAG laser. The quantum yields values and the trichromatic coordinates of all powders were measured using C9920-02 G PL-QY measurement system from Hamamatsu. The setup comprises a 150W monochromatized Xe lamp, an integrating sphere (Spectralon Coating, Ø= 3.3 in) and a high sensitivity CCD camera for detecting the whole spectral luminescence. The automatically controlled excitation wavelength range spread from 250 nm to 950 nm with a resolution bandwidth better than 5 nm.

6.3 Structural data and morphology

YPO_4 has a tetragonal zircon-type structure with $I4_1/amd$ space group and cell parameters a=b=6.8817 and c=6.0177 Å [4, 5]. The RE^{3+} and Bi^{3+} doping ions enter the Y^{3+} sites having eightfold oxygen coordination and D_{2d} point symmetry. The structure (Fig. 6.2) can be described as built from chains of alternating edge-sharing PO_4 tetrahedra and YO_8 dodecahedra extending parallel to the crystallographic *c* axis and joined laterally by ‘zigzag’ chains parallel to the *a* axis.

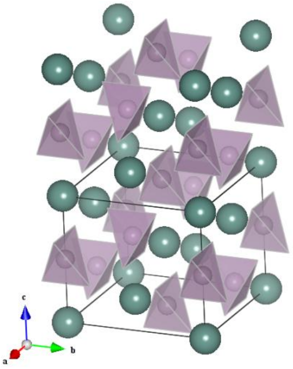

Fig. 6.2. Structure of YPO_4 (realized with the VESTA software [6]).

Representative XRD patterns of the SS*x* (solid state) and SG*x* (sol gel) phosphors are shown in Fig. 6.3. The comparison with the reference pattern of YPO_4 (JCPDS 11–0254 card) clearly evidences the formation of a single phase and the total absence of unwanted impurities. The structure of the patterns is independent of the Bi^{3+} concentration in the considered range.

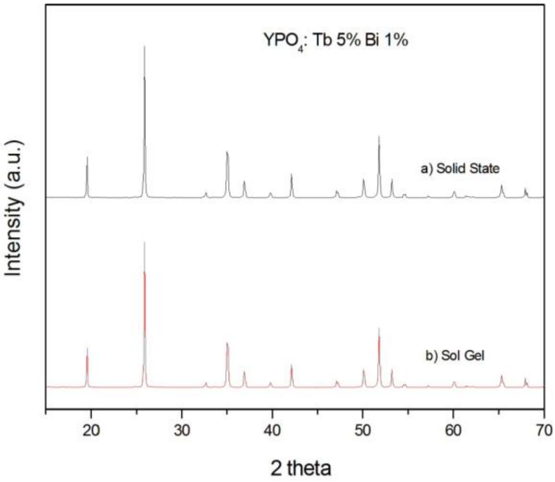

Fig. 6.3. XRD patterns of $Y_{0.94}Tb_{0.05}Bi_{0.01}PO_4$ synthesized by solid state reaction and sol–gel method.

The SEM images of these samples are shown in Fig. 6.4.

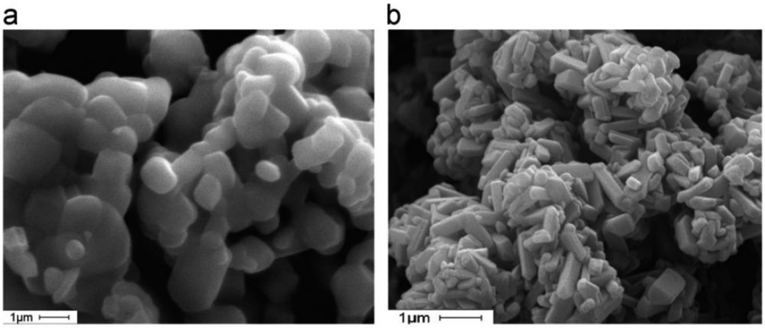

Fig. 6.4. SEM images of $Y_{0.94}Tb_{0.05}Bi_{0.01}PO_4$ synthesized by the solid state reaction (a) and sol–gel method (b).

It can be observed that their morphologies differ significantly: the particles prepared by solid state reaction have smooth surface and their size distribution is in the 0.5–2 μm range while those obtained by sol–gel technique have well defined elongated shape, similar to that of the flux grown single crystals, and are smaller, their size distribution being in the 200–800 nm range.

6.4 $YPO_4:Tb^{3+}, Bi^{3+}$

$YPO_4:Tb^{3+}$ single crystals

The measurements on single crystals have been carried out in order to obtain information about the emission dynamics and the performance of the investigated system. The 10 K emission spectrum is shown in Fig. 6.5.

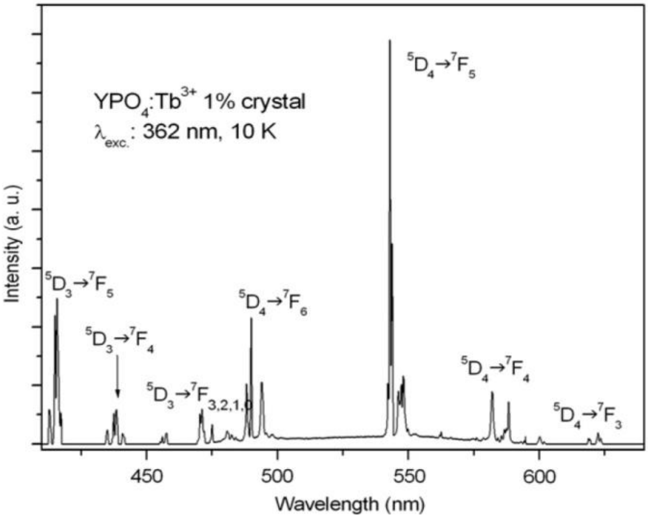

Fig. 6.5. 10 K emission spectrum of $YPO_4:Tb^{3+}$ 1% crystals.

It is composed of manifolds originating in both $^5D_3$ and $^5D_4$ levels, constituted by relatively narrow components, the full width at half maximum (FWHM) being of the order of 20 cm^{-1}. This confirms the good quality of the grown crystals and provides a reliable indication for the evaluation of the emission characteristics of the phosphor materials in relation with their morphological properties. The number of the components is consistent with that expected from the D_{2d} crystal field (CF) splitting of the energy levels of Tb^{3+}, that is a non-Kramers ion. The most intense line is located in the green, at 543 nm, and belongs to the $^5D_4 \rightarrow {}^7F_5$ multiplet. The $^5D_3$ emission bands lie below 480 nm. Their presence introduces a blue component that would alter the purity of the green emission of the phosphor. The adopted Tb^{3+} concentration in the powder samples (5%) induces the nearly complete quenching of the $^5D_3$ emission through cross relaxation processes like:

$$^5D_3,\ {}^7F_6 \rightarrow {}^5D_4,{}^7F_0 \qquad (6.1)$$

The analysis of the emission decay curves is consistent with this mechanism.

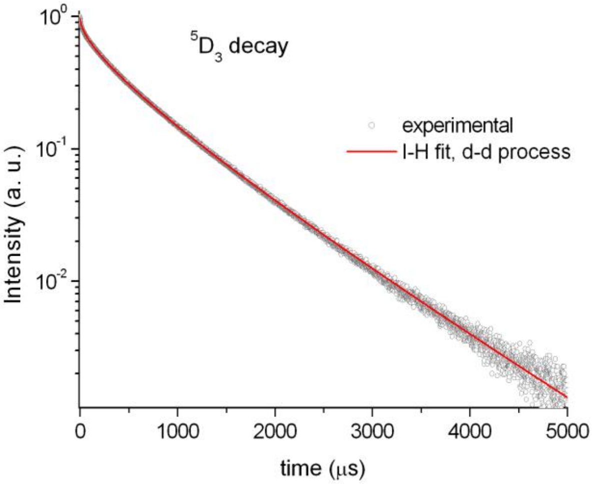

Fig. 6.6. Decay profile of the $^5D_3$ emission.

The temporal evolution of the luminescence from the $^5D_3$ level, shown in Fig. 6.6, has the non exponential profile typical of an energy transfer process in absence of migration, and it can be reproduced by the Inokuti–Hirayama model described in Sect. 2. We have fitted the decay curve by means of Eq. (2.16) by considering a *D*–*D* process and A, τ and α as adjustable parameters. The obtained τ value is 1.1 ms and the critical distance for the transfer, evaluated by means of Eq. (2.17), is of about 12 Å, consistent with the statistically estimated mean shortest distance between the doping ions in the lattice (10 Å). The $^5D_4$ decay curve (Fig. 6.7) presents a rise time indicating that the emitting level is fed from another state.

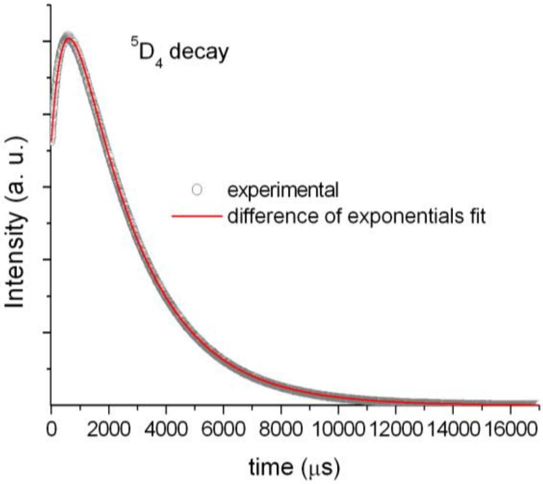

Fig. 6.7. Decay profile of the $^5D_4$ emission.

It can be fitted to a difference of two exponentials allowing the evaluation of both rise time and decay time of the emitting level. The former is of 493 μs, significantly shorter than the $^5D_3$ decay times of the isolated donor deduced from the Inokuti–Hirayama model, but consistent with the 1/*e* decay time calculated from the profile of Fig. 6.6, confirming that feeding occurs from the $^5D_3$ state. The $^5D_4$ decay time is of 2.3 ms, indicating that probably the $^5D_4$ emission is scarcely affected by non radiative processes.

YPO_4:Tb^{3+}, Bi^{3+} co-doped phosphors

The emission properties along the SG*x* and SS*x* series have been summarized in Fig. 6.8 and Fig. 6.9, respectively.

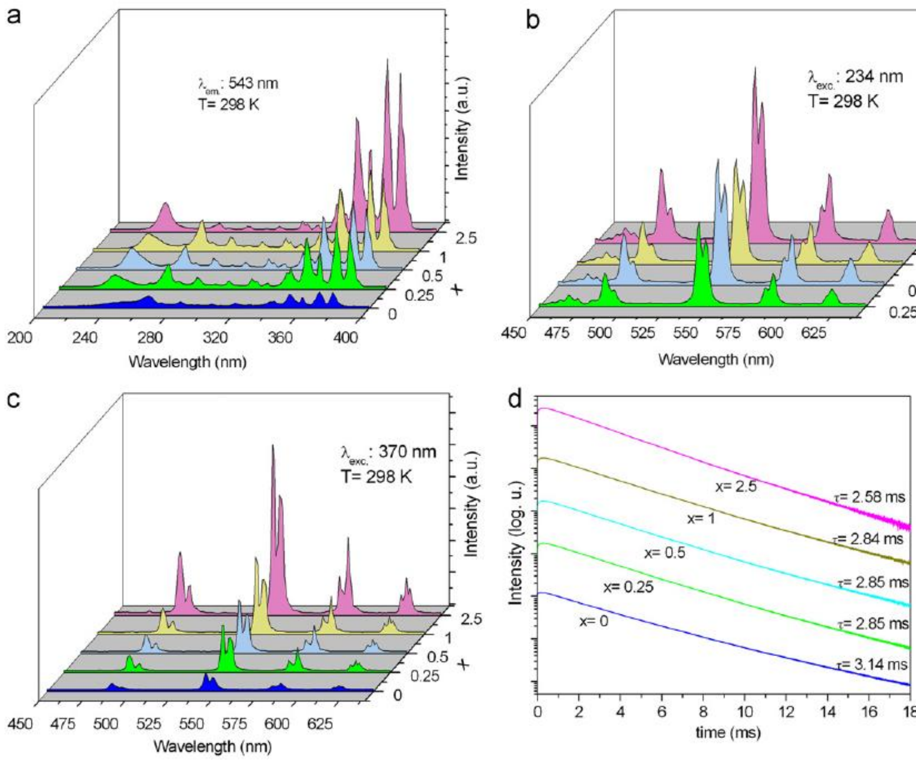

Fig. 6.8. Emission spectroscopy along the SGx series. (a) excitation; (b) emission upon 234 nm excitation; (c) emission upon 370 nm excitation; (d) decay profiles ($\lambda_{exc.}$: 355 nm, λem.: 543 nm).

The spectra have similar structures and the assignment of the observed features is straightforward. The excitation spectra (Figs. 6.8a and 6.9a) present a broad transition with maximum at 236 nm, that is absent in the singly Tb^{3+}-doped samples. It can be assigned to the $^1S_0 \rightarrow {}^3P_1$ absorption transition of Bi^{3+}[8]. The weaker band peaking at 267 nm is ascribed to a spin forbidden *f–d* transition of Tb^{3+}[9]. The remaining transitions at longer wavelengths pertain to transitions from the $^7F_6$ ground state to the excited levels of the $4f^8$ configuration.

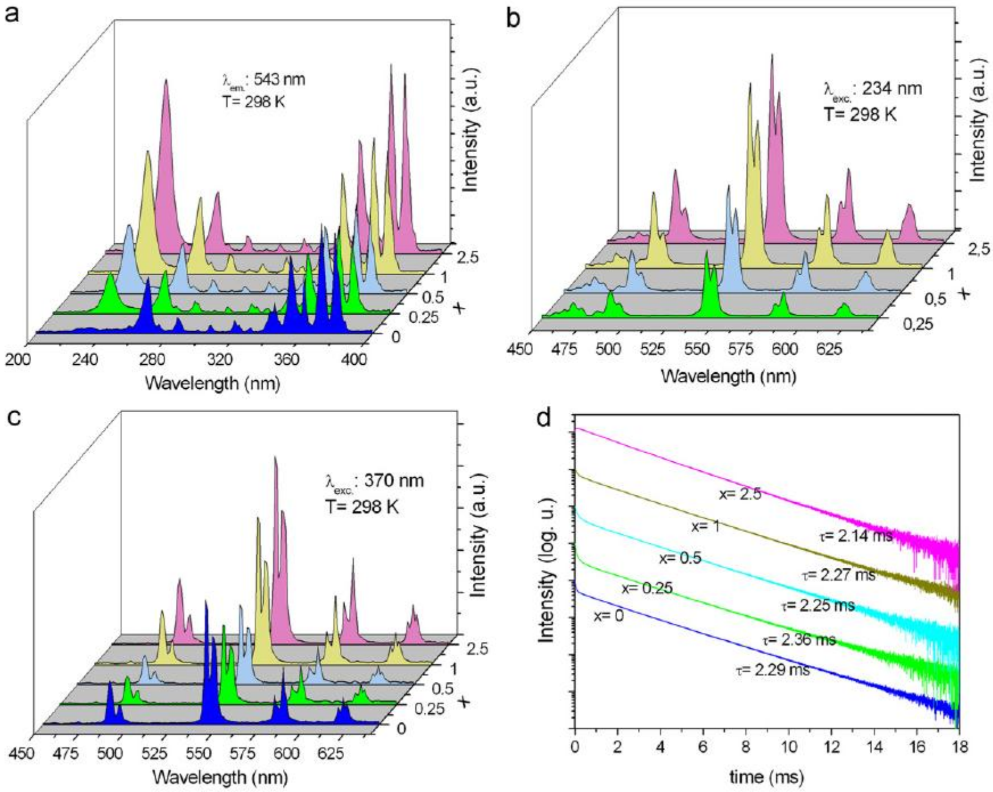

Fig. 6.9. Emission spectroscopy along the SSx series. (a) excitation; (b) emission upon 234 nm excitation; (c) emission upon 370 nm excitation; (d) decay profiles ($\lambda_{exc.}$: 355 nm, $\lambda_{em.}$: 543 nm).

The most intense lines with maxima at 370 and 378 nm can be assigned to the $^7F_6 \rightarrow ({}^5G_6, {}^5G_5, {}^5L_9)$ and $^7F_6 \rightarrow ({}^5D_3, {}^5L_{10})$ on the basis of the energy levels scheme of Tb^{3+}[10]. The emission transitions have already been assigned in the previous section. The effect of the Bi^{3+} co-doping is evident in both excitation and emission spectra. In the case of the SG*x* samples (Fig. 6.8a–c) it can be summarized as follows:

- The presence of the excitation bands at 236 nm (Fig. 6.8a) indicates that a $Bi^{3+} \rightarrow Tb^{3+}$ energy transfer occurs. On the other hand, the intensity of the Bi^{3+} bands is nearly independent of the co-doping level and much lower than those of the *f–f* Tb^{3+} transitions, allowing to conclude that this mechanism is relatively inefficient. Nevertheless, it introduces a new excitation channel for the Tb^{3+} luminescence. It is interesting to note that the intensity of the *f–f* Tb^{3+} excitation transitions progressively increases with the Bi^{3+} concentration.
- As expected, the emission spectra obtained upon 234 nm excitation (Fig. 6.9b) do not vary very much with the Bi^{3+} content. In addition a residual emission from the $^5D_3$ level is observable at around 470 nm, indicating that the $Bi^{3+} \rightarrow Tb^{3+}$ energy transfer process partially interferes with the cross relaxation mechanism (1).
- These features in fact do not appear in the spectra measured upon direct excitation at 370 nm (Fig. 6.8c). These spectra are significantly more intense than the previous ones: this evident from the relative intensities of the corresponding excitation features. For the rest a direct comparison is not easy, since the adopted measurements conditions (slit width, optical filters, etc.) are different. In agreement with the excitation behavior, the intensity of the luminescence significantly increases with the Bi^{3+} concentration. The emission decay curves (Fig. 6.8d) are single exponential, with only an incipient rise times indicating strong shortening of the $^5D_3$ decay time. The values of the $^5D_4$ decay times

range from 3.14 ms for *x*=0 to 2.56 ms for *x*=2.5, indicating again that the emission probability increases with the Bi^{3+} content. These results can be visually verified by comparing the colors of the SG*x* phosphors under UV lamp illumination (365 nm). The results, shown in Fig. 6.10, are consistent with the spectroscopic observations.

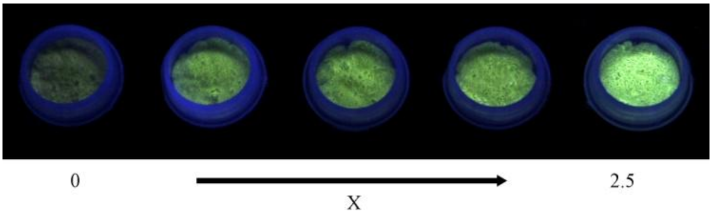

Fig. 6.10. Green emission of the SGx phosphors under 365 nm UV lamp.

The measurements carried out on the SS*x* samples (Fig. 6.9a–d) reveal some discrepancies with respect to the previous ones:

- In the excitation spectrum (Fig. 6.9a) the intensity of the Bi^{3+} band increases with the co-doping level and it is similar to that of the *f*–*f* Tb^{3+} transitions.
- The increase of the emission intensity with the Bi^{3+} concentration is less pronounced than in the SG*x* case.
- The intensity of the 370 nm excited emission of the SG*x* phosphors is significantly stronger than that of the SS*x* ones. This aspect has been evidenced in Fig. 6.11.
- The emission decay profiles (Fig. 6.9d) are again single exponential with the same trend but shorter than in the previous case. In the shortest time tail they present (with the exclusion of the SS2.5 phosphor) a faster component, likely ascribable to an incipient cross relaxation process depopulating the $^5D_4$ state.

These observations allow to infer that the effective concentration of Bi^{3+} in the SS*x* phosphors is lower than the nominal one. This can be correlated to the relatively high temperature required by the solid state synthesis (1200 °C), that evidently implies the loss of part of Bi_2O_3 by sublimation.

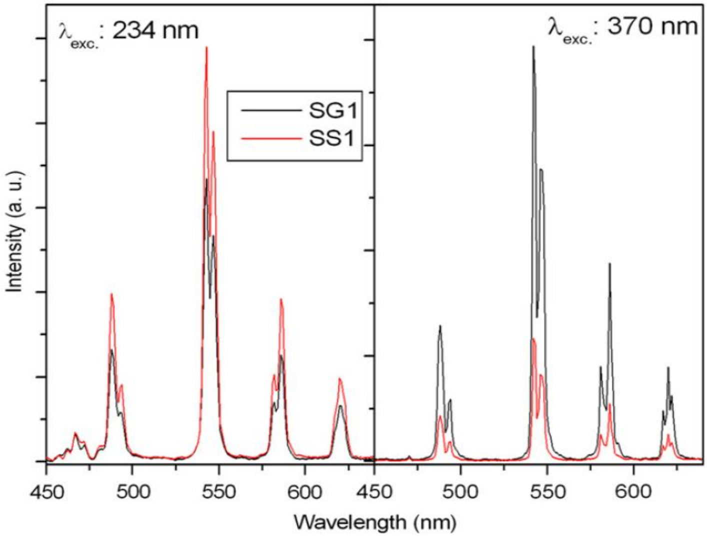

Fig. 6.11. Comparison between the relative intensities of the emission spectra of the SG1 and SS1 phosphors.

The experimental results evidence that the SG2.5 is the best performing phosphor among those investigated in this work. We have measured its 10 K spectrum and compared it with the 298 K one and with that of the single crystals. As shown in Fig. 6.12, the bandwidth does not change very much on passing from the crystals to the nano-sized phosphor. Moreover the emission intensity at room temperature is slightly higher than at low temperature, confirming the absence of thermal quenching.

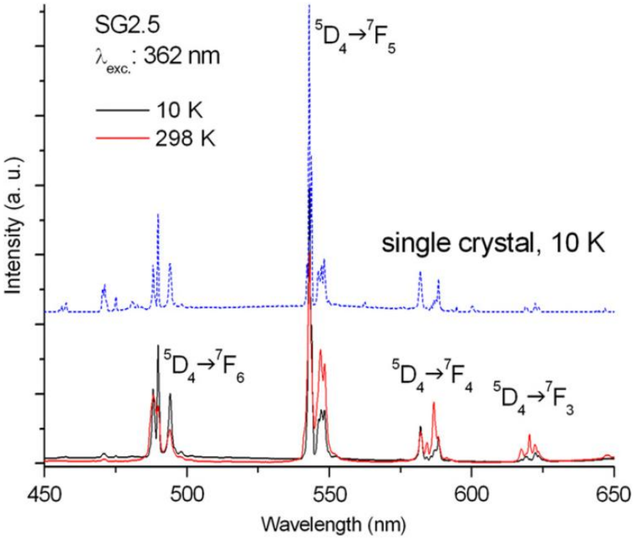

Fig. 6.12. 10 and 298 K emission spectra of the SG2.5 phosphor. The spectrum of the single crystal is shown for the sake of comparison.

6.5 YPO_4:Sm^{3+}, Bi^{3+}

The room temperature excitation and emission spectra of the $Y_{0.98-y}Sm_{0.02}Bi_yPO_4$ (y= 0, 0.005, 0.01, 0.025, 0.05) phosphors are shown in Fig. 6.13a and b respectively. The formers are composed of relatively sharp lines ascribed to transitions from the $^6H_{5/2}$ ground state of Sm^{3+} to its excited levels, namely $^6D_{5/2}$ (364 nm), $^6P_{7/2}$ (377 nm), $^4G_{11/2}$ (392 nm), $^4F_{7/2}$ (404 nm), $^6P_{5/2}$ (419 nm), $^4G_{9/2}$ (441 nm), $^4I_{13/2}$+$^4I_{11/2}$+$^4I_{19/2}$ (460–490 nm). We have also explored the 220–300 nm wavelength region in order to verify the presence of bands ascribable to $Bi^{3+}\rightarrow Sm^{3+}$ energy transfer. The 241 nm emission of YPO_4:Bi^{3+}, and consequently a possible energy transfer process involving Bi^{3+} as a sensitizer, can be in fact observed upon excitation at 230 and at 160–180 nm [8]. We did not observe any feature in the mentioned range, then we infer that the $Bi^{3+}\rightarrow Sm^{3+}$ energy transfer process is inefficient in $YPO_4:Bi^{3+},Sm^{3+}$ at ambient temperature. The emission spectra are composed of four manifolds with maxima at 562, 600, 644 and 705 nm and assigned to the $^4G_{5/2}\rightarrow{}^6H_J$ (J=11/2, 9/2, 7/2, 5/2) transitions of Sm^{3+}, respectively. The spectra of Fig. 6.13 clearly reveal that the emission intensity is enhanced as the Bi^{3+} concentration increases from 0% to 5%.

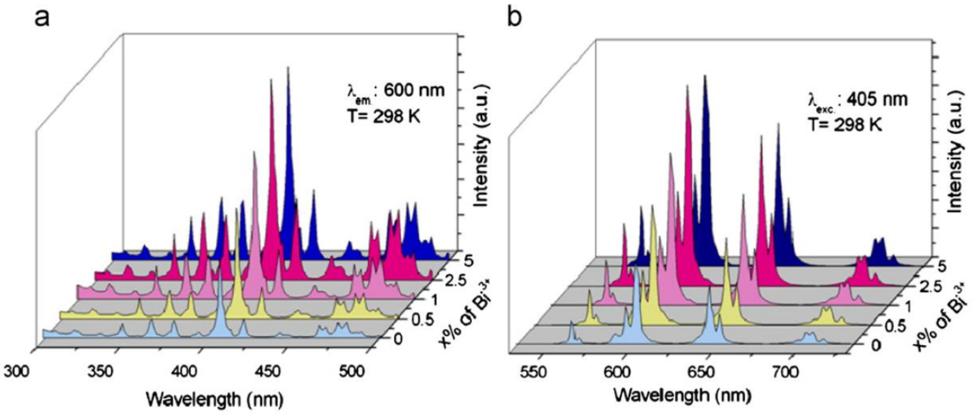

Fig. 6.13. Excitation (a) and emission (b) spectra of $Y_{0.98-x}Sm_{0.02}Bi_xPO_4$ (x=0, 0.005,0.01,0.025,0.05).

These results can be visually verified by comparing the color intensities of the studied phosphors under 365 nm UV lamp illumination. The intensity trend shown in 6.14 is well consistent with the spectroscopic observations.

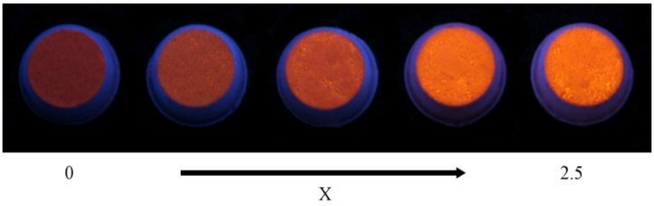

Fig. 6.14. Orange–red emission of the $Y_{0.98-x}Sm_{0.02}Bi_xPO_4$ (x=0, 0.005, 0.01, 0.025, 0.05) phosphors under 365 nm UV lamp illumination.

The decay profiles of the investigated phosphors are shown in Fig. 6.14. As observed in the case of YPO_4:Tb^{3+} single crystals they are non-exponential and can be reproduced by the Inokuti–Hirayama model suitable for the energy transfer process in absence of migration.

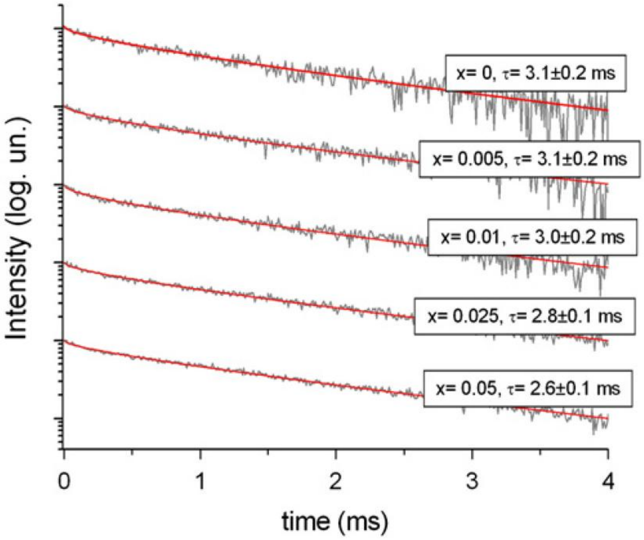

Fig. 6.15. Emission decay profiles of $Y_{0.98-x}Sm_{0.02}Bi_xPO_4$ (x=0, 0.005, 0.01, 0.025, 0.05). $\lambda_{exc.}$: 406.1 nm, $\lambda_{em.}$: 600 nm. Gray line: experimental; red line: Inokuti– Hirayama fit.

The main energy transfer process responsible of the observed behavior is the cross relaxation [11]:

$$^4G_{5/2}+{}^6H_{5/2}\rightarrow{}^6F_{11/2}+{}^6F_{5/2} \qquad (6.2)$$

The critical distance for the transfer, evaluated by means of Eq. (2.17), is of about 7.5 Å, i. e. shorter than the statistically estimated mean shortest distance between the doping ions in the lattice (9.5 Å). This could be an indication of some clustering effects. In Table 6.1 we report the (*x*, *y*) CIE coordinates, the internal quantum yields (defined as the ratio of the emitted photons to the absorbed photons) and the absorbed fraction (AF) of the

405 nm incident radiation (in correspondence of the $^6H_{5/2} \rightarrow {}^4F_{7/2}$ transition) of the investigated samples.

Table 6.1. Color coordinates, internal quantum yields (IQY) and absorbed fraction (AF) of the 405 nm incident radiation of $Y_{0.98-x}Sm_{0.02}Bi_xPO_4$ (x=0, 0.005, 0.01, 0.025, 0.05).

x	**Color coordinate (x,y)**	**IQY**	**AF**
0	0.585, 0.375	0.037	0.338
0.005	0.563, 0.364	0.080	0.244
0.01	0.584, 0.376	0.157	0.189
0.025	0.588, 0.377	0.300	0.194
0.05	0.589, 0.379	0.381	0.177

The AF parameter is important in the evaluation of the emission performance as it depends on the radiative absorption probability and on the morphological characteristics of the sample. The values of the quantum yield quantitatively account for the observed emission behavior. As expected, the presence of Bi^{3+} does not significantly affect the color of the emission, that is located in the red–orange region (Fig. 6.16).

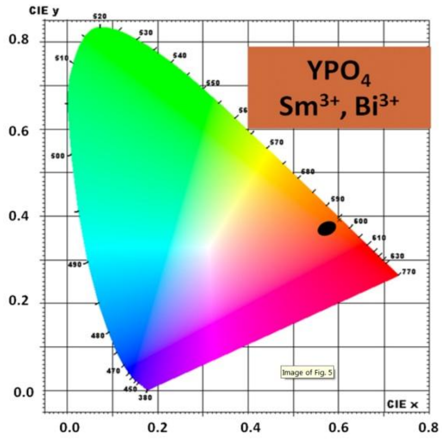

Fig. 6.16. Chromaticity diagram of the investigated phosphors. The dominant wavelength is 596 nm.

6.6 $YPO_4:Eu^{3+}, Bi^{3+}$ and $YPO_4:Nd^{3+}, Bi^{3+}$

In order to further confirm the enhancing effect of bismuth co-doping on the luminescence properties of YPO_4 activated with rare earth ions, we have extended the investigation to samples doped with europium or neodymium. The room temperature excitation and emission spectra of $YPO_4:Eu^{3+}$ and $YPO_4:Eu^{3+}, Bi^{3+}$ are shown in Fig. 6.17a and b respectively.

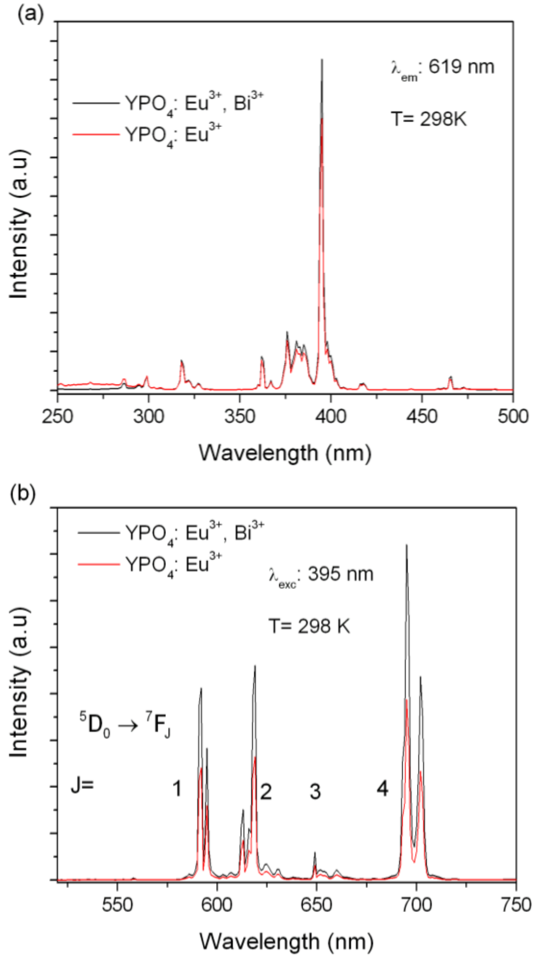

Fig. 6.17. Excitation (a) and emission (b) spectra of $Y_{0.98-x}Eu_{0.02}Bi_xPO_4$ (x=0, 0.025).

The excitation spectrum is composed of sharp lines ascribed to transitions from the $^7F_0$ ground state to the excited levels of the $4f^6$ electronic configuration of Eu^{3+}. The most intense feature is located at 395 nm and it is assigned to the $^7F_0 \rightarrow ^5L_6$ transition. The emission spectra are composed of four manifolds with maxima at 592, 619, 649, 695 nm and assigned to the $^5D_0 \rightarrow ^7F_J$ (J=1, 2, 3, 4) transitions of Eu^{3+} respectively. The intensity ratio between the $^5D_0 \rightarrow ^7F_2$ and the $^5D_0 \rightarrow ^7F_1$ emission manifold is lower than that reported for other phosphors like, for instance, $YVO_4:Eu^{3+}$ [12]. This is related to the fact that the $^5D_0 \rightarrow ^7F_2$ transition is hypersensitive, then its intensity strongly depends on the host, whereas the $^5D_0 \rightarrow ^7F_1$ is a magnetic dipole transition, relatively independent on the environment. The observed behavior is consistent with a relatively low value of the Ω_2 intensity parameter, in analogy with the $YPO_4:Dy^{3+}$ case discussed in Sect. 4. The spectra of Fig. 6.17 confirm the Bi^{3+}effect of the luminescence properties: the emission intensity is stronger in the case of co-doped material. We have finally carried out a preliminary study on $YPO_4:Nd^{3+}$, in order to verify the effectiveness of the Bi^{3+} co-doping in the case of a NIR emitting material, in the perspective to extend the investigations to materials of interest for laser applications. The emission spectra of $YPO_4:Nd^{3+}$ and $YPO_4:Nd^{3+}$, Bi^{3+} are presented in Fig. 6.18a, the luminescence decay profiles in Fig. 6.18b. The emission spectrum is composed of three manifolds at 890, 1060 and 1340 nm, assigned to the $^4F_{9/2} \rightarrow ^4I_J$ (J= 9/2, 11/2, 13/2) transitions respectively. The effect of the bismuth is not so evident as in the previous cases, even if an increment of the emission intensity with the co-doping can be appreciated.

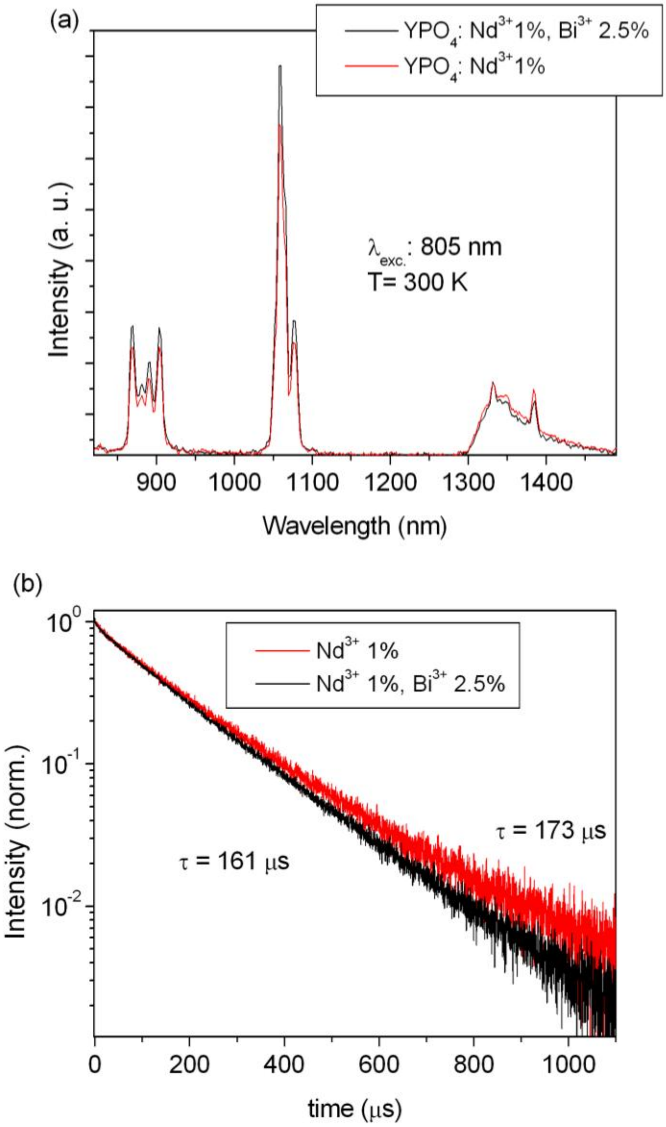

Fig. 6.18. Emission spectra (a) and decay profiles (b) of $Y_{0.98-x}Nd_{0.02}Bi_xPO_4$ (x=0, 0.025).

The decay profiles are nearly single exponential: the decay time of the co-doped material is slightly shorter, confirming that the allowance degree of the emission transition is higher than in the singly doped phosphor.

6.7 Conclusions

In $YPO_4:Tb^{3+}$ the co-doping with Bi^{3+} induces the appearing of an additional excitation channel at 234 nm arising from the $Bi^{3+}\rightarrow Tb^{3+}$ energy transfer. This is a resonant process, since the overlap integral between the Bi^{3+} emission (constituted of a sharp band peaking at 245 nm and of a very weak broadband extending to about 370 nm [8]) and the Tb^{3+} excitation features is nonzero. Its value however is not very high, and this accounts for its relatively low efficiency. The emission spectra recorded upon direct excitation at 370 nm in the Tb^{3+} absorption band (Figs. 6.8c and 6.9c) and at 405 nm in the Sm^{3+} absorption band (Fig. 6.13b) as well as the comparative measurements carried out upon 365 nm UV lamp illumination (Fig. 6.10 and 6.14) evidence that the intensity of the Tb^{3+} and Sm^{3+} luminescence significantly increases as the Bi^{3+} concentration increases (within the considered range). Preliminary measurements on Eu^{3+}- and Nd^{3+}- doped YPO_4 have provided further confirmations of this effect, that cannot be ascribed to direct interactions between doping and co-doping ions. Since the efficiency of the non-radiative processes cannot vary along the considered series (it depends on the activator concentration, that is constant), we have considered the possibility that the presence of Bi^{3+} could induce an increase of the radiative emission probabilities through an alteration of some host properties. In particular, it is known that the refractive index of several glasses and crystals tends to increase when these are doped with Bi^{3+}[13, 14]. This influences the probabilities of the radiative transitions, whose dependence on the refractive index is in general expressed in terms of ‘local field correction’ and indicated with E_{loc}/E_0. For what concerns an electric dipole allowed emission transition [15]:

$$A = \frac{1}{4\pi\varepsilon_0} \frac{4n\omega_0^3}{3\hbar c_0^3} \left(\frac{E_{loc}}{E_0} \right)^2 |\mu|^2 \qquad (6.3)$$

where A is the spontaneous emission probability, ε_0 the permittivity of vacuum, ω_0 the transition frequency, $\hbar$ the reduced Planck's constant, n the refractive index, c_0 the light speed, $|\mu|^2$ the square of the matrix element of the transition. The local field correction is often approximated as:

$$\frac{E_{loc}}{E_0} = \frac{n^2 + 2}{3} \qquad (6.4)$$

The spontaneous emission probability then increases as the refractive index increases. The individual contribution of a single ion to the value of the refractive index can be estimated using the modified form of the Lorenz–Lorentz equation proposed by Korotkov et al. [16]:

$$\frac{n^2 - 1}{n^2 + 2} \frac{1}{\rho} = \frac{\sum l_i r_i}{M} \qquad (6.5)$$

where n is the refractive index, ρ the density of the crystal, l_i the number of atoms of the selected element in the nominal chemical formula and r_i is the ionic refraction and M is the molar mass of the compound. The ionic refraction of Bi^{3+} is much higher than that of Y^{3+} (10.1 against 3.2 [16]), then the substitution of the latter with the former induces an increase of the refractive index of the host material and consequently of the spontaneous emission transition probability. The progressive shortening of the decay time with the Bi^{3+} concentration is consistent with this hypothesis.

In $YPO_4:Tb^{3+}$, the decay time of the samples synthesized by sol-gel are generally longer than those obtained by solid state reaction and of the single crystals. We suppose that this is related to a lower defectivity of the crystalline grains in the former case, that reduces the probability of the excitation migration towards quenching centers. In conclusion, we have firstly investigated the emission properties of $YPO_4:Tb^{3+}$ in form of single crystals in order to obtain information about its fluorescence dynamics, then we have extended the study to singly and Bi^{3+}-co-doped nano/micro-sized materials obtained by sol–gel synthesis and solid state reaction. We have demonstrated the beneficial effect of Bi^{3+} co-doping, at concentration up to about 5%, on the emission performance of $YPO_4:Sm^{3+}$ and $YPO_4:Tb^{3+}$, provided an explanation for this behavior and confirmed this results with preliminary studies on YPO_4 activated with Eu and Nd.

References

[1] G. Blasse, A. Bril., J. Chem. Phys. 47 (1967) 1920.

[2] H. Lai, A. Bao, Y. Yang, Y. Tao, H. Yang, Y. Zhang, L. Han, J. Chem. Phys. C 112 (2008) 282.

[15 Tb] S.H. Smith, B.M. Wanklyn, J. Cryst. Growth 21 (1974) 23.

[16] W.O. Milligan, D.F. Mullica, G.W. Beall, L.A. Boatner, Inorg. Chim. Acta 60 (1982) 39.

[5] T. Aldred, Acta Cryst. B 40 (1984) 569.

[6] K. Momma, F. Izumi, J. Appl., Crystallogr 41 (2008) 653.

[7] M. Inokuti, F. Hirayama, J. Chem. Phys. 43 (1965) 1978.

[8] T. Jűstel, P. Huppertz, W. Mayr, D.U. Wiechert, J. Lumin. 106 (2004) 225.

[9] E. Nakazawa, J. Lumin. 100 (2002) 89.

[10] K.S. Thomas, S. Singh, G.H. Dieke, J. Chem. Phys. 38 (1963) 2180.

[11] T. Luxbacher, H.P. Fritzer, C.D. Flint, J. Lumin. 71 (1997) 313.

[12] L. Chen, Y. Liu, K. Huang, Mat. Res. Bull. 41 (2006) 158.

[13] P. Becker, Cryst. Res. Technol. 38 (2003) 74.

[14] H. Moriceau, B. Ferrand, M.F. Armand, M. Olivier, D. Challeton, J. Daval, IEEE Trans. Mag. 20 (1984) 1004.

[15] J. García Solé , L.E. Bausá, D. Jaque, ‘An Introduction to the Optical Spectroscopy of Inorganic Solids’, Wiley, 2005.

[16] A.S. Korotkov, V.V. Atuchin, Opt. Commun. 281 (2008) 2132.

Chapter 7

Photoswitching of bis-spiropyran using near-infrared excited upconverting nanoparticles

7.1 Introduction

Photochromism is defined as a light induced reversible interconversion of molecules between two states with a distinct absorption signature across the ultraviolet and visible regions of the electromagnetic spectrum [1]. The main families of organic photochromic compounds include spiropyrans, spirooxanines, diarylethenes, azobezenes, and fulgides [2]. These photochromic molecules are widely studied for their potential applications in molecular electronic and photonic devices [3,4]. In this context, one of the most widely studied organic photochromic families, spiropyrans, have attracted a great deal of attention for biological applications in recent years [5]. The spiropyran molecule has two isomers, the ring-closed spiropyran form and the ring-opened merocyanine form. Irradiation of the colorless spiropyran form with UV-light not exceeding 450 nm produces the colored merocyanine form, which has a strong absorption in the visible and can be reversed by exposing it to yellow light. Upon UV irradiation, the C–O spiro bond is cleaved heterolytically and the spiro carbon, which is sp^3-hybridized becomes sp^2-hybridized producing a delocalized pi-system in the merocyanine form that is capable to absorb light in the visible region. Andersson *et al.* showed that the ring-open form exhibited a strong affinity with DNA by intercalation, whereas the ring-closed spiropyran had little or no affinity for DNA [6]. Thus, by photoswitching between the two forms, spiropyran can be used to modulate the behaviour of DNA [6]. In addition, a number of fluorophore-spiropyran hybrid systems have also been recently reported in the literature and spiropyrans have also been hybridized with quantum dots (QDs) to modulate their fluorescence emission [7]. However, for the biological applications of spiropyrans, direct irradiation of UV light was needed to trigger the isomerisation transformation. Excitation with high-energy UV light source obviously limits their use in biological applications due to its low tissue penetration depth, potential for photodamage and autofluorescence in biological specimens where chromophores are present [8].

Lanthanide-doped upconverting nanoparticles (UCNPs) have been intensively studied in recent years [9]. These nanoparticles can emit UV, visible and/or near-infrared (NIR) light upon NIR excitation (typically 980 nm) *via* a multiphoton process known as upconversion [10]. It has been recently synthesized Tm^{3+}/Yb^{3+}-doped $LiYF_4$ UCNPs *via* the thermal decomposition method, which showed stronger UV emission following NIR excitation with 980 nm light compared to $NaYF_4$ [11]. Taking advantage of the high penetration depth, reduced photodamage, and minimal autofluorescence of the NIR excitation light, these UCNPs could be used as biocompatible UV sources in biological applications. Incorporating spiropyrans with UCNPs could achieve the photochromic transformation of spiropyran upon NIR excitation through fluorescence resonance energy transfer (FRET) process.

In this Section we report on the functionalization of $LiYF_4{:}Tm^{3+}$, Yb^{3+} UCNPs with bis-spiropyran to demonstrate the photoswitching of this molecule using the UV light obtained after NIR excitation of the nanoparticles. We also carry out a kinetic study of the photoswitching and report on the energy transfer efficiency between the UCNPs and the ring-closed bis-spiropyran as well as the photodegradation of the bis-spiropyran functionalized UCNPs (BSP-UCNPs).

7.2 Experimental

Synthesis of $LiYF_4$:Tm^{3+}, Yb^{3+} (UCNPs).

Synthesis of $LiYF_4$:Tm^{3+}, Yb^{3+} (UCNPs). Thulium oxide (Tm_2O_3, 99.99+ %), ytterbium oxide (Yb_2O_3, 99.99%), yttrium oxide (Y_2O_3, 99.99+ %), triflouroacetic acid (CF_3COOH, 99%), lithium trifluoroacetate (CF_3COOLi, 98%), oleic acid (technical grade, 90%), and 1-octadecene (technical grade, 90%) were all purchased from Sigma-Aldrich and were used without further purification. $LiYF_4$:Tm^{3+}, Yb^{3+} UCNPs were synthesized via the thermal decomposition method previously, which was comprised of a two-step process. In the first step, a 10 mL mixture of water/trifluoroacetic acid (1:1) was added to a round-bottom flask containing 6.25×10^{-6} mol of Tm_2O_3 (0.0024 g, 0.5 mol % Tm^{3+}), 3.13×10^{-4} mol of Yb_2O_3 (0.1232 g, 25 mol % Yb^{3+}), and 9.31×10^{-4} mol of Y_2O_3 (0.2103 g), and the cloudy solution was heated to reflux at 80 °C until it was clear. The resulting solution was then dried at 60 °C to form the trifluoroacetate lanthanide precursors. In the second step, 12.5 mL of oleic acid and 12.5 mL of 1-octadecene were added to a 3-neck round bottom flask (solution A) and degassed at 150 °C for 30 min, and then maintained at the same temperature under argon atmosphere. Approximately 2.50×10^{-3} mol (0.2999 g) of CF_3COOLi was added to the dried precursor solids along with 7.5 mL of oleic acid and 7.5 mL of 1-octadecene (solution B), the resulting solution was degassed at 45 °C, 75 °C, and 125 °C for 5 min, respectively. Meanwhile, solution A was heated to

315 °C. At this moment, solution B was injected into solution using a syringe and pump system at a rate of 1.5 mL/min (Harvard Apparatus Econoflow). The reaction mixture was left to stir vigorously for 90 min under Ar gas. After cooling down to room temperature, absolute ethanol was added to the reaction solution to precipitate UCNPs, which were subsequently isolated via centrifugation (3000 rpm, 15 min). The pellets were washed with a 1:3 hexane/ethanol mixture twice to remove any impurities.

Synthesis of Bis-Spiropyran

1-(2-Hydroxyethyl)-3,3-dimethylindolino-6'-nitrobenzopyrylospiran (200 mg, 0.57 mmol) and Ethylenediaminetetraacetic dianhydride (73 mg, 0.285 mmol) were dissolved in 5 mL of anhydrous DMF in an inert atmosphere. The solution mixture was heated to 80 °C for 24 h. Subsequently, the solution was allowed to cool to room temperature and water was added to precipitate the molecule, which was subsequently isolated by filtration and dried under vacuum. The target molecule was obtained as a pinkish solid with a 80 % yield.

Ligand Exchange Reaction with Bis-Spiropyran

UCNPs conjugated with bis-spiropyran (BSP-UCNPs) were synthesized by a ligand exchange reaction between oleate-capped UCNPs ($LiYF_4:Tm^{3+}$, Yb^{3+}) and bis-spiropyran. Typically, 100 mg of UCNPs were dispersed in 5 mL tetrahydrofuran (THF) followed by the addition of 10 mg of bis-spiropyran in 1 mL of THF. The mixture was stirred at room temperature for 48 h and the resulting solution was subsequently centrifuged at 3000 rpm for 15 min. After centrifugation the clear supernatant was eliminated and the pellet was re-dispersed with THF and washed twice. Free unbound bis-spiropyran molecules were removed by further centrifugations and the resulting pink deposit was subsequently dispersed in THF for use.

Fourier Transform Infrared (FTIR) Spectroscopy

FTIR spectra of the as-synthesized bis-spiropyran molecules, oleate-capped UCNPs, and the BSPUCNPs conjugate were measured on a Nicolet 6700 FTIR spectrometer by using the KBr method.

Transmission Electron Microscopy (TEM)

TEM analysis of the colloidal dispersion of UCNPs were performed using a Philips CM200 microscope operating at 200 kV equipped with a charge-coupled device (CCD) camera (Gatan). Prior to analysis, a 20 mg sample was dispersed in 2 g of toluene to yield an approximate 1 wt% solution. A few drops of the resulting solution were evaporated on a formvar/carbon film supported on a 300 mesh copper grid (3 mm in diameter).

X-Ray Powder Diffraction (XRPD)

XRPD patterns were measured using a Scintag XDS-2000 Diffractometer equipped with a Si(Li) Peltier-cooled solid state detector, Cu Kα source at a generator power of 45 kV and 40 mA, divergent beam (2 mm and 4 mm), and receiving beam slits (0.5 mm and 0.2 mm). The scan range was set from 20-80° 2θ with a step size of 0.02° and a count time of 2 s. The sample was measured using a quartz “zero background” disk.

Upconversion Luminescence Spectroscopy

The upconversion visible emission spectra of the oleate-capped UCNPs and the BSP-UCNPs were obtained upon 980 nm excitation, using a Coherent 6-pin fiber-coupled F6 series 980 nm laser diode (power of 615 mW), coupled to a 100 μm (core) fiber. For the upconversion studies, the samples (1 wt% in THF) were placed in 1 cm path-length quartz cuvettes (Hellma, QS). The upconverted visible emissions were collected at right angle with respect to the incident beam and subsequently dispersed by a 1m Jarrell-Ash Czerny-Turner double monochromator with an optical resolution of ~0.15 nm. The visible emissions were detected by a thermoelectrically cooled Hamamatsu R943-02 photomultiplier tube. A preamplifier, model SR440 Standard Research Systems, processed the photomultiplier signals and a gated photon counter model SR400 Standard Research Systems data acquisition system was used as an interface between the computer and the spectroscopic hardware. The signal was recorded under computer control using the Standard Research Systems SR465 software data acquisition/analyzer system. The UV emissions were collected using a Spex Minimate ¼ m monochromator and detected with an Oriel 70680 photomultiplier tube. It should be noted that while the UV and visible emissions are measured with different detectors, they do in fact have overlapping wavelengths in the blue region. Thus, by measuring the overlapping regions with both monochromators, under identical conditions, the intensity of the UV emissions could be compared to the visible ones.

UV-visible absorption measurement

UV-visible absorption spectra of bis-spiropyran and BSP-UCNPs in THF solvent were recorded using Varian (Mulgrave, Victoria, Australia) Cary 5 and 5000 spectrophotometers.

7.3 Results and discussion

Structural data and morphology

The oleate-capped LiYF$_4$:Tm$^{3+,}$Yb^{3+} UCNPs prepared *via* the thermal decomposition method show a diamond-like morphology (Fig. 7.1a) and are approximately 89 nm along the long axis with a narrow particle size distribution (Fig. 7.1b).

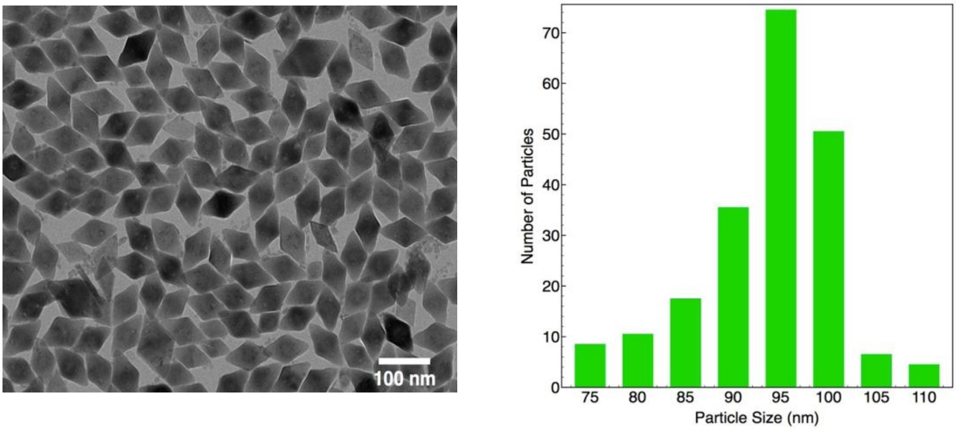

Fig 7.1 Transmission electron microscopy image of oleate-capped UCNPs (a). Particle size distribution of the oleate-capped LiYF$_4$:Tm^{3+}, Yb^{3+} UCNPs obtained from the long axis (b).

XRPD analysis showed the highly crystalline nature of the material and confirmed the tetragonal structure of the LiYF$_4$:Tm^{3+},Yb^{3+} UCNPs (Fig. 7.2).

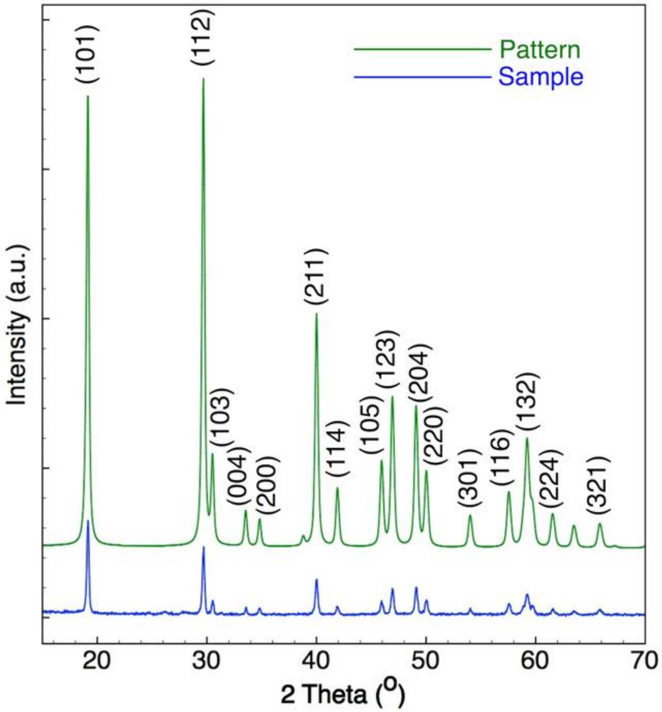

Fig. 7.2 Experimental (blue) and standard (green) X-ray diffraction patterns for the (0.5 mol%) Tm^{3+} and (25 mol%) Yb^{3+} co-doped $LiYF_4$ nanoparticles.

Photoluminescence and ligand exchange process

The upconversion luminescence spectrum upon irradiation with 980 nm light showed that the UCNPs emit strong UV light centered at 353 nm and 368 nm, which corresponds to the $^3P_0 \rightarrow {}^3F_4$ and $^1D_2 \rightarrow {}^3H_6$ transitions from the Tm^{3+} ions, respectively (in Fig. 7.3). In order to achieve the transformation from ring-closed bis-spiropyran form to the ring-open merocyanine form via the upconverted UV emission of UCNPs, grafting the bis-spiropyran molecules onto the surface of the nanoparticles is imperative since it will enhance the energy transfer efficiency. The bis-spiropyran molecules will be sensitized via FRET, which is distance dependent. Thus, the spatial separation between donor (UCNPs) and acceptor molecules (bis-spiropyran) should be small enough to favor efficient non-radiative transfer.

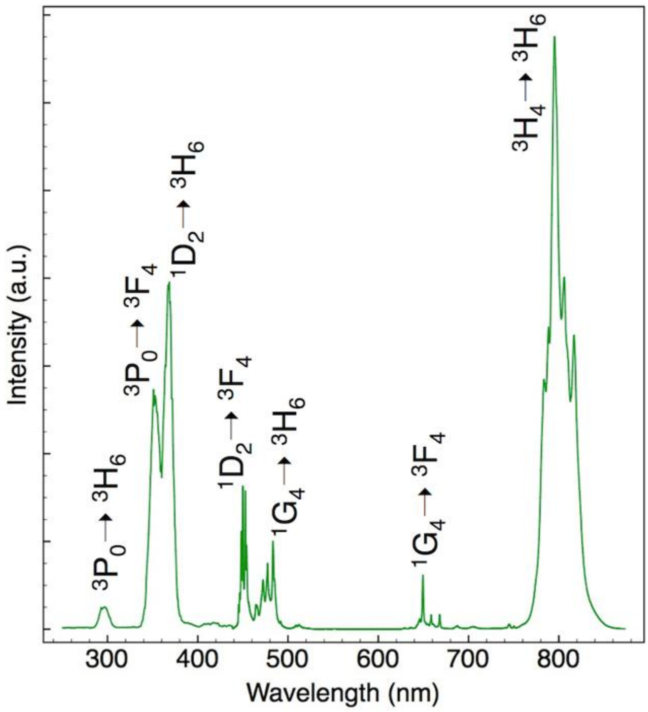

Fig. 7.3 Upconversion luminescence spectrum of oleate-capped $LiYF_4$:Tm^{3+}, Yb^{3+} UCNPs in toluene following 980 nm excitation.

In addition, the absorption peak of the ring-closed bis-spiropyran overlaps with the UV emission of the $LiYF_4$:Tm^{3+}, Yb^{3+} UCNPs centered at 353 nm and 368 nm from the $^3P_0 \rightarrow {}^3F_4$ and $^1D_2 \rightarrow {}^3H_6$ transitions of the Tm^{3+} ions, respectively (Fig. 7.4).

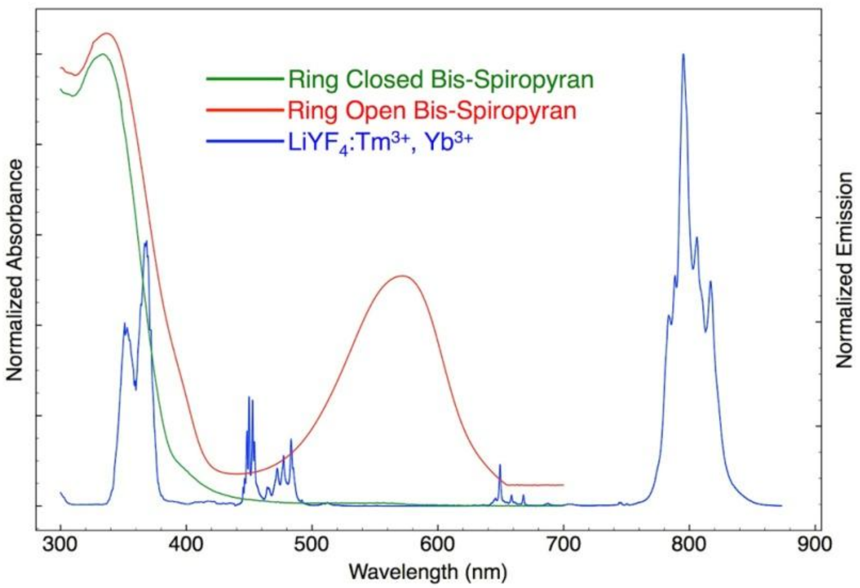

Fig. 7.4 Absorption spectra of ring-closed spiropyran (green line) and ring-open merocyanine (red line) in THF solvent. The bis-spiropyran to bis-merocyanine transformation was achieved by irradiation at 365 nm. The blue curve represents the upconverting emission spectrum of LiYF$_4$:Tm^{3+}, Yb^{3+} UCNPs (excited at 980 nm) demonstrating the overlap of absorption and emission spectra.

This yields the possibility of using the UCNPs as a UV source to trigger the bis-spiropyran → bis-merocyanine transformation. Thus, by grafting these photochromic compounds onto the surface of the UCNPs via a ligand exchange process, we were able to generate the BSP-UCNP conjugate system (Fig. 7.5). To confirm the success of the ligand exchange process between the oleate capping ligand and the bis-spiropyran, we used FTIR spectroscopy to identify the functional groups before and after ligand exchange.

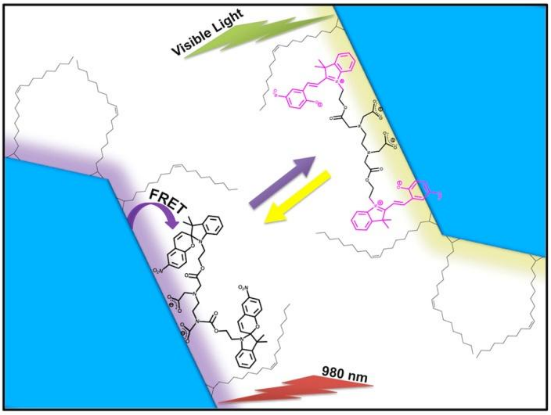

Fig. 7.5 Molecular structures of the ring-closed and ring-open isomers of the bis-spiropyran and the photoinduced isomerization. The schematic of photoswitching of bis-spiropyran in the BSP-UCNPs system is presented.

By comparing the fingerprint region of the FTIR spectra between BSP-UCNPs (blue line) and bis-spiropyran (green line), it clearly shows that bis-spiropyran was successfully grafted on the surface of the UCNPs (Fig. 7.6).

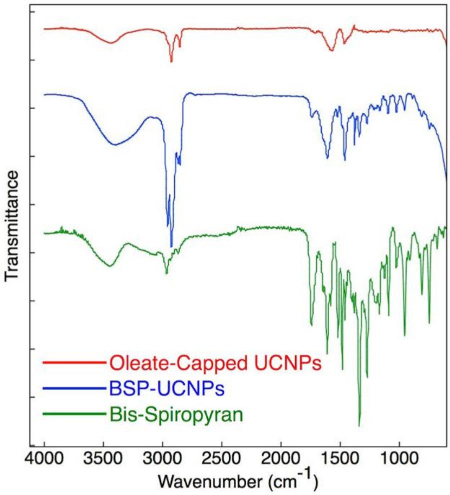

Fig. 7.6 Fourier transform infrared spectra of oleate-capped UCNPs (red line); BSP-UCNPs (blue line); and bis-spiropyran (green line).

However, comparison of the spectra of oleate-capped UCNPs (red line) and BSP-UCNPs (blue line) makes it difficult to conclude that the oleate is completely removed as some of the characteristic peaks attributed to the oleate such as carboxylate symmetric stretching (at 1568 cm^{-1}) and asymmetric stretching (at 1468 cm^{-1}) are still present in the BSP-UCNPs spectrum. Thus, we concluded that the oleate capping ligands on the surface of the UCNPs were not completely exchanged by bis-spiropyran. It should also be noted that the ratio between the peaks at 1744 cm^{-1} (corresponding to –COOH) and 1690 cm^{-1} (corresponding to COO–) in the spectrum of BSP-UCNPs decreased dramatically, compared to the spectrum of bis-spiropyran. This is indicative that some carboxylic groups were converted into carboxylate groups after ligand exchange demonstrating that the bis-spiropyran molecule was in fact grafted on to the surface of the UCNPs through carboxylate groups [10].

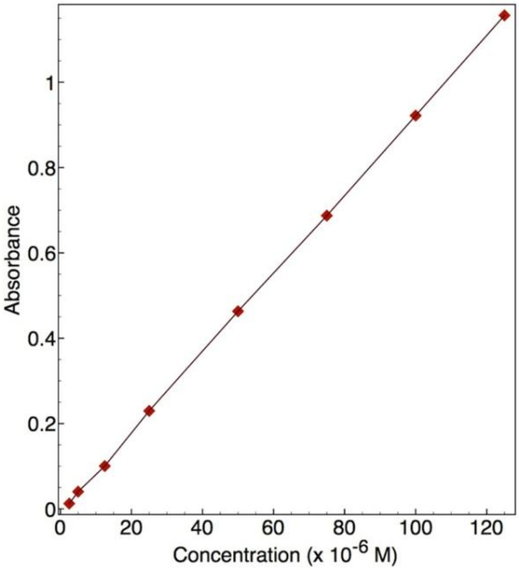

Fig. 7.7 Calibration curve of bis-spiropyran in THF (absorbance at 333 nm).

To determine the concentration of bis-spiropyran on the surface of the UCNPs, we measured its absorbance in THF at 333 nm and established a calibration curve. Using this curve and the absorbance value obtained for a sample of 0.2 wt% BSP-UCNPs, we found the concentration of bis-spiropyran on the nanoparticles to be 6.8×10^{-5} M (see Fig. 7.7), which represents approximately 220 molecules of bis-spiropyran on the surface of the UCNPs. Fig. 7.8 shows the upconversion spectra of oleate-capped UCNPs (0.2 wt% in THF), BSP-UCNPs (0.2 wt% in THF) and a solution of 0.2 wt% oleate-capped UCNPs plus 6.8×10^{-5} M of bis-spiropyran in THF. We observe a significant difference in the intensity of the UV peaks centered at 353 and 368 nm of the BSP-UCNPs (bis-spiropyran functionalized on the UCNPs) in comparison to the respective peaks for the oleate-capped UCNPs and the solution of oleate-capped UCNPs and bis-spiropyran.

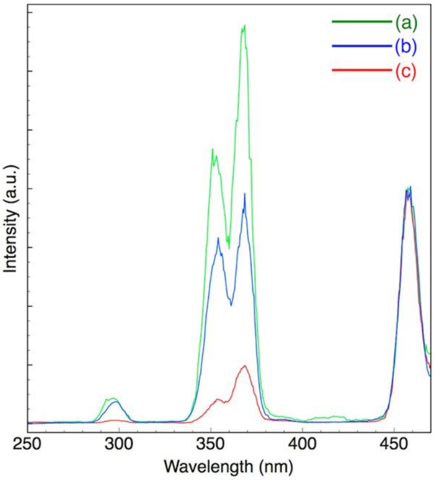

Fig. 7.8 Upconverted emission spectra following excitation at 980 nm demonstrating the quenching of the UV emission through a FRET process to bis-spiropyran; (a) Oleate-capped UCNPs (0.2 wt% in THF); (b) Simple mixture consisting of 0.2 wt% oleate-capped UCNPs and 6.8×10^{-5}Mof bis-spiropyran in THF; (c) BSP-UCNPs (0.2 wt% in THF).

This provides evidence of a possible non-radiative energy transfer from the UCNPs to the bis-spiropyran. Subsequently, the energy transfer efficiency was calculated using the following equation [12]

$$E = 1 - (I_1/I_2) \qquad (7.1)$$

where E is the energy transfer efficiency, I_1 is the intensity of BSP-UCNPs or the mixture of oleate capped UCNPs plus BSP sample at 368 nm, and I_2 is the intensity of oleate-capped UCNPs at 368 nm. The calculated energy transfer efficiency for the BSP-UCNPs was determined to be 81% whereas for the solution (oleate-capped UCNPs plus bis-spiropyran), the energy transfer efficiency was calculated to be 42%. These results confirm that the distance separating the bis-spiropyran molecules on the UCNPs in the bis-spiropyran functionalized UCNPs system is far smaller than that of the solution of the oleate-capped UCNPs and bis-spiropyran, in which the bis-spiropyran molecules are moving randomly in the solution. This suggests that the bis-spiropyan molecules in BSP-UCNP system are indeed capping the surface of the UCNPs and readily undergo an efficient FRET process.

Kinetic and stability of the system

Kinetic studies were performed in order to evaluate the effect that the functionalization of bis-spiropyran on the UCNPs has on the ring opening kinetics of the bis-spiropyran, which is known to be first order [13]. This involved irradiation of a 50 μL solution of 1 wt% BSP-UCNPs in THF under NIR excitation (980 nm) and recording the absorbance value of the bis-merocyanine at $\lambda_{max} = 570$ nm at intervals of 30 s (in the range of 0–240 s) (Fig. 7.9)

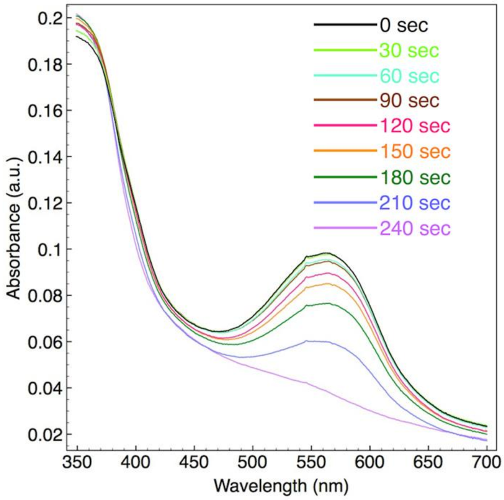

Fig. 7.9 UV-Vis absorption spectra of BSP-UCNPs (1 wt% in THF, 50 mL) after irradiation with 980 nm laser light at 30 s intervals.

This allowed us to calculate the rate constant of the bis-spiropyran to bis-merocyanine transformation (see Fig. 7.10a and b)

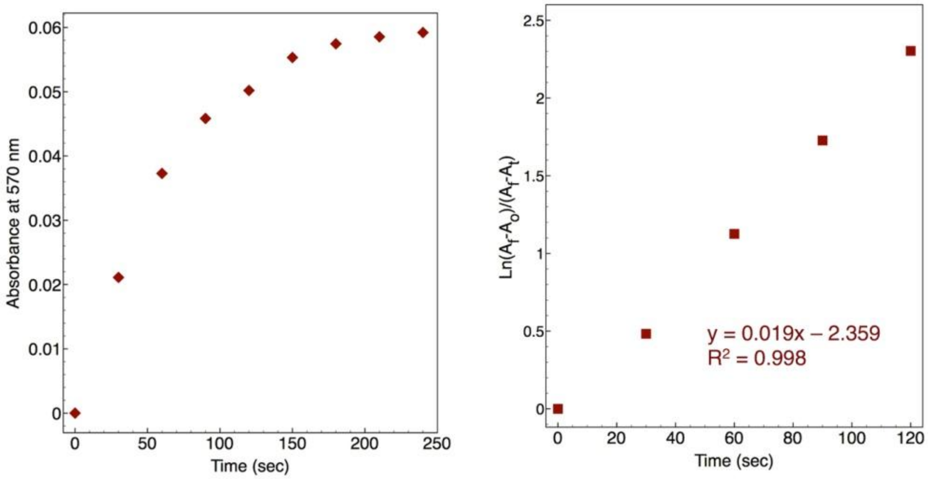

Fig. 7.10 (a) Kinetic curve of BSP-UCNPs following 980 nm laser irradiation (at 570 nm). (b) Reaction order determination *A*0, *A*t and *A*f: absorbance at *t* = 0, *t*, infinite time, respectively.

using the following equation [14]:

$$Ln\left(\frac{A_f - A_0}{A_f - A_t}\right) = Kt \qquad (7.2)$$

where: A_f is the absorbance at infinite time, A_0 is the absorbance at $t = 0$, and A_t is the absorbance following 980 nm irradiation at every interval; k is the rate constant, and t is the irradiation time. Our results show that ring-closed to ring-open isomerisation reaction follows first order kinetics with a rate constant $k = 1.9\times10^{-2}$ s^{-1} which is in good agreement with the values reported for the conversion of spiropyran to merocyanine in non-polar solvents (Fig.7.10b). The results show that the ring opening is fast and with a $t_{1/2}$ = 53s for the conversion of bis-spiropyran to bis-merocyanine on the UCNPs using NIR light irradiation.

Photodegradation of many organic photochromic molecules is a well known phenomenon which occurs when these molecules are repeatedly switched between two forms, using UV radiation, over a certain number of times (cycles). To investigate the photostability we monitored the absorbance of the peak at 580 nm while continuously switching between the BSP-UCNPs and bis-merocyanine-UCNPs (BMC-UCNPs). Fig. 7.11a shows the absorbance measured at 570 nm for the cyclical switching between BSP-UCNPs and BMC-UCNPs when exposed to 365 nm light for 30 s followed by irradiation with visible light for 30 s. Fig. 7.11b shows the results obtained when using 980 nm excitation followed by visible irradiation. As shown in Fig. 7.11a, b switching with UV and visible light is reversible and does not adversely affect the efficiency of the switching.

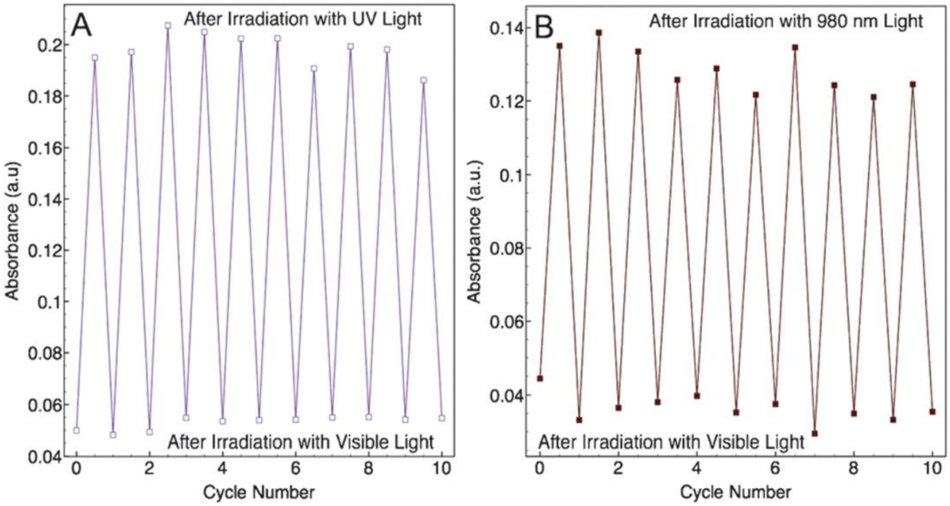

Fig. 7.11 (a) Irradiation cycles of BSP-UCNPs (1 wt% in THF) under alternate UV (365 nm; 30 s) and visible (30 s) light irradiation. (b) Irradiation cycles of BSP-UCNPs (1 wt% in THF) under alternate 980 nm (3 min.) and visible (30 s) light irradiation.

7.4 Conclusions

In conclusion, by grafting bis-spiropyran molecules onto the surface of the oleate-capped UCNPs *via* ligand exchange, we demonstrated that fluorescence resonance energy transfer from the upconverting UCNPs to the surface bis-spiropyran molecules can trigger the transformation of the ring-closed bis-spiropyran form to the ring-open bis-merocyanine form. Furthermore, the photochromic bis-spiropyran molecules in this system can be turned on and off using alternating NIR and visible light irradiation. Since the transformation in this model system was achieved by using NIR/visible excitation, along with the reasonable switching cycles, this new system would be very useful for biological applications related to photoswitching of photochromic compounds, which require UV irradiation to achieve the photochromic transformation.

References

[1] (a) Organic Photochromic and Thermochromic Compounds, ed. J. C. Crano and R. J. Guglielmetti, Plenum Press, New York, 1999; (b) M.-Q. Zhu, G.-F. Zhang, C. Li, M. P. Aldred, E. Chang, R. A. Drezek, A. D. Q. Li, J. Am. Chem. Soc. 133 (2011) 365; (c) M.-M. Russew, S. Hecht, Adv. Mater. 22 (2010) 3348.

[2] Z. Tian, W. Wu, A. D. Q. Li, ChemPhysChem 10 (2009) 2577.

[3] K. Kinashi, S. Nakamura, Y. Ono, K. Ishida, Y. Ueda, J. Photochem. Photobiol. A 213 (2010) 136.

[4] (a) H. Tian, Y. Feng, J. Mater. Chem. 18 (2008) 1617; (b) C. Zhang, H.-P. Zhou, L.-Y. Liao, W. Feng, W. Sun, Z.-X. Li, C.-H. Xu, C.-J. Fang, L.-D. Sun, Y.-W. Zhang, C.-H. Yan, Adv. Mater. 22 (2010) 633; (c) N. Shao, H. Wang, X.-D. Gao, R.-H. Yang, W.-H. Chan, Anal. Chem. 82 (2010) 4628; (d) I. S. Park, Y.-S. Jung, K.-J. Lee and J.-M. Kim, Chem. Commun. 46 (2010) 2859.

[5] (a) S. Zhang, Q. Zhang, B. Ye,X.Li, X. Zhang, Y. Deng, J. Phys. Chem. B 113 (2009) 6012; (b) M.-Q. Zhu, L. Zhu, J. J. Han, W. Wu, J. K. Hurst, A. D. Q. Li, J. Am. Chem. Soc. 128 (2006) 4303.

[6] J. Andersson, S.Li, Lincoln, J. Andréasson, J. Am. Chem. Soc. 130 (2008) 11836.

[7] L. Zhu, M.-Q. Zhu, J. K. Hurst, A. D. Q. Li, J. Am. Chem. Soc. 127 (2005) 8968.

[8] P. Li, Q. Peng, Y. Li, Adv. Mater. 21 (2009) 1945.

[9] (a) C.-J. Carling, J.-C. Boyer, N. R. Branda, J. Am. Chem. Soc. 131 (2009) 10838; (b) C.-J. Carling, N. Farahnaz, J.-C. Boyer, N. R. Branda, Angew. Chem., Int. Ed. 49 (2010) 3782; (c) J.-C.Boyer, C.-J. Carling, B. D. Gates, N. R. Branda, J. Am. Chem. Soc., 132 (2010) 15766; (d) F. Wang, X. Liu, Chem. Soc. Rev. 38 (2009) 976; (e) F. Vetrone, R. Naccache, V. Mahalingam, C. G. Morgan, J. A. Capobianco, Adv. Funct. Mater. 19 (2009) 2924; (f) R. Naccache, F. Vetrone, V. Mahalingam, L. A. Cuccia, J. A. Capobianco, Chem. Mater. 21 (2009) 717; (g) M. Haase, H. Schäfer, Angew. Chem., Int. Ed. 50 (2011) 5808; (h) R. Deng, X. Xie, M. Vendrell, Y.-T. Chang, X. Liu, J. Am. Chem. Soc. 133 (2011) 20168; (i) F. Wang, R.Deng, J. Wang, Q.Wang, Y. Han, H. Zhu, X. Chen, X. Liu, Nat. Mater. 10 (2011) 968.

[10] (a) F.Auzel, Chem. Rev. 104 (2004) 139; (b) N. Bogdan, F. Vetrone, G. A. Ozin, J. A. Capobianco, Nano Lett. 11 (2011) 835; (c) N. Bogdan, F. Vetrone, René Roy, J. A. Capobianco, J. Mater. Chem. 20 (2010) 7543.

[11] V. Mahalingam, F. Vetrone, R. Naccache, A. Speghini, J. A. Capobianco, Adv. Mater. 21 (2009) 4025.

[12] A. R. Clapp, I. L. Medintz, J. M. Mauro, B. R. Fisher, M. G. Bawendi, H. Mattoussi, J. Am. Chem. Soc. 126 (2004) 301.

[13] Y. Wu, X. Qu, L. Huang, D. Qiu, C. Zhang, Z. Liu, Z. Yang, L. Feng, J. Colloid Interface Sci. 343 (2010) 155.

[14] J. B. Jr. Flannery, J. Am. Chem. Soc. 90 (1968) 5660.

Acknowledgments

I would like to thank my tutor Dr. Enrico Cavalli who gave me the opportunity to carry out the PhD program in his laboratory. During these years, he constantly followed me and provided the advice necessary to proceed through the doctoral program and taught the basic knowledge of the optical spectroscopy of the inorganic solids.

I would than thank Professor John Capobianco who hosted me at Concordia University and gave me the opportunity to explore new scientific challenges.

Another special thanks goes to Professor Philippe Boutinaud that hosted me in his laboratory for an internship in the ambit of an European master and he first introduced me to world of the luminescent materials and to Professor Marco Bettinelli for the intense and profitable cooperation that we had during these three years.

A fundamental contribution to my work comes from Alessandro Belletti that provided the technical support required to carry out the experimental work, Davide Calestani for the SEM images, Roberta Magnani, Gianluca Calestani and Francesco Mezzadri for the XRD measurements.

I dedicate this work to my dear friend Stefano Marini, to my sweet English teacher Sara Martin, to my dear mother Alessandra, to my brothers Nicola and Massimiliano and their mates Chiara and Melania, to my little niece Martina and to the memory of my father that will always stand by me.